

## ABSTRACT

Title of Dissertation: BEYOND LI ION: RECHARGEABLE METAL  
BATTERIES BASED ON MULTIVALENT  
CHEMISTRY

Tao Gao, Doctor of Philosophy, 2017

Dissertation directed by: Professor Chunsheng Wang  
Department of Chemical and Biomolecular  
Engineering

The development of advanced battery technology with lower cost and higher energy density is important since various mobile applications are becoming indispensable in our daily life. While Li chemistry has approached its theoretical limit after several decades' increment improvement, the potential of multivalent chemistry (Mg, Al, etc.) remains unexplored. Compared to Li ion chemistry, multivalent chemistry provides many intriguing benefits in terms of lowering cost and increasing energy density. First of all, minerals containing multivalent element such as Mg,

Al, and etc. are much more abundant and cheaper than Li. Second, multivalent metals (Mg, Al etc.) can be directly used as anode materials, ensuring much higher anode capacity than graphite currently used in Li-ion battery. Third, the divalent or trivalent nature of the electroactive cation ( $Mg^{2+}$  and  $Al^{3+}$ ) also promise high capacity for intercalation cathodes because the capacity of these materials are limited by their available ion occupancy sites in the crystal structure instead of its capability to accept electrons.

In this dissertation, I detailed our efforts in examining some redox chemistries and materials for the use of rechargeable batteries based on multivalent metal anodes. They include intercalation cathode ( $TiS_2$ ) and conversion cathode (sulfur, iodine). We studied their electrochemical redox behavior in the corresponding chemistry, the thermodynamics, kinetics as well as the reaction reversibility. The reaction mechanism is also investigated with various macroscopic and spectroscopic techniques.

BEYOND LI ION:  
RECHARGEABLE METAL BATTERIES BASED ON MULTIVALENT CHEMISTRY

By

Tao Gao

Dissertation submitted to the Faculty of the Graduate School of the  
University of Maryland, College Park, in partial fulfillment  
of the requirements for the degree of  
Doctoral of Philosophy

2017

Advisory Committee:

Professor Chunsheng Wang, Chair  
Professor Sang Bok Lee, Dean's Representative  
Professor Michael R. Zachariah  
Professor Nam Sun Wang  
Professor Taylor J. Woehl

© Copyright by

Tao Gao

2017



# **Dedication**

Dedicated to Hong Lin

Love you

## Acknowledgements

I would like to acknowledge the support from my advisor, Prof. Chunsheng Wang. During the course of my Ph.D. study from 2013 to 2017, I learn about the most important qualities one excellent scientist should possess: diligence, creativity and critical thinking. Without his support, I wouldn't be able to finish my Ph.D. research and stand here today to defend my dissertation. I really appreciate his support on my growth in my academic career.

I want to thank Dr. Xiulin Fan, Dr. Yujie Zhu, and Dr. Liumin Suo, who taught me how to design and conduct experiment hand-by-hand when I just joined the group. I wish Dr. Zhu to become a successful professor in Beihang University, and also wish Dr. Xiulin Fan and Dr. Liumin Suo everything goes well in finding academic jobs. I believe they will become excellent scientists in this field in the future. I want to give my special gratitude to Fudong Han, who had lead my way into the field of energy storage material research and given me tremendous help during my first project, especially in writing the first scientific article. I am also grateful to my collaborators, Prof. Gary Rubloff, Prof. Sang Bok Lee, Dr. Malachi Noked, Dr. Karen Gaskell. I would like to thank all my lab mates. They are Dr. Chao Luo, Dr. Fei Wang, Dr. Chongyin Yang, Dr. Long Chen, Dr. Ji Chen, Dr. Huajun Tian, Dr. Zhaohui Ma, Ye Tao, Xiwen Wang, Wei Sun, Xiaogang Li, Singyuk Hou, Xiangyang Zhu, Jie Yue, Xiao Ji, Minglei Mao, except for the ones mentioned above. Together they have built an atmosphere in which doing research is not just joyful and but also fun.

At last, I want to send my special thanks to family, my wife, Hong Lin, my parents, Yudang

Gao and Dexiu Yu, my sister, Mei Gao and my brother Bo Gao. Without their love, understanding and support, I cannot obtain my Ph. D. in the United States.

# Table of Contents

<b>Dedication</b> .....	ii
<b>Acknowledgements</b> .....	iii
<b>Table of Contents</b> .....	v
<b>List of Tables</b> .....	viii
<b>List of Figures</b> .....	ix
<b>Chapter 1 Introduction</b> .....	1
Beyond Li ion battery: An Overview .....	1
From Fossil Fuel to Clean Energy .....	1
Batteries: Pb-Acid, Ni-MH and Li ion .....	3
Beyond Li-ion: Li/S and Li/O <sub>2</sub> .....	4
Beyond Li-ion: Multivalent Chemistry .....	6
Rechargeable Mg Battery .....	8
Electrolyte .....	8
Cathode .....	10
Rechargeable Al Battery.....	15
Motivation and Objective .....	17
Layout of this Dissertation .....	17
<b>Chapter 2 Hybrid Mg/Li Battery</b> .....	20
Introduction .....	20
Experiment .....	22

Results and Discussion .....	23
Conclusion .....	27
<b>Chapter 3 High Power Magnesium/Iodine Chemistry .....</b>	<b>28</b>
Introduction .....	28
Experiment .....	30
Calculations .....	31
Results and Discussion .....	33
ACC/I <sub>2</sub> cathode .....	33
Electrolyte .....	35
Electrochemical Performance.....	39
Two-phase reaction mechanism .....	41
Conclusion .....	49
<b>Chapter 4 Magnesium/Sulfur Battery: Thermodynamics and Kinetics .....</b>	<b>51</b>
Introduction .....	51
Experiment .....	53
Thermodynamics .....	56
Kinetics.....	68
Electrochemical Performance.....	74
Discussion.....	77
Conclusion.....	78
<b>Chapter 5 Enhancing the Reversibility of Magnesium/Sulfur Battery Chemistry</b>	
<b>through Li<sup>+</sup> Mediation .....</b>	<b>81</b>
Introduction .....	81
Experiment .....	83

Results and Discussion .....	84
Conclusion .....	92
<b>Chapter 6 Rechargeable Aluminum/Sulfur Battery based on ionic liquid electrolyte ...</b>	<b>94</b>
Introduction .....	94
Experiment .....	95
Calculation.....	97
Results and Discussion .....	98
Electrolyte .....	98
Electrochemical Performance.....	103
Reaction Mechanism .....	107
Kinetics .....	114
Conclusion .....	118
<b>Chapter 7 Summary and Future Work .....</b>	<b>121</b>
Hybrid Mg/Li Battery .....	121
Mg/I <sub>2</sub> battery.....	121
Al/S battery.....	122
Mg/S battery .....	123
<b>Bibliography .....</b>	<b>125</b>
Peer Reviewed Publications.....	135
Conference Presentations.....	139

## List of Tables

Table 3-1. Solubility of different iodine species in Mg/I <sub>2</sub> chemistry (solvent:tetraglyme) ....	30
Table 4-1. The possible polysulfide species in electrolytes.....	60
Table 4-2. The experimental bond length of sulfur and MgS (unit: Å).....	68
Table 5-1 Theoretical Capacity and Energy Density Comparison of different Battery Systems .....	82
Table 6-1. Atomic ratio (%) of each element on the surface of discharged ACC/S quantified from XPS .....	109

## List of Figures

Figure 1-1. a) Global oil production and consumption; b) The production of solar energy on a sunny day and the energy consumption of a general home; c) A usual day in Beijing; d) The desired drive range and real drive range for several EVs .....	2
Figure 1-2. Schematic of a Lithium ion Battery (LIB) .....	3
Figure 1-3. a) Top view of Li deposition <sup>[9]</sup> ; b) Cross section view of Li deposition .....	5
Figure 1-4. The capacity and reduction potential of various metal anodes.....	7
Figure 1-5. The molecular structure of the complex salt precipitated from the Mg(AlCl <sub>2</sub> BuEt) <sub>2</sub> -THF Electrolyte. ....	9
Figure 1-6. a) A schematic illustration of the charge distribution over strong d-p orbital hybridization. Electrons are accommodated in the delocalized state which extends over the transition metal and the ligand atom; b) A schematic illustration of the charge distribution over weak d-p orbital hybridization. c) The crystal structure of 1-TiSe <sub>2</sub> ; d) Energy diagram of atomic orbitals; d) XRD and SEM of TiSe <sub>2</sub> powder.....	12
Figure 1-7. Electrochemical performance of spinel TiS <sub>2</sub> at 60 C .....	13
Figure 2-1. Schematic of a) the potential and capacity of magnesium ion battery's cathode (Chevrel Phase), anode (magnesium metal) and some lithium ion battery cathodes that could possibly be used in the mixed-ion battery; b) the operating mechanism of the mixed-ion battery .....	20
Figure 2-2. a) Discharge/charge curves of TiS <sub>2</sub> cathode in the TiS <sub>2</sub>  Mg <sup>2+</sup>  Mg cell(1 <sup>st</sup> cycle) , TiS <sub>2</sub>  Li <sup>+</sup>  Li cell(1 <sup>st</sup> cycle), TiS <sub>2</sub>  Li <sup>+</sup> , Mg <sup>2+</sup>  Mg cell(2 <sup>nd</sup> cycle) at 0.1C (C=240mAh/g); b) Discharge/charge curves of TiS <sub>2</sub> cathode in the TiS <sub>2</sub>  Li <sup>+</sup> , Mg <sup>2+</sup>  Mg cell at C/3 at different cycles; c) X-ray diffraction patterns of pristine TiS <sub>2</sub> electrode and TiS <sub>2</sub> electrode after	

discharge in a $\text{TiS}_2 \text{Li}^+, \text{Mg}^{2+} \text{Mg}$ cell; d) Cyclic voltammetry of the mixed $\text{Mg}^{2+}/\text{Li}^+$ electrolyte in a three-electrodes system, WE: Pt foil; RE and CE : Mg foil, scan rate: 100mV/s; e) Scanning electron microscopy(SEM) image and f) X-ray diffraction patterns of pristine Pt foil and the deposition on Pt foil after three hours constant voltage at -0.5V vs $\text{Mg}/\text{Mg}^{2+}$ in the mixed $\text{Mg}^{2+}/\text{Li}^+$ .....	24
Figure 2-3. a) Cycling stability at C/3 and b) rate capability of a $\text{TiS}_2 \text{Li}^+, \text{Mg}^{2+} \text{Mg}$ battery .	25
Figure 2-4. Energy Density Comparison of different Battery Chemistries .....	27
Figure 3-1. (a) The capacity and voltage of typical RMB cathodes; (b) Schematic of rechargeable $\text{Mg}/\text{I}_2$ batteries. ....	29
Figure 3-2. The images of (a) iodine solution in TEGDME with no ACC; (b) iodine solution in TEGDME after adding ACC for 2 minutes; (c) iodine solution in TEGDME after adding ACC for 12 hours.....	33
Figure 3-3. (a) Procedure for preparing the $\text{ACC}/\text{I}_2$ electrode; (b) SEM and (c) EDS mapping of I in the $\text{ACC}/\text{I}_2$ electrode; (d) XRD of $\text{ACC}/\text{I}_2$ electrode. ....	34
Figure 3-4. a) Cyclic Voltammetry of electrolyte (2M $\text{Mg}$ -HMDS in TEGDME). Scan rate: 100 mV/s, voltage:-1V-3.5V. Working electrode: Pt, Reference electrode: Mg foil, Counter electrode: Mg foil. b) capacity-time curve.....	36
Figure 3-5. a) Galvanostatic discharge/charge of $\text{Cu} \text{Mg}$ coin cell. Current: 0.1 mA/cm <sup>2</sup> . Discharge time: 1h. Charge cut-off voltage: 1V; b) A typical discharge/charge curve; c) Coulombic Efficiency for Mg depositing/stripping on Cu foil.....	38
Figure 3-6. The discharge/charge curve of $\text{Mg}/\text{I}_2$ battery with $\text{ACC}/\text{I}_2$ cathode at C/4 with 0.5 M $\text{Mg}$ -HMDS electrolyte.....	39

Figure 3-7. (a) Typical charge/discharge curve of the Mg/I<sub>2</sub> battery with ACC/I<sub>2</sub> cathode; (b) Cyclic Voltammogram of the Mg/I<sub>2</sub> battery with ACC/I<sub>2</sub> cathode. Scan rate: 0.1 mV/s; (c) Cycling stability of the Mg/I<sub>2</sub> battery at 0.5 C (105.5 mA/g) with ACC/I<sub>2</sub> cathode; (d) Rate capability of Mg/I<sub>2</sub> battery with ACC/I<sub>2</sub> cathode. Error bar was plotted. The contribution of carbon has been excluded here for assessing the real capacity of iodine redox couple. The rate capability of other cathode materials are plotted for comparison ..... 41

Figure 3-8. Images of saturated I<sub>2</sub>, MgI<sub>2</sub> and Mg(I<sub>3</sub>)<sub>2</sub> solutions. Saturated I<sub>2</sub> and MgI<sub>2</sub> solutions are made by adding sufficient I<sub>2</sub> and MgI<sub>2</sub> into TEGDME until precipitates show. I<sub>3</sub><sup>-</sup>, the most common polyiodide species, was made by adding a mixture of I<sub>2</sub>/MgI<sub>2</sub> (I<sub>2</sub>:MgI<sub>2</sub>=2:1) into the solvent. .... 42

Figure 3-9. (a) Visual observation of the discharge process of Mg/I<sub>2</sub> battery at different discharge stages; the controlled FT-IR spectra of (b) I<sub>2</sub>, MgI<sub>2</sub> and Mg(I<sub>3</sub>)<sub>2</sub> in TEGDME; (c) Magnified view of the regions outlined in (b); (d) the ex-situ FT-IR spectra of Mg/I<sub>2</sub> cell during the discharge process and (e) Magnified view of the regions outlined in (d). .... 44

Figure 3-10. (a) High resolution I 3d spectra of the ACC/I<sub>2</sub> cathode; (b) High resolution Mg 1s spectra and (c) high resolution I 3d spectrum of the Mg anode. .... 46

Figure 3-11. The discharge/charge curve of Mg/I<sub>2</sub> battery based on MPC/I<sub>2</sub> cathode at C/4. 48

Figure 3-12. The self-discharge test on fresh Mg/I<sub>2</sub> cell based on MPC/I<sub>2</sub> cathode. The OCV of the cells was monitored to evaluate the shuttle effect of the cell. .... 49

Figure 4-1. Figure 1. Coulombic Titration Experiment. a) Thermodynamic equilibrium curve discharged to 0.5V. Current: 50 mA/gs, Rest 4 hours; b) thermodynamic equilibrium curve discharged to 1.4V. Current 50 mA/gs, Rest 1 hour. c-e) Transient voltage during Coulombic

Titration experiment. Sulfur loading: 1 mg/cm <sup>2</sup> , sulfur/carbon ratio= 0.125. Red: equilibrium curve; black: transient voltage; blue: current.....	58
Figure 4-2. First discharge of sulfur cathode in simple electrolyte at gradually decreasing current.....	59
Figure 4-3. ESI-MS spectra of electrolyte before and after discharge.....	60
Figure 4-4. High Resolution XPS S 2p Spectra. a) Sulfur Cathode at Different States; b) MgS; c) Schematic for the reaction mechanism .....	63
Figure 4-5. Structure of MgS <sub>x</sub> by DFT calculation.....	66
Figure 4-6 Pair Distribution Functions (PDF) of MgS <sub>x,x=8-2</sub> and MgS.....	67
Figure 4-7. First and second closest atom pair in sulfur molecule and MgS crystal .....	68
Figure 4-8. Chain length shortening scheme of MgS <sub>x,x=8-2</sub> .....	68
Figure 4-9. Kinetics Study by Experiment and AIMD Simulation. a) overpotential during coulombic titration tests; b) Cyclic Voltammetry curves at different scan rates; c) kinetic fitting of the peak current by using equation $i=avb$ ; d) Diffusivity of Mg <sup>2+</sup> in MgS <sub>x</sub> , x=8-1 obtained through AIMD simulation.....	70
Figure 4-10.The Influence of Electronic Conductivity. a) Coulombic titration curves of sulfur/carbon composite cathode with different sulfur loading. The sulfur weight ratio is given in the figure. b) the contributed capacities of each Stage.....	73
Figure 4-11. Electrochemical Performance of Sulfur cathodes. a-b) Galvanostatic discharge/charge curves at different cycles; c-d) voltage profiles for a typical cycle; e-f) Cycling performance and Coulombic efficiency, current: 100 mA/gs. ....	76
Figure 4-12. Schematic for Overall Sulfur Reduction Pathway. ....	78
Figure 5-1. Corrosion Test of Mg foil in TEGDME solution.....	86

Figure 5-2. XPS of Mg foil aged in TEGDME/sulfur, clearly demonstrating MgS layer on the Mg surface. ....	86
Figure 5-3. Comparison of surface XPS measurements of Mg anode cycled in Mg-HDMS in the absence (a) and presence (b) of LiTFSI .....	87
Figure 5-4. a) Charge/discharge curves of sulfur cathode in 0.1 M Mg-HMDS+1.0 M LiTFSI electrolyte in a three electrode cell at a current of 71 mAh/g at room temperature. Arrow illustrates the capacity increasing trend of the ACC/S composite cathode as a result of slow electrolyte penetration.b) Cycling stability of the Mg/S battery in electrolyte with and without LiTFSI.....	89
Figure 5-5. a) First cycle potential of sulfur cathode, Mg anode vs. Mg RE and full cell potential in 0.2 M Mg-HMDS + 0.5 M LiTFSI electrolyte and b) Overpotential for Mg deposition during cycling.....	90
Figure 5-6. Working mechanism of the Mg/S battery with LiTFSI additive.....	92
Figure 6-1. Al deposition/stripping in EMIC:AlCl <sub>3</sub> =1:1.3 electrolyte(black) and the electrochemical stability of the electrolyte (pink). Inset: Charge-time curve of Al deposition/stripping. Scan rate:100 mV/s, WE: Glassy carbon; CE and RE: Al wire. ....	99
Figure 6-2. Cyclic Voltammetry of Inconel alloy in a three-electrode set-up. WE: Inconel foil; CE: Al wire; RE: Al wire; Electrolyte: EMIC:AlCl <sub>3</sub> =1:1.3. Scan rate: 10 mV/s. ....	101
Figure 6-3. XPS survey spectra of a) cycled ACC/S cathode and b) cycled Al anode.....	102
Figure 6-4. Images of Inconel alloy before and after cycle. ....	103
Figure 6-5. N <sub>2</sub> adsorption/desorption isotherms measured at 77 K .....	104
Figure 6-6. The typical charge/discharge curve of the ACC/S cathode in Li/S battery.....	104
Figure 6-7. A typical charge /discharge curve of the Al/S battery with ACC/S cathode, ionic liquid electrolyte and Al foil anode. Current: 50 mA/gs. Room Temperature.....	106

Figure 6-8. Solubility of different sulfur species (in units of sulfur atomic concentration) in Li and Al electrolytes. Li electrolyte is 1M LiTFSI in TEGDME. The solubility of lithium polysulfide is from reference 20 and 21.....	106
Figure 6-9. Cycling stability of the Al/S cell.....	107
Figure 6-10. XRD of sulfur cathode before and after discharge. The bump at 15° comes from the sealing tape.....	107
Figure 6-11. High Resolution S 2p and Al 2p spectra of Al <sub>2</sub> S <sub>3</sub> .....	108
Figure 6-12. The high resolution C 1s and S 2p spectra of pristine ACC/S, discharged ACC/S with no sputtering, with 1 hour sputtering and with 4 hours sputtering.....	114
Figure 6-13. SEM images of pristine Al metal anode a) and Al metal anode after cycling b) .....	114
Figure 6-14. The voltage hysteresis of a Al/S cell at 50 mA/g, and room temperature .....	115
Figure 6-15. a) EIS of a symmetrical Al/EMIC-AlCl <sub>3</sub> /Al cell after several cycles. R <sub>ohm</sub> =3.5 ohm, R <sub>ct</sub> = 20 ohm. b) EIS of an Al/S cell after several cycles. R <sub>ohm</sub> =2.78 ohm, R <sub>ct</sub> =750 ohm. From the impedance result we can infer in an Al/S cell, the ohmic resistance is ~3 ohm, charge transfer resistance of anode reaction (Al deposition/stripping) is ~10 ohm, while charge transfer resistance of cathode reaction is almost two orders higher (750 ohm-10 ohm=740 ohm).....	116
Figure 6-16. Voltage-time curve of a typical Al/S cell. It takes > 24 hours for the system to completely remove all polarization and reach equilibrium. This indicates that diffusion of Al <sup>3+</sup> in solid phase and S/AlS <sub>x</sub> phase boundary movement are very slow during the operation of the Al/S cell. The sluggish diffusion of Al <sup>3+</sup> in solid phase can be expected from its large charge/radius ratio.....	117

Figure 6-17. a) charge/discharge curve at 50 °C(50 mA/g) and b) dQ/dV curve of Al/S cell at different temperatures; ..... 118

# Chapter 1 Introduction

## *Beyond Li ion battery: An Overview*

### **From Fossil Fuel to Clean Energy**

Today, energy and environment are two major concerns of our society. To deal with the ever-increasing global population and maintain the modern lifestyle, energy production rate must be doubled by 2050.<sup>[1]</sup> The gap between oil production and oil consumption (Figure 1-1a), as well as the global mission of reducing CO<sub>2</sub> emission, has made renewable energy production an imperative. Nevertheless, the generation of renewable energies (solar, wind, tidal and etc.) are by nature intermittent in time and dispersed in location (Figure 1-1b). Grid energy storage is required for load leveling: storing the excessive energy produced during the peak hours while releasing it during the valley hours.

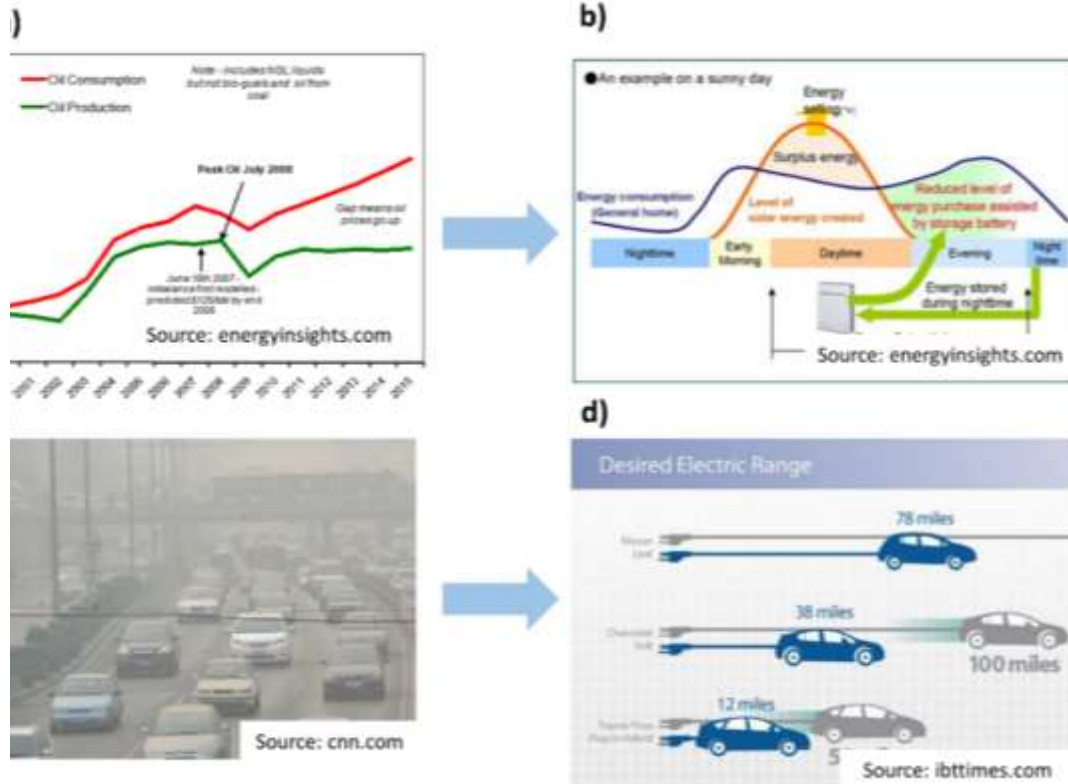


Figure 1-1. a) Global oil production and consumption; b) The production of solar energy on a sunny day and the energy consumption of a general home; c) A usual day in Beijing; d) The desired drive range and real drive range for several EVs

On the other hand, the booming of gasoline vehicles has caused serious air pollution problem, especially in big cities (Figure 1-1c). Vehicle electrification is widely accepted as the most promising solution to mitigate or even get rid of the polluting emission (Figure 1-1d). However, the unsatisfactory drive range and high cost of electric vehicles (EVs) have greatly restricted their generalization. Low cost and high energy density battery is now the deciding factor for both renewable energy and EVs.

## Batteries: Pb-Acid, Ni-MH and Li ion

Three rechargeable battery technologies are widely used in our daily life: Lead-acid battery is applied for starting, lighting and ignition in vehicles, Ni-MH battery is powering electric tools and lithium ion battery (LIB) is powering portable electronics. However, none of them is able to satisfy all criteria required for grid energy storage and vehicle electrification: 1) high energy density; 2) low cost; 3) environmentally benign. Lead-acid battery uses toxic heavy metal element. Ni-MH does not provide enough energy density. LIB's energy density (400Wh/kg) is far below the target for EVs (800-1000 Wh/kg). Massive demand of LIB could result in a roaring price of lithium due to its scarcity.<sup>[2]</sup> Thus, novel chemistry with low cost and high energy density, that is green and sustainable, is in urgent demand.

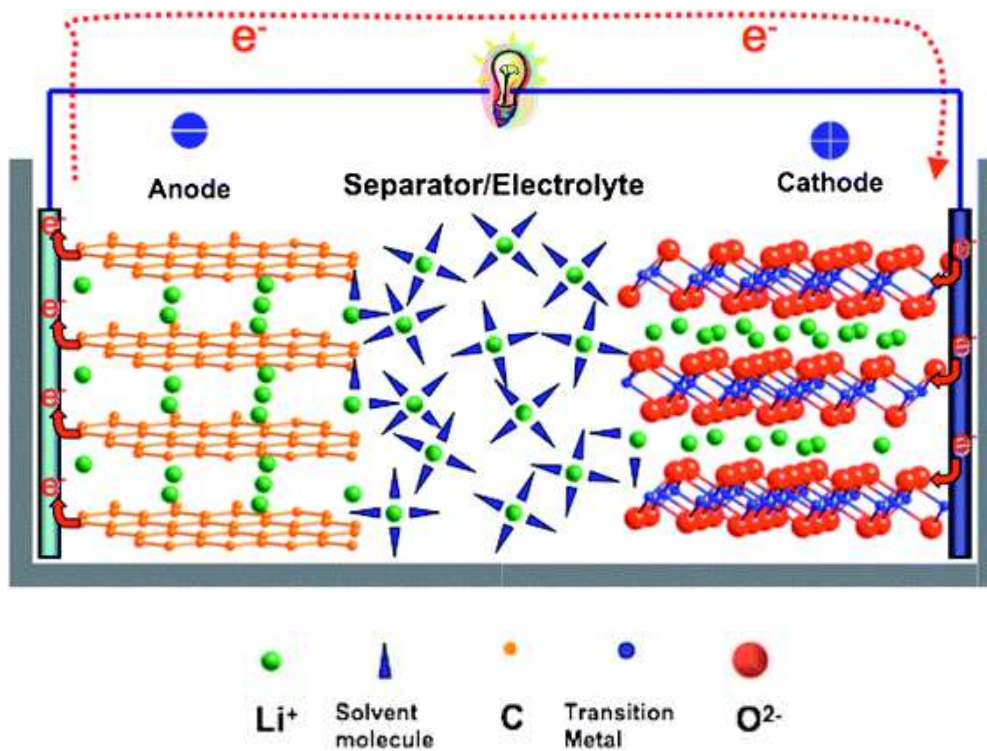


Figure 1-2. Schematic of a Lithium ion Battery (LIB)

As the most widely used rechargeable battery nowadays, LIB stores energy by elevating the chemical potential of charged species ( $\text{Li}^+$  and  $e^-$ ) through chemical bonding (electrical energy  $\rightarrow$  chemical energy); and release energy vice versa (chemical energy  $\rightarrow$  electrical energy) (Figure 1-2). Both cathode ( $\text{LiCoO}_2$ ) and anode (graphite) are layered structures where  $\text{Li}^+$  can reside between the layers after intercalation, and electrons are accepted by the electronic structure of the redox center, i.e. the 3d orbital of Co for  $\text{LiCoO}_2$  and the  $\pi$  bond of the graphene layer. During discharge,  $\text{Li}^+$  leaves graphite, shuttles through the ion-conducting electrolyte, and inserts into  $\text{LiCoO}_2$ . Simultaneously, electrons leave graphite, travel via the external circuit and are accommodated by  $\text{LiCoO}_2$ . The amount of charge ( $\text{Li}^+$  and  $e^-$ ) an electrode can hold dictates battery capacity. The potential difference of cathode and anode, intrinsically determined by the chemical potential difference of charge species in electrode materials, governs battery voltage. Together they decide the energy density of a battery chemistry.

During the past several decades, material innovation and incremental improvement have been increasing the energy density of Li-ion chemistry steadily.<sup>[3][4]</sup> However, the potential of Li-ion chemistry is close to its theoretical limit after the long-term endeavor.<sup>[5]</sup> This is because the maximum capacity of intercalation oxides, with a general formula of  $\text{LiMO}_2$  (M=transition metal), is limited to 300 mAh/g due to the presence of inactive host structure  $\text{MO}_2$ . The voltage of a full cell is limited to 5V by the Fermi energy of the 3d orbital of transition metal and the HOMO of organic electrolyte.

### **Beyond Li-ion: Li/S and Li/O<sub>2</sub>**

State-of-the-art LIB functions by  $\text{Li}^+$  intercalation into host electrodes (e.g.  $\text{LiCoO}_2$  cathode and graphite anode) through a topotactic reaction. The hosts take a large portion of the battery mass and volume but do not carry any charge. Replacing graphite with Li metal can eliminate

the inactive mass and dramatically increase the anode capacity (e.g. graphite: 372 mAh/g; Li metal: 3861 mAh/g). For this reason, Li metal anode becomes an emerging research topic and attracts plenty of efforts in recent years.<sup>[6]</sup> However, two challenges need to be solved before Li metal can be used as practical anode. The first is the potential safety hazard due to the mossy and dendritic deposition of Li.<sup>[7]</sup> When Li deposition penetrates separator, it can cause internal short-circuit and sudden release of the chemical energy as fire or explosion (Figure 1-3). Another challenge is the low coulombic efficiency of Li metal. The reactive nature of Li metal causes electrolyte decomposition and the formation of surface layer on Li surface, which acts as a side reaction on anode and in turn limits the coulombic efficiency for Li deposition/stripping.<sup>[8]</sup> This is extremely undesirable for rechargeable battery, because the side reaction can consume electrolyte during battery cycling and cause battery failure.

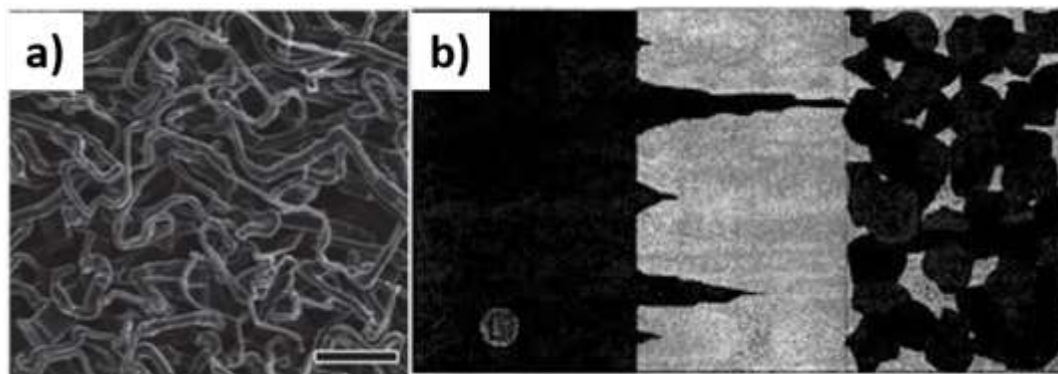


Figure 1-3. a) Top view of Li deposition<sup>[9]</sup>; b) Cross section view of Li deposition

Similar to the strategy to increase anode capacity, it is of great interest to replace intercalation cathode with conversion cathode like sulfur (voltage: 2.1V, capacity: 1650 mAh/g) and oxygen (voltage: 3.0V, capacity: 1650 mAh/g for discharged product  $\text{Li}_2\text{O}_2$ ) due to their free of inactive mass in theory. Li/S and Li/oxygen chemistries therefore become hot research topics during the past few years. <sup>[10][11][12][13]</sup> Despite significant progress was made, many practical issues

still exist. For sulfur cathode, the dissolution of polysulfide not just leads to low coulombic efficiency, but also causes active material loss and capacity fade. On the other hand, the full sulfur reduction relies on high electrolyte amount, which compromises its high capacity benefit.<sup>[14]</sup> For oxygen cathode, the large overpotential during discharge/charge remains a serious problem, since it severely limits the energy efficiency of the full cell.<sup>[15]</sup> On the other hand, no feasible approach can solve the conflicts between high discharge capacity and good reaction reversibility, despite the mechanism are recently understood.<sup>[16]</sup>

### **Beyond Li-ion: Multivalent Chemistry**

Multivalent chemistry based on Mg, Zn, Al and etc. provides many unique benefits for rechargeable batteries. Since Mg, Zn and Al are less reactive than Li and other alkaline metal, it is feasible to find a chemically stable electrolyte in which they can function without any electrolyte decomposition and surface film formation at the metal/electrolyte interface, in sharp contrast to alkaline metal anodes (Li, Na and K). This is very beneficial for increasing the energy density of the battery chemistry even considering the voltage loss of the battery due to the elevated potential of the anode compared to graphite(-2.8V vs. NHE), because using metal anodes can remarkably increase the anode capacity, especially volumetrically.<sup>[17][18]</sup> Figure 1-4 gives an overview of what metal anodes can offer compared to the current technology graphite (760 mAh/ml and 372 mAh/g). Mg metal provides a capacity of 3833 mAh/ml and 2205 mAh/g, which is ~10 and ~8 times of graphite, at a cost of 0.4 V loss in battery voltage, about 10% of the current LiCoO<sub>2</sub>/graphite battery.

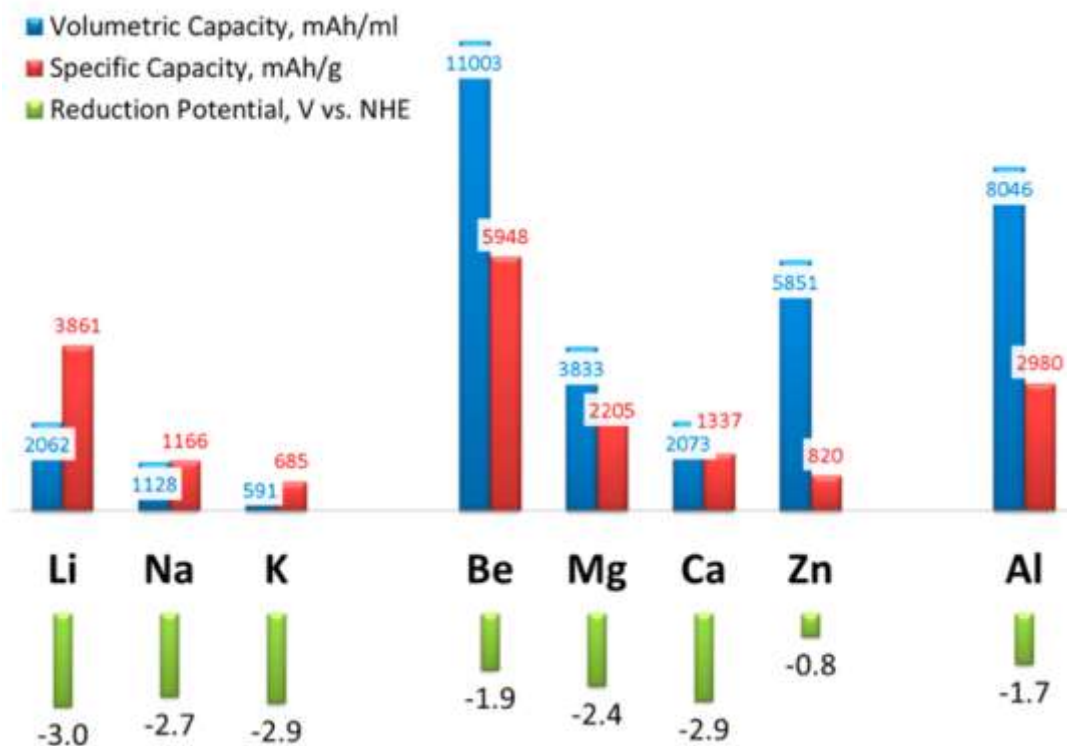


Figure 1-4. The capacity and reduction potential of various metal anodes.

On cathode side, the divalent or trivalent nature of the multivalent chemistry also provides unique advantages over Li. Current Li ion battery uses intercalation compound (e.g.  $\text{LiCoO}_2$ ,  $\text{LiMn}_2\text{O}_4$ ) as cathode. Their structure function as an ion host with many empty sites so that Li ion can enter the structure and occupy these sites during battery discharge. At the meantime, the redox center of the compound (Co 3d orbital for  $\text{LiCoO}_2$  and Mn 3d orbital for  $\text{LiMn}_2\text{O}_4$ ) takes in electron to compensate the positive charge brought in by Li ion. The capacity of the cathode depends on not only the available sites in the structure, but also the capability of the redox center to accommodate electrons. Due to the single valent nature of Li ion, these structure are usually fully filled before their redox center can accept more electrons. As a result, the potential for higher capacity of these compounds are not completely exploited.<sup>[19]</sup> Multivalent

chemistry can potentially utilize all the redox capability of these structure, because multivalent cations carrier double or triple charge of Li ion, therefore yields higher cathode capacity.

### **Rechargeable Mg Battery**

Rechargeable Mg battery receives the most attention among all multivalent chemistries because the reduction voltage of Mg (-2.4V vs. NHE) is reasonably higher than Li so that a stable organic electrolyte can be found but not too high to compromise the battery voltage too much. The studies on rechargeable Mg battery started at 1990,<sup>[20]</sup> two decades after the discovery of fast Li ion conductor and the associated fever on Li ion battery, but it received much less attention. After a decade's efforts the first prototype full cell came out in 2001.<sup>[21]</sup> As the research on Li chemistry reaches its theoretical limit, more and more endeavors are spent on Mg chemistry. The past decade have witnessed the fast growing in this field. The research in this field mainly focus on electrolyte and cathode materials development. A brief overview will be provided below.

#### **Electrolyte**

In contrast to Li<sup>+</sup>, the bivalency of Mg<sup>2+</sup> renders it difficult to migrate in the solid state.<sup>[22]</sup> As a result, any electrolyte (solvent-salt mixture) that is not chemically stable with Mg metal will passivate Mg surface and make reversible Mg deposition/stripping impossible. Popular electrolytes for Li chemistry, e.g. carbonate, nitrile based electrolytes and ClO<sup>4-</sup>, BF<sup>4-</sup> salt based electrolytes, belong to this category.<sup>[23]</sup> Fortunately, the higher reduction potential of Mg(-2.4V vs. NHE, Li: -3.0V vs NHE) makes it stable in ether solution of Grignard reagent(RMgX in THF, R is an alkyl or aryl group).<sup>[24]</sup> For this reason, it becomes the mainstream electrolyte for magnesium battery research. A comprehensive review of the development on Mg battery electrolyte can be found in literature.<sup>[25][18]</sup>

The first prototype Mg battery utilized  $\text{Mg}(\text{AlCl}_2\text{BuEt})_2$ -THF electrolyte, made by in-situ reacting Grignard reagent  $\text{RMgCl}$  ( $\text{R}=\text{Bu}$  or  $\text{Et}$ ) and  $\text{AlCl}_3$  in THF. The adding of  $\text{AlCl}_3$ , a strong Lewis acid, increases the anodic stability of the electrolyte from 1.0V vs. Mg to 2.0V vs. Mg due to the formation of complex Mg cation and Al anion (Figure 1-5). It also increases its ionic conductivity.<sup>[26]</sup> While this enables the use of sulfide cathode ( $\text{Mo}_6\text{S}_8$ , voltage: 1.1V), its anodic stability is still not sufficient for oxide cathode with high voltage. For this reason, later development of electrolyte has been partially focuses on improving the anodic stability. Replacing alkyl magnesium chloride (e.g.  $\text{BuMgCl}$ ) with aryl magnesium chloride (e.g.  $\text{PhMgCl}$ ) successfully increases the anodic stability to 3.0V,<sup>[27]</sup> and later work of replacing  $\text{AlCl}_3$  by  $\text{Al}(\text{OPh})_3$  further increases the stability to 4.5V due to the reducing amount of  $\text{Cl}^-$ .<sup>[28]</sup> Besides enhancing the anodic stability of electrolyte, there is a strong incentive to substitute the organometallic species in the complex electrolyte with inorganic constituents, because they are highly unstable in the presence of water and air and many of them are pyrophoric. An all inorganic complex electrolyte was then brought up in 2014, which was made by reacting  $\text{MgCl}_2$  with  $\text{AlCl}_3$ .<sup>[29]</sup>

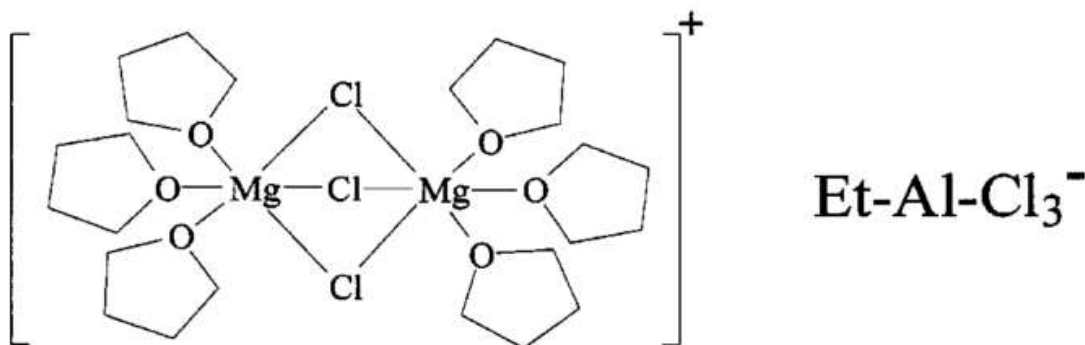


Figure 1-5. The molecular structure of the complex salt precipitated from the  $\text{Mg}(\text{AlCl}_2\text{BuEt})_2$ -THF Electrolyte.

Since the complex electrolyte is difficult to make, and the chlorine it contains is highly corrosive to battery current collector, many efforts were also devoted to developing Mg electrolyte based on simple salt.  $\text{Mg}(\text{BH}_4)_2$  was first used because it shows great chemical stability against Mg anode due to its reductive nature, and its ethereal solution demonstrates reversible Mg deposition/stripping.<sup>[30]</sup> Meanwhile, it shows comparable anodic stability on non-noble metal current collector and noble metal current collector, in sharp contrast to the above complex electrolyte. To further enhance its anodic stability, Mg salts based on boron-cluster anion<sup>[31]</sup> and monocarborane anion<sup>[32]</sup> were invented, and the latter shows an anodic stability of  $>3.5\text{V}$  on non-noble metal current collector (stainless steel, Ni etc.), permitting the use of coin cell for evaluating oxide cathodes. This achievement was regarded as a turning point in Mg electrolyte development for practical Mg batteries.

Except for the above simple salts,  $\text{Mg}(\text{TFSI})_2$  also attracts some attention since it is the only ether soluble inorganic salt commonly used in battery research (others include  $\text{Mg}(\text{BF}_4)_2$ ,  $\text{Mg}(\text{ClO}_4)_2$  are not soluble).<sup>[33]</sup> Nevertheless, Mg deposition/stripping in  $\text{Mg}(\text{TFSI})_2$ -ether electrolyte needs large overpotential to drive and bears low coulombic efficiency. Recent work shows that moisture content is critical for the performance of this simple electrolyte and water content below 15 ppm is necessary for the reversible Mg deposition/stripping.<sup>[34]</sup> Adding  $\text{MgCl}_2$  to complex with  $\text{MgTFSI}_2$  was shown to be an effective approach to reduce the overpotential and increase the reversibility.<sup>[35]</sup>

### **Cathode**

The first rechargeable Mg battery use Chevrel phase,  $\text{Mo}_6\text{S}_8$ , as the cathode. It shows a voltage of 1.2V and a capacity of 120 mAh/g, yielding an energy density of  $\sim 140\text{ Wh/kg}$ , much lower

than that of LiCoO<sub>2</sub> in Li ion battery. Cathode materials with higher voltage and/or higher capacity are needed to achieve a higher energy density.

Although Mg<sup>2+</sup> has similar ion radius as Li<sup>+</sup>, intercalation compounds with high Li storage capability were mostly not able to insert Mg<sup>2+</sup>. Due to the large inter-layer space and the weak Van der Waals force, layered oxides and sulfides like V<sub>2</sub>O<sub>5</sub>, TiS<sub>2</sub> were initially thought to be able to accept Mg<sup>2+</sup>. However, experiment shows they do not intercalate Mg<sup>2+</sup> electrochemically despite chemical magnesianation were reported possible.<sup>[36][37]</sup> Various polymorphs of MnO<sub>2</sub> were also tested since they are all open framework materials with certain ion hopping channel, but usually large overpotential was accompanied during discharge/charge.<sup>[38][39]</sup> An explanation refers the sluggish Mg diffusion in solid state, which is resulted mainly from the difficulty for the host to accommodate the electrons and partially from the strong coulombic repulsion between the host and Mg ion, as the main reason for their inability to intercalate Mg<sup>2+</sup>.<sup>[22]</sup> This theory explains the Chevrel phase's electrochemical results quite well, which attributes the Mg storage capability to its ability to fast attain local electro-neutrality after Mg<sup>2+</sup> insertion by the Mo<sub>8</sub> cluster in its unique crystal structure.<sup>[22]</sup> Later this theory was proved by the storage of Mg in Fullerene since it can delocalize electrons on the entire cluster rather than to individual atoms.<sup>[40]</sup> Recently, this idea was extended to binary compounds that have overlapping electron orbital for their two constituting atoms, e.g. TiSe<sub>2</sub>, TiS<sub>3</sub>, because the transition metal and the chalcogenides form d-p orbital hybridized electron structure, so that the introduced electrons can be distributed over the metal-ligand unit rather than on the metal center(Figure 1-6).<sup>[41][42]</sup>

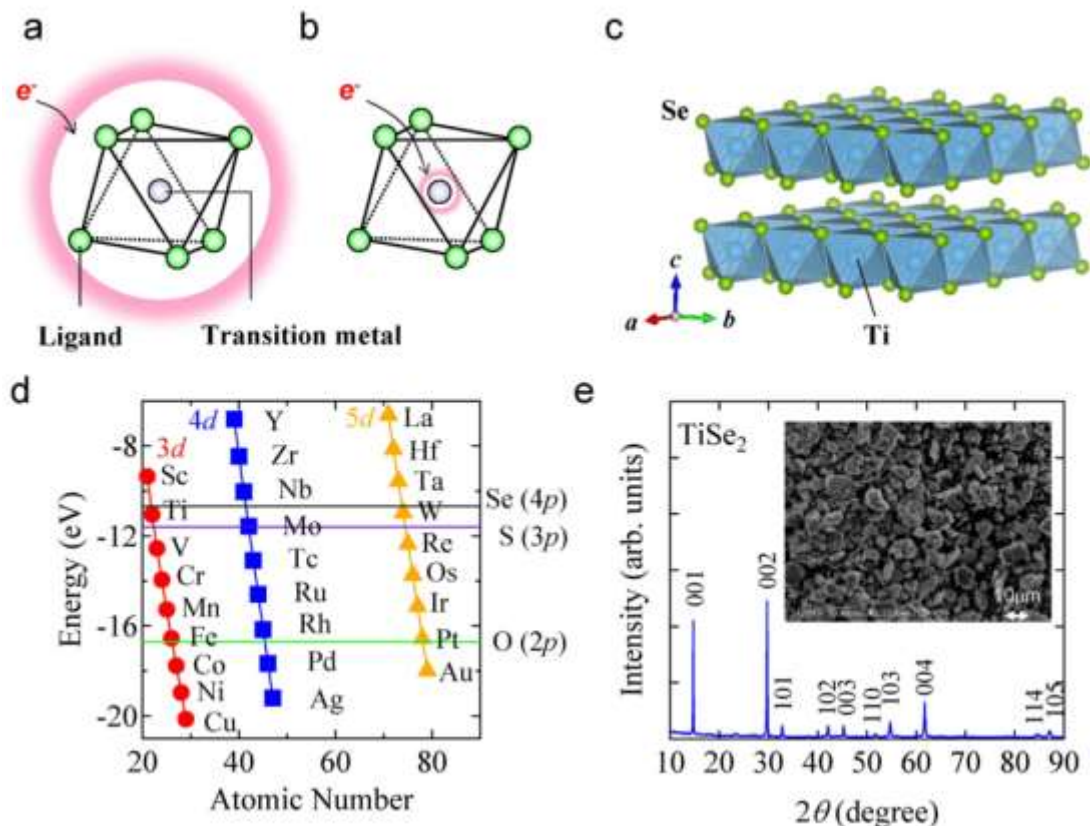


Figure 1-6. a) A schematic illustration of the charge distribution over strong d-p orbital hybridization. Electrons are accommodated in the delocalized state which extends over the transition metal and the ligand atom; b) A schematic illustration of the charge distribution over weak d-p orbital hybridization. c) The crystal structure of 1-TiSe<sub>2</sub>; d) Energy diagram of atomic orbitals; e) XRD and SEM of TiSe<sub>2</sub> powder.

To develop materials with fast Mg diffusion, ab initio quantum calculation has been conducted. It was discovered that multivalent cation diffusion is first dependent on structure,<sup>[43]</sup> which determines the diffusion pathway, and then on its chemistry, which determines the interactions between the intercalant and the host anion lattice.<sup>[19,44]</sup> In different structures, coordination preference of the multivalent cation dictates the energy level change during their migration

along the possible diffusion pathway, and structures in which the intercalants occupy the site that does not have its preferred coordination can reduce the migration energy barrier to ~525-650 meV, a value necessary for acceptable migration kinetics at room temperature. For this reason, the spinel structure was regarded as a better choice for Mg battery over layered or olivine structure, because  $Mg^{2+}$  has a lower migration barrier in spinel structure since the stable insertion site is four coordinated tetrahedral site but Mg prefers six coordination.<sup>[43]</sup> Further calculation shows that sulfide spinel is better than oxide spinel because the longer M-S imposes less ionic interaction with the  $Mg^{2+}$ . Recently, the spinel sulfide was synthesized and it shows remarkable capacity and intercalation kinetics especially at high temperature, which proves the calculation prediction (Figure 1-7).<sup>[45]</sup>

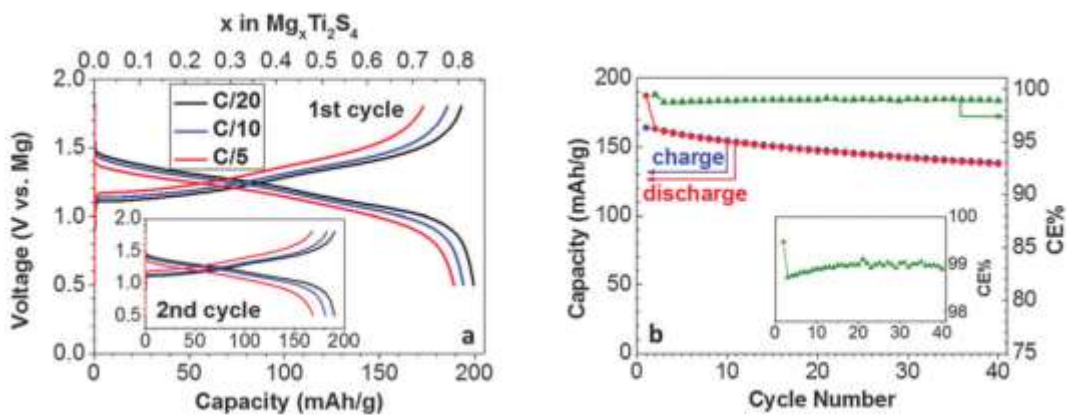


Figure 1-7. Electrochemical performance of spinel  $TiS_2$  at 60 C

Despite of the outstanding results, the spinel  $TiS_2$  shows inferior performance at room temperature and relatively low voltage. According to inductive effect, replacing S with more electronegative anion (such as O) can increase the voltage due to the more ionic nature of the M-X bond.  $\alpha-MoO_3$  was examined recently and it shows no electrochemical activity. Interestingly, after partial doping O by F, a reversible capacity of 75 mAh/g can be achieved

with large overpotential. Since slow Mg diffusion was the main reason for the large overpotential, it is necessary to improve Mg mobility at room temperature.<sup>[46]</sup> For this reason, a Mo-V-O ternary oxide with open channel was proposed by Jacobson et al,<sup>[47]</sup> because they believe Mo and V's ability to change multiple oxidation states ensures better charge redistribution therefore leading to better kinetics. The material shows a capacity of ~400 mAh/g at ~2.0V in a three-electrode set-up.

Another type of intercalation materials that have been studied for Mg battery is the Prussian Blue complex, with a typical formula of  $MN(CN)_6$ , in which M and N refer to transition metal and CN refers to the ligand which connects all transition metals and therefore forms an open framework in which ions can occupy the interstitial sites. A capacity of ~80 mAh/g was realized with  $NiFe(CN)_6$  with active carbon as reference electrode.<sup>[48][49]</sup> Nevertheless, a full cell with Mg anode has never been demonstrated.

Other than intercalation compounds, conversion cathodes were also investigated for Mg battery. Conversion reaction usually occurs during ion insertion when the electrode material does not have open ion diffusion channel, or the number of inserted ion exceeds the maximum available sites. Materials of this type include many transition metal oxides, sulfides, chloride and etc. Some Manganese oxide, e.g. ramsdellite- $MnO_2$  and  $\alpha$ - $MnO_2$ , despite of their open channel for ion transport, are shown to undergo conversion reaction due to the strong distortion that damages the structure integrity by calculation.<sup>[50]</sup> Transition metal sulfides are also studied, for example copper sulfide and copper selenide. It is interesting to note that CuS does not show any electrochemical activity at room temperature for Mg storage,<sup>[51]</sup> while  $Cu_2Se$  shows a capacity of 250 mAh/g<sup>[52]</sup>. Transition metal chloride were shown to have fast discharge kinetics, due to the dissolution of discharge product  $MgCl_2$ .<sup>[53]</sup> Organic materials, emerging in recent years, are also being studied as Mg cathode, for example, DMBQ<sup>[54]</sup>, polyanthraquinone<sup>[55]</sup>.

Due to the slow Mg mobility in solid state and poor interfacial kinetics, many materials do not show electrochemical activity upon Mg insertion. For this reason, high temperature test protocol has been proposed and used. Because ion diffusion is a thermal activated process, it is expected to see an increases in Mg ion mobility. On the other hand, high temperature also reduces the energy barrier for desolvation process upon interfacial charge transfer. With this protocol, Nazar et al. has successfully realized reversible Mg insertion/extraction with both spinel<sup>[45]</sup> and layer  $\text{TiS}_2$ <sup>[56]</sup> at 60 °C, and they also demonstrated CuS conversion cathode at 150 °C, whose activity was triggered upon repeated cycling at high temperature.<sup>[51]</sup>

To address the cathode kinetics limitation, some studies have revealed that trace water in Mg electrolyte can facilitate Mg intercalation, probably due to the shielding of Mg ion charge by water solvation. However, the compatibility of such moisture contained electrolyte with Mg metal remains a problem. On the other hand, recent study has pointed out that the large capacity of oxides( $\text{V}_2\text{O}_5$ ) in moisture contained electrolyte is mainly from proton insertion instead of Mg intercalation.<sup>[34]</sup>

Some simple redox cathode material is also being studied. Sulfur has very high capacity, but the first concept cell was not published until a non-nucleophilic electrolyte was developed.<sup>[57]</sup> Oxygen has also attracted some attention, and these studies show Mg/ $\text{O}_2$  chemistry suffers similar large overpotential issue as Li/ $\text{O}_2$  does..<sup>[58,59]</sup>

### **Rechargeable Al Battery**

Although primary Al/ $\text{O}_2$  battery has been commercialized for many years, the study of rechargeable Al battery is still at its early stage. This is partially due to its high reduction potential has sacrificed its potential for realizing a high voltage battery. Nevertheless, the high

volumetric capacity of Al makes it attractive for niche market where compact size is required, e.g. submarine. The study of rechargeable Al battery is also of scientific value since it shares many similarity to other multivalent chemistry.

Due to its higher reduction potential and less reactivity than alkali and alkali earth metal, the using of aqueous electrolyte is possible. Commercial Al/O<sub>2</sub> battery uses concentrated KOH solution as the electrolyte, and during discharge, Al is dissolved into the electrolyte. Since this reaction is not reversible, aqueous electrolyte is only limited to primary Al batteries.

Ionic liquid based electrolyte has been extensively studied for over two decades, due to the large demand of Al electrolyte in Al production industry.<sup>[60,61]</sup> Due to its high charge density, Al does not exist as simple ion in these electrolytes. Instead, Al containing salt, usually Al halides, complex with other components of the electrolyte and form a complex anion. In the ionic liquid electrolyte, AlCl<sub>3</sub> was dissolved into 1-methy-2-ethyl-imidazolium chloride ionic liquid with a molar ratio larger than one (usually:1.3). The excessive amount of AlCl<sub>3</sub> ensures the solution to be acidic, and the formed Al<sub>2</sub>Cl<sub>7</sub><sup>-</sup> complex in this environment has very good electrochemical activity for Al deposition/stripping and very high ionic conductivity.<sup>[62]</sup>

Non-aqueous electrolyte based on organic solvent also received some attentions. Reversible Al stripping/deposition was first shown possible in AlCl<sub>3</sub>-LiCl-dimethylsulfone system at high temperature,<sup>[63,64]</sup> and recently room temperature deposition/stripping was demonstrated in AlCl<sub>3</sub>-ether system.<sup>[65]</sup>

Regarding cathode materials, graphitic materials were studied because they can intercalate the anion from the ionic liquid electrolyte during charge.<sup>[66]</sup> Conversion cathode were also investigated and showed reversible capacity.<sup>[67]</sup> Studies on sulfur cathode also attracts some attention recently.<sup>[68]</sup>

### Motivation and Objective

Considering the potential of achieving energy density exceeding Li ion battery, it is important to investigate potential redox chemistries for rechargeable batteries based on multivalent metal anodes. On the other hand, there are also many fundamental scientific questions remain unanswered for multivalent chemistry. From the perspective of electrochemistry, the structure of the complex ion in the electrolyte, its desolvation and charge transfer process at the interface, the Mg deposition mechanism are still not understood. From the perspective of material science, how the material thermodynamics is compared to that in Li chemistry, what dominates the mobility of multivalent cation in solid materials are still opaque. In this dissertation, I aim to examine possible cathode materials for multivalent battery, with an emphasis on Mg chemistry. Fundamentally, I want to investigate the thermodynamics, kinetics and reversibility of these materials in multivalent chemistry. Practically, I want to construct concept battery and test their electrochemical performance so as to examine their feasibility to be used in rechargeable batteries.

### Layout of this Dissertation

**Chapter 2.** I will discuss my attempt of constructing a hybrid Mg/Li battery by coupling Li<sup>+</sup> intercalation cathode(TiS<sub>2</sub>) with Mg metal anode in a mixed Mg<sup>2+</sup>/Li<sup>+</sup> electrolyte. This hybrid cell design aims to replace the inferior Mg<sup>2+</sup> intercalation at cathode by the superior Li<sup>+</sup> intercalation so that many intercalation compounds, previously believed not usable in Mg batteries, can be utilized. Such hybrid cell can combine the high capacity/voltage of Li<sup>+</sup> intercalation cathode with the high capacity Mg anode. This work is published in Advanced Energy Material.( T. Gao *et al.* Hybrid Mg<sup>2+</sup>/Li<sup>+</sup> Battery with Long Cycle Life and High Rate Capability, *Advanced Energy Materials*, DOI: 10.1002/aenm.201401507)

**Chapter 3.** I will elaborate on the idea of using liquid-solid two phase reaction to address the poor cathode kinetics in Mg batteries. The liquid-solid two phase reaction bypasses the sluggish solid state diffusion of  $Mg^{2+}$ , which is the main reason for the poor kinetics for  $Mg^{2+}$  intercalation. Iodine is a perfect example for demonstrating this idea since iodine and its partially reduced product, polyiodide, are highly soluble while the final discharge product, iodide, is insoluble. The constructed iodine/Mg battery shows remarkable rate capability (kinetics) than all systems reported before. This work is published in Nature Communication. (H. Tian, T. Gao (co-first author), et al. High Power Rechargeable Magnesium/iodine Battery Chemistry, Nature Communications, Accepted, 2016).

**Chapter 4.** I will introduce the thermodynamic and kinetics study of sulfur cathode in different Mg electrolytes. Sulfur is a promising cathode material due to its high capacity (1675 mAh/g). Despite previous studies have proved the feasibility of Mg/S battery, the voltage profile of sulfur cathode at different Mg concentration remains controversial partially due to the complicated interaction between the polysulfide species with the complex electrolyte. In this work, I compared the equilibrium potential curves of sulfur in both simple and complex electrolyte using three-electrode cells and investigated the reaction pathway during sulfur reduction. The kinetics was also studied by both experimental work and computational approach. The work is currently under preparation.(Manuscript under preparation).

**Chapter 5.** I will present my previous efforts of modifying the composition of electrolyte to enhance the reversibility of Mg/S chemistry. The reversibility of Mg/S battery remains a problem hindering its practical application. This is partially due to the difficulty to oxidize  $MgS_x$  electrochemically. In this work, I found that  $Li^+$  can facilitate the dissolution of  $MgS_x$ , enhancing the oxidation kinetics and therefore dramatically increasing the cycling stability of Mg/S battery. The work is published in Journal of American Chemical Society.(T. Gao(co-

first), M. Noked, et al. Enhancing the Reversibility of Mg/S Battery Chemistry through Li<sup>+</sup> Mediation, *Journal of American Chemical Society*, 37(2015)12388.)

**Chapter 6.** I will present the work on rechargeable aluminum/sulfur battery based on ionic liquid electrolyte. Similar to Mg, aluminum has high capacity (especially volumetrically) and shows high reversible (100%) deposition/stripping in ionic liquid electrolyte. In this study, I investigated the possibility of Al/S battery and demonstrated the first rechargeable Al/S battery. Its reaction mechanism and kinetics were also studied with various characterization techniques. This work is published in *Angewandte Chemie International Edition*. (T. Gao, et al, Rechargeable Al/S Battery with Ionic Liquid Electrolyte, *Angew. Chem. Int. Ed.* 55(2016), 9898-9901).

**Chapter 7.** I will summarize my main contribution to the field both in terms of scientific discoveries and practical applications. I will also point out the shortcoming of the current work and lay out the future plan to develop multi-valent battery chemistries.

## Chapter 2 Hybrid Mg/Li Battery

### Introduction

Due to the sluggish solid state diffusion of  $Mg^{2+}$ , it is difficult to find a proper cathode with facile Mg intercalation kinetics. One potential approach is to circumvent the intercalation of clumsy  $Mg^{2+}$  by coupling Mg metal anode with a mature LIB cathode in a mixed  $Mg^{2+}/Li^+$  electrolyte. A hybrid battery chemistry thus constructed simultaneously combines the high-capacity/high-voltage LIB cathodes, the fast  $Li^+$  intercalation and the high-capacity/dendrite-free Mg anode (Figure 2-1). This concept of employing multiple ions in the same electrochemical device can actually be traced back to the so-called ‘Daniel Cell’ demonstrated by British chemist John. F. Daniel in 1883.

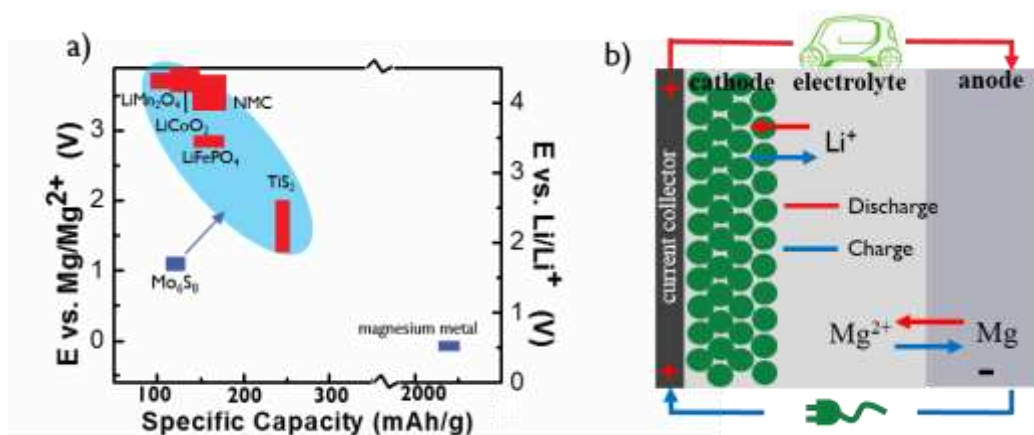
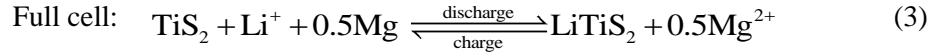
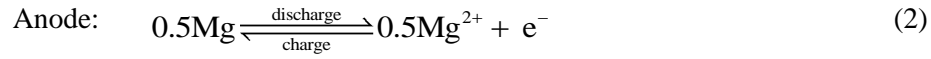


Figure 2-1. Schematic of a) the potential and capacity of magnesium ion battery's cathode (Chevrel Phase), anode (magnesium metal) and some lithium ion battery cathodes that could possibly be used in the mixed-ion battery; b) the operating mechanism of the mixed-ion battery

Several aspects must be carefully examined before designing a hybrid  $\text{Mg}^{2+}/\text{Li}^+$  battery with high performance. First of all, the presence of lithium salt in the Mg complex electrolyte directly affects its electrochemical properties.<sup>[69]</sup> In addition, the current collector must be carefully chosen, as the corrosion of current collectors by electrolyte components could have a significant influence on the stability window of the complex electrolyte. For instance, the anodic stability of APC(all phenyl complex) could be lowered to  $\leq 2.0$  V (vs.  $\text{Mg}/\text{Mg}^{2+}$ ) when non-inert metals are used as the current collector.<sup>[69]</sup> Most importantly, the chosen cathode must be compatible with the complex electrolyte, i.e. it should have redox potential within the electrochemical stability window of the complex electrolyte and also remain chemically inert to electrolyte components to avoid any parasitic reactions.

With these considerations, we propose a novel hybridized  $\text{Mg}^{2+}/\text{Li}^+$  battery with APC-LiCl as the electrolyte, stainless steel as the current collector,  $\text{TiS}_2$  as the cathode and Mg foil as the anode. Since the lithium salt anion,  $\text{Cl}^-$ , is a part of APC's composition, LiCl was expected to exhibit good compatibility with APC. For practical applications, stainless steel was chosen as the current collector, which lowers the anodic stability of the electrolyte to 2.0V, but eliminates the utilization of expensive noble metals. LIB cathodes with lithiation/delithiation potential below 2.0 V were screened, and layered  $\text{TiS}_2$  was identified as a model cathode due to its relatively high voltage (1.0-1.6 V), large capacity (240 mAh/g), high reversibility and good compatibility with the complex electrolyte.

The APC-LiCl complex was revealed to be able to dissociate  $\text{Li}^+$  and  $\text{Mg}^{2+}$ .<sup>[70]</sup> The proposed working mechanism is shown in Fig 8b. During discharge,  $\text{Li}^+$  is inserted into  $\text{TiS}_2$  (Equation 1) and Mg is dissolved from Mg foil into electrolyte (Equation 2), while during charge  $\text{Li}^+$  is extracted from lithiated  $\text{TiS}_2$  (Equation 1) and Mg is deposited onto Mg foil (Equation 2). The full cell reaction is given in Equation 3.



## Experiment

**Electrolyte Synthesis:** The synthesis of electrolytes was conducted under pure argon atmosphere in VAC, Inc. glove box (<1 ppm of water and oxygen). The solvent, anhydrous THF (Aldrich, 99.9%, inhibitor free), was dried with molecular sieve (5 Å, Aldrich) in glove box overnight before filtering. The electrolyte in control experiment (1), 0.4 M LiCl in THF, was prepared by dissolving LiCl (Aldrich, 99%) into THF. The electrolyte in control experiment (2), 0.4 M APC, was prepared by first dissolving AlCl<sub>3</sub> (Aldrich, 99.999%) into THF followed by adding the solution dropwisely into PhMgCl solution (Aldrich, 2.0 M in THF) and stirring overnight. The electrolyte in control experiment (3), 0.4M APC-LiCl, was prepared by dissolving LiCl into the synthesized APC electrolyte.

**Electrochemical Measurement:** Galvanostatic tests were carried out in 2025 coin cells with Land CT 2001A. Micron-sized TiS<sub>2</sub> powder (Aldrich, 99.9%, 200 mesh) were mixed with carbon black (Super P) and sodium alginate (MP, Biomedicals) in an 80:10:10 wt% ratio, hand-milled for 30 min, and then casted onto individual stainless steel disk (TBI, 0.001 in. thickness). The loading for each electrode is ~1.0 mg. The electrode disks were dried in a vacuum oven at 100 °C overnight. Li foil and Mg ribbon were used as anodes in LIB and MIB/mixed-ion battery. Celgard 3501 was used as the separator. CV was performed on Gamry Reference 3000 with a scan rate of 100 mV/s, and -1 and 2 V (vs Mg/Mg<sup>2+</sup>) were used as high and low cutoff voltages when testing the APC-LiCl electrolyte.

**Material Characterization:** The morphology of the deposition in APC-LiCl complex electrolyte was examined using a Hitachi SU-70 field-emission scanning electron microscope. X-ray powder diffraction patterns were obtained on Bruker Smart 1000 (Bruker AXS Inc., USA) by using Cu K $\alpha$  radiation with an air-tight holder from Bruker. Electron energy loss spectroscopy results were obtained on JEOL JEM 2100F TEM/STEM.

### **Results and Discussion**

To confirm that only Li<sup>+</sup> rather than Mg<sup>2+</sup> intercalates into TiS<sub>2</sub> in the mixed-ion electrolyte, control experiments were conducted in three different cells with TiS<sub>2</sub> as the cathode: 1) a TiS<sub>2</sub>|Li<sup>+</sup>|Li LIB using LiCl-Tetrahydrofuran (THF) electrolyte and Li anode; 2) a TiS<sub>2</sub>|Mg<sup>2+</sup>|Mg MIB using APC electrolyte and Mg anode; 3) a TiS<sub>2</sub>|Li<sup>+</sup>, Mg<sup>2+</sup>|Mg hybrid battery using APC-LiCl electrolyte and Mg anode.

Figure 2-2a shows the galvanostatic charge/discharge curves of TiS<sub>2</sub> cathodes in these three different cells. In the TiS<sub>2</sub>|Li<sup>+</sup>|Li cell, the lithiation/delithiation curves of TiS<sub>2</sub> in LiCl-THF electrolyte is almost identical to that of TiS<sub>2</sub> in LiPF<sub>6</sub>-EC-DEC electrolyte, demonstrating that Li<sup>+</sup> can reversibly intercalate/deintercalate into TiS<sub>2</sub> in LiCl-THF electrolyte in the same manner as in a typical LIB electrolyte. On the contrary, TiS<sub>2</sub> barely delivers any capacity in the TiS<sub>2</sub>|Mg<sup>2+</sup>|Mg cell, showing that Mg<sup>2+</sup> could not intercalate into TiS<sub>2</sub> structure. Nevertheless, in the TiS<sub>2</sub>|Li<sup>+</sup>, Mg<sup>2+</sup>|Mg cell, similar charge/discharge curves and a comparable capacity as that in the TiS<sub>2</sub>|Li<sup>+</sup>|Li cell was shown, indicating similar solid solution reaction in the hybrid cell. The ‘Li<sup>+</sup> only intercalation’ mechanism at cathode was further verified by comparing powder X-ray diffraction (XRD) patterns of TiS<sub>2</sub> electrode before and after discharging (Figure 2-2c). The wide broadening peaks at 2 $\theta$ = 13° and 20° arose from the air-tight sample holder. The XRD pattern of the pristine sample is in good agreement with JCPDS-15-0853, indicating

the high crystallinity of  $\text{TiS}_2$ . After discharge, the pattern can be well indexed to  $\text{LiTiS}_2$  (JCPDS-28-0595), confirming that only  $\text{Li}^+$  could be inserted into  $\text{TiS}_2$  in the mixed-ion electrolyte.

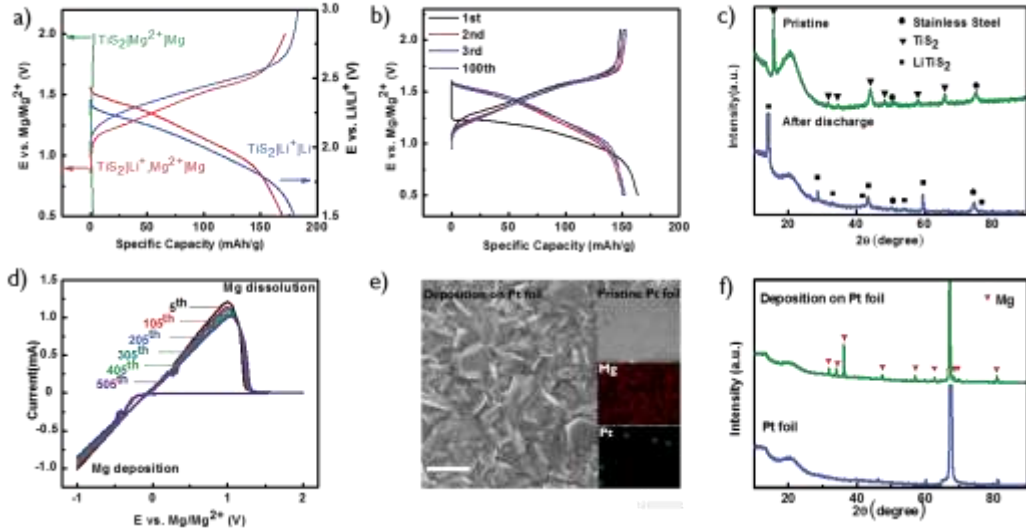


Figure 2-2. a) Discharge/charge curves of  $\text{TiS}_2$  cathode in the  $\text{TiS}_2|\text{Mg}^{2+}|\text{Mg}$  cell(1<sup>st</sup> cycle) ,  $\text{TiS}_2|\text{Li}^+|\text{Li}$  cell(1<sup>st</sup> cycle),  $\text{TiS}_2|\text{Li}^+, \text{Mg}^{2+}|\text{Mg}$  cell(2<sup>nd</sup> cycle) at 0.1C ( $C=240\text{mAh/g}$ ); b) Discharge/charge curves of  $\text{TiS}_2$  cathode in the  $\text{TiS}_2|\text{Li}^+, \text{Mg}^{2+}|\text{Mg}$  cell at C/3 at different cycles; c) X-ray diffraction patterns of pristine  $\text{TiS}_2$  electrode and  $\text{TiS}_2$  electrode after discharge in a  $\text{TiS}_2|\text{Li}^+, \text{Mg}^{2+}|\text{Mg}$  cell; d) Cyclic voltammetry of the mixed  $\text{Mg}^{2+}/\text{Li}^+$  electrolyte in a three-electrodes system, WE: Pt foil; RE and CE : Mg foil, scan rate: 100mV/s; e) Scanning electron microscopy(SEM) image and f) X-ray diffraction patterns of pristine Pt foil and the deposition on Pt foil after three hours constant voltage at -0.5V vs  $\text{Mg}/\text{Mg}^{2+}$  in the mixed  $\text{Mg}^{2+}/\text{Li}^+$

The electrochemical performance of the APC-LiCl complex electrolyte was examined by cyclic voltammetry (CV) (Figure 2-2d), and the morphology and composition of the deposition

from the electrolyte were investigated by scanning electron microscopy (SEM) (Figure 2-2e) and XRD (Figure 2-2f). CV was conducted in a three-electrode cell with Pt foil as working electrode and two Mg foils as reference and counter electrodes.  $Mg^{2+}$  started to deposit on Pt during the cathodic scan to  $-0.2$  V (vs.  $Mg/Mg^{2+}$ ) and the deposition product started to dissolve when voltage exceeded  $-0.1$  V (vs.  $Mg/Mg^{2+}$ ) during the reverse scan. The deposition/dissolution of Mg was highly reversible for hundreds of cycles. To examine the chemical composition of the deposit from the  $Mg^{2+}/Li^+$  mixed-ion electrolyte, XRD patterns of the Pt working electrode were recorded before and after electrochemical depositing in the APC-LiCl electrolyte (Figure 2-2f). After three hours of deposition, all XRD peaks of the deposition can be assigned to Mg except for the peaks of the sample holder and Pt substrate. No peaks can be indexed to Li or Mg-Li alloy. The surface morphology of the deposit from the APC-LiCl complex electrolyte was also examined under SEM, which reveals that no dendrite but micron-sized uniform scale-like deposition (Figure 2-2e) was formed.

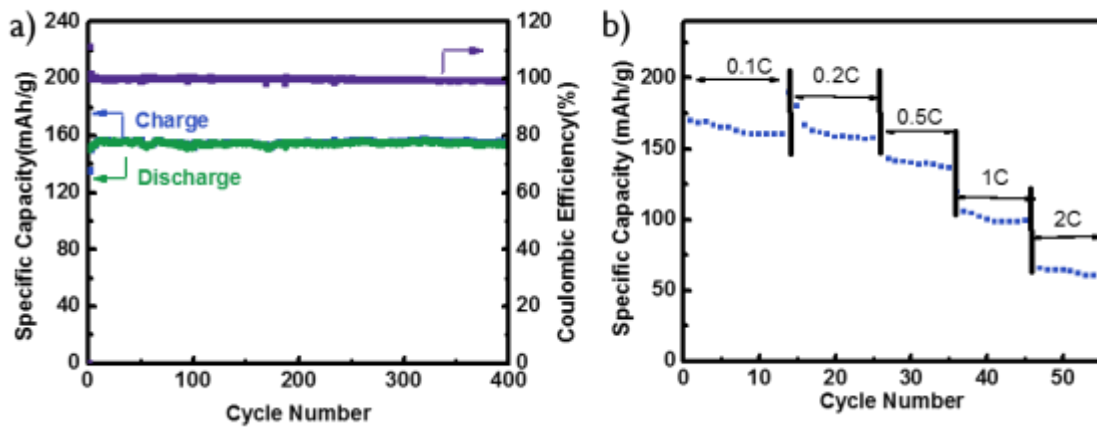


Figure 2-3. a) Cycling stability at C/3 and b) rate capability of a  $TiS_2|Li^+,Mg^{2+}|Mg$  battery

The cycling stability and rate capability of the hybrid Mg battery are shown in Figure 2-3. Due to the simultaneous reversibilities of Mg deposition/dissolution at Mg anode and  $\text{Li}^+$  intercalation/deintercalation at  $\text{TiS}_2$  cathode, as well as the excellent chemical inertness of  $\text{TiS}_2$  toward the complex electrolyte, no capacity decay can be observed for at least 400 cycles with coulombic efficiency as high as 99.5% except for the first few cycles, demonstrating the best cycling stability among reported MIBs and mixed  $\text{Mg}^{2+}/\text{Li}^+$  ion batteries using non- $\text{Mo}_6\text{X}_8$  cathodes. Compared to the MIB using  $\text{Mo}_6\text{X}_8$  cathode, the theoretical specific capacity and specific energy of the mixed-ion battery is 161.0 mAh/g and 209.3 Wh/kg even when the weight of lithium salt was taken into account, which are 32.2% and 56.2% higher than 121.8 mAh/g and 134 Wh/kg of the state-of-the-art MIB. A comparison on specific capacity/specific energy between LIB, MIB and the hybrid battery is given in Figure 2-4. In addition, the hybrid battery inherits the fast kinetics of Li intercalation/deintercalation at cathode, as demonstrated by the high rate performance shown in Figure 2-3b. Hence, the proposed hybrid Mg battery shows an overall superior performance than the traditional MIB.

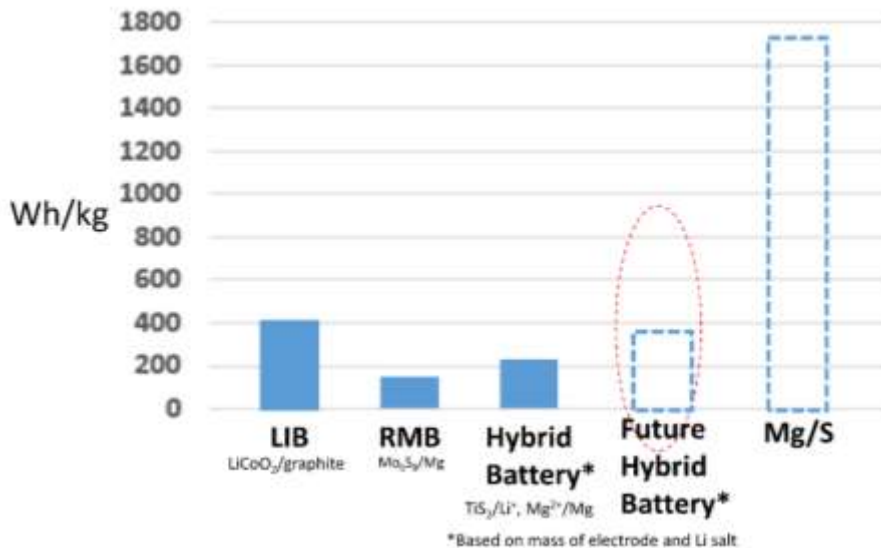


Figure 2-4. Energy Density Comparison of different Battery Chemistries

### **Conclusion**

In conclusion, a highly reversible hybrid battery with a Mg anode and LIB cathode through rational design is reported. In terms of specific capacity, specific energy, cycling stability and rate capability, the reported hybrid  $\text{Mg}^{2+}/\text{Li}^+$  battery demonstrates the best overall performance among reported magnesium-based batteries. The intrinsic challenges of dendrite growth in lithium batteries and poor  $\text{Mg}^{2+}$  insertion/extraction kinetics in MIB have been simultaneously circumvented in this hybrid chemistry. Noteworthy, there is still a huge potential to be exploited for this hybrid battery concept, since recent discoveries of enhanced electrolyte stability on commercially feasible current collectors have made the application of cathodes with higher voltage possible. If a compatible high voltage electrolyte-cathode pair can be found, the specific energy of the hybrid battery could be potentially doubled (385.2Wh/kg). This makes the hybrid battery an alternative that could be even competitive against the mainstream LIB technology (400Wh/kg) (Figure 2-4), not mentioning the advantages of a dendrite-free Mg anode that is free of inert masses (current collector, binder, and conductive additives) and first cycle irreversible reaction associated with SEI formation. Since all  $\text{Li}^+$  is provided by the electrolyte, a high  $\text{Li}^+$  concentration is required for the hybrid battery to function at high capacities.

## Chapter 3 High Power Magnesium/Iodine Chemistry

### Introduction

Extensive efforts have been conducted to improve the reaction kinetics and cycling stability of RMBs. The most successful strategy is to couple  $\text{Li}^+$  intercalation cathodes (e.g.  $\text{TiS}_2$ ,  $\text{LiFePO}_4$  etc.) with a Mg anode in a hybrid  $\text{Mg}^{2+}/\text{Li}^+$  electrolyte so that the clumsy  $\text{Mg}^{2+}$  intercalation can be partially or even completely replaced by fast  $\text{Li}^+$  intercalation.<sup>[71][72][73][74]</sup> However, the energy density of such a hybrid battery is restricted by the Li salt concentration of the electrolyte, which limited its practical application. There are also studies reporting that water can stimulate  $\text{Mg}^{2+}$  intercalation and thus dramatically enhancing the intercalation kinetics by shielding the charge of  $\text{Mg}^{2+}$  via a solvent co-intercalation mechanism,<sup>[75][76][77]</sup> yet the compatibility of Mg anode with water remains a problem. Up until now, there has been no facile strategy that could effectively tackle the troublesome  $\text{Mg}^{2+}$  intercalation issue. A conversion cathode that undergoes two-phase (solid-liquid or liquid-solid) reaction pathway during an electrochemical reaction that does not rely on solid state  $\text{Mg}^{2+}$  diffusion is considered a promising direction.<sup>[78]</sup> The most successful demonstration of this concept is Li/S batteries where a solid-liquid-solid reaction pathway takes place during the reduction of sulfur.<sup>[79]</sup> For Mg batteries,  $\text{I}_2$  serves as a perfect cathode material for illustrating this concept. This is because  $\text{I}_2$  and its partial reduction product,  $\text{Mg}(\text{I}_3)_2$ , have high solubility in ether based electrolytes, but its final reduced product,  $\text{MgI}_2$ , is insoluble (Table 1). Thus an  $\text{I}_2$  cathode is expected to have faster redox reaction kinetics than intercalation cathodes. In addition,  $\text{I}_2$  is able to provide a much higher voltage (2.1 V) and capacity (211 mAh  $\text{g}^{-1}$ ) than  $\text{Mo}_6\text{S}_8$ .

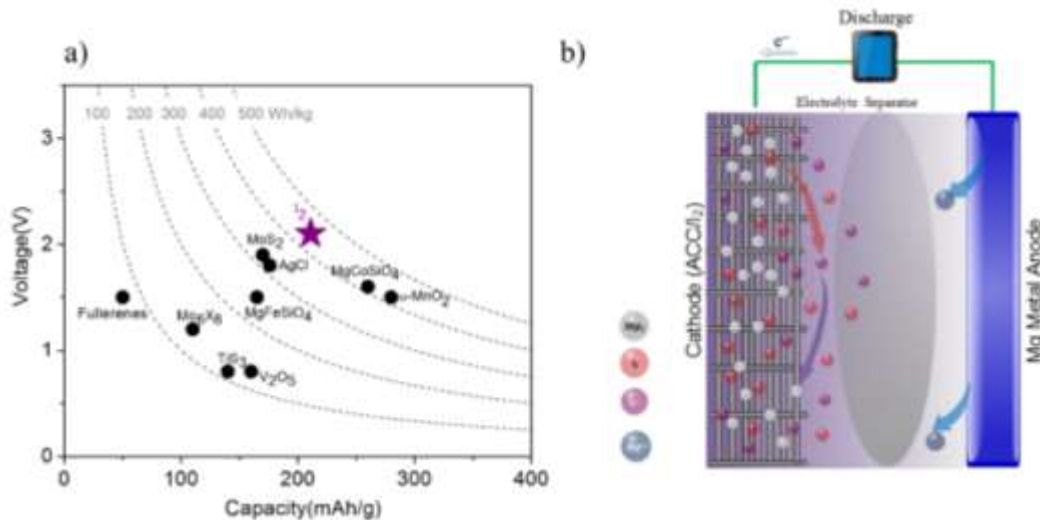


Figure 3-1. (a) The capacity and voltage of typical RMB cathodes; (b) Schematic of rechargeable Mg/I<sub>2</sub> batteries.

Herein, we demonstrate for the first time a rechargeable Mg/I<sub>2</sub> battery. The battery is able to provide capacity close to the theoretical value ( $\sim 200 \text{ mAh g}^{-1}$ ) with an average voltage of 2.0 V at C/4, corresponding to an energy density of  $400 \text{ Wh kg}^{-1}$ . Prolonged cycling shows an excellent stability at C/2 with a capacity retention of 94.6% for 120 cycles. A liquid-solid two-phase reaction mechanism (Figure 3-1b) was validated using spectroscopic and microscopic characterizations. Due to the fast Mg<sup>2+</sup> diffusion in the electrolyte, the ready electron access of iodine species and large interfacial reaction area, the Mg/I<sub>2</sub> battery shows superior rate capability ( $180 \text{ mAh g}^{-1}$  at 0.5C,  $140 \text{ mAh g}^{-1}$  at 1C). This proof-of-concept Mg/I<sub>2</sub> battery demonstrates the feasibility of using a liquid-solid two phase reaction route to address the challenging intercalation kinetics of RMB cathodes. The chemical insights obtained here can

be beneficial for realizing an optimized system, a Mg/I<sub>2</sub> flow battery or other kinds of two-phase reaction RMB cathodes.

Table 3-1. Solubility of different iodine species in Mg/I<sub>2</sub> chemistry (solvent:tetraglyme)

solubility	I <sub>2</sub>	Mg(I <sub>3</sub> ) <sub>2</sub>	MgI <sub>2</sub>
Gram of solute per 100 ml solvent(g)	>75	> 100	< 0.1
Molarity of iodine element (mol L <sup>-1</sup> )	>5.9	>7.6	<0.007

### **Experiment**

**Solubility Measurement:** Sufficient I<sub>2</sub> and MgI<sub>2</sub> were added into TEGDME to form saturated solution. I<sub>3</sub><sup>-</sup>, the most common polyiodide species, was made by adding a mixture of I<sub>2</sub>/MgI<sub>2</sub> (I<sub>2</sub>:MgI<sub>2</sub>=2:1) into the solvent.

**Cathode Fabrication:** Active carbon cloth (ACC)/I<sub>2</sub> cathode was prepared through a melt-diffusion method following a previous report.<sup>[80][81]</sup> The ACC samples (ACC-507-20) were obtained from Kynol Inc. (USA) and were cut to circular discs with a diameter of ~8 mm. Elemental I<sub>2</sub> (99.98%, Sigma-Aldrich) was spread on the bottom of a stainless reactor and then ACC disks were laid on top of the I<sub>2</sub>. The reactor was then sealed and heated to 135 °C for 12 hours. I<sub>2</sub> loading was measured by subtracting the mass of blank ACC from the loaded ACC.

**Electrolyte preparation:** Electrolytes were prepared under pure argon atmosphere in VAC, Inc. glove box (<1 ppm of water and oxygen). The non-nucleophilic Mg electrolyte based on

Magnesium Bis(trimethylsilyl)amide, (HMDS)<sub>2</sub>Mg, was synthesized following a previously reported procedure.<sup>[82]</sup> 3.45g of (HMDS)<sub>2</sub>Mg was dissolved in 20 mL Tetraglyme (TEGDME) with stirring for 24h. After that, 2.67g of AlCl<sub>3</sub> was added slowly into the solution and stirred for 24 h at room temperature. Subsequently, about 0.95 g of MgCl<sub>2</sub>, was added slowly to the solution and stirred for 48 h.

**Electrochemistry:** Mg foil was used as anode. Separators were Whatman Glass fiber or W-scope COD 16. Inconel alloy rod was used as current collector. 100 μL electrolyte was added for each cell. Galvanostatic tests were carried out in Swagelok cell with Arbin Instrument. All applied current was based on the mass of active material (I<sub>2</sub>). 1C rate corresponded to a current density of 211 mA/g<sub>iodine</sub>. All capacities were calculated based on the mass of active material (I<sub>2</sub>) unless otherwise specified.

**Material Characterization:** X-ray diffraction patterns (XRD) were obtained on Bruker Smart 1000 (Bruker AXS Inc., USA) using CuKα radiation. The ACC/I<sub>2</sub> was measured with the TGA equipment (SDT Q600, TA Instruments) and heated in argon atmosphere with a heating rate of 10° C/min. The discharged sample was sealed by a plastic tape from exposure to air and moisture. SEM were conducted using a Hitachi SU-70 field emission scanning electron microscope. XPS analysis was measured using a Kratos Axis 165 spectrometer. Measurements were performed both before and after argon sputtering.

### Calculations

The Gibbs formation energy of MgI<sub>2</sub> at standard conditions (298 K, 1 atm) can be calculated (data from NIST webbook)<sup>[83]</sup>

$$\Delta G_f = \Delta H_f - T \Delta S$$

$$\begin{aligned}
&= -366.94 \frac{\text{kJ}}{\text{mol}} - 298 \text{ K} \\
&\quad \times (-129.67) \frac{\text{J}}{\text{K} \cdot \text{mol}} \\
&= -406.6 \frac{\text{kJ}}{\text{mol}}
\end{aligned}$$

Complete I<sub>2</sub> reduction is accompanied by 2 e<sup>-</sup> transfer per I<sub>2</sub>. Therefore, the theoretical capacity of I<sub>2</sub> is

$$\begin{aligned}
C &= \frac{nF}{M} = \frac{2 \times 26800 \frac{\text{mAh}}{\text{mol}}}{2 \times 126.9 \frac{\text{g}}{\text{mol}}} \\
&= 211.2 \frac{\text{mAh}}{\text{g}}
\end{aligned}$$

The electromotive force (e.m.f) of the Mg/I<sub>2</sub> battery is

$$\begin{aligned}
V &= -\frac{\Delta G_f}{nF} = \frac{406.6 \frac{\text{kJ}}{\text{mol}}}{2 \times 96485 \frac{\text{C}}{\text{mol}}} \\
&= 2.1 \text{ V}
\end{aligned}$$

The theoretical energy density of I<sub>2</sub> cathode is

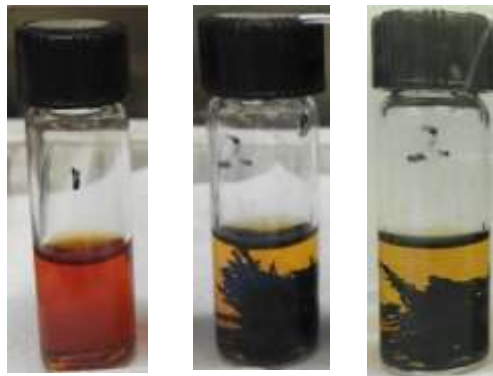
$$E = C \times V = 211.2 \frac{\text{mAh}}{\text{g}} \times 2.1 \text{ V} = 443.5 \text{ Wh/kg}$$

The theoretical energy density of the Mg/I<sub>2</sub> battery based on the total electrode mass is

$$\begin{aligned}
E &= -\frac{\Delta G_f}{M} = \frac{406.6 \frac{\text{kJ}}{\text{mol}}}{278.1 \frac{\text{g}}{\text{mol}}} = 1462.1 \frac{\text{kJ}}{\text{kg}} \\
&= 406 \frac{\text{Wh}}{\text{kg}}
\end{aligned}$$

## Results and Discussion

### ACC/I<sub>2</sub> cathode



(a)

(b)

(c)

Figure 3-2. The images of (a) iodine solution in TEGDME with no ACC; (b) iodine solution in TEGDME after adding ACC for 2 minutes; (c) iodine solution in TEGDME after adding ACC for 12 hours.

Due to the electronic insulating nature of I<sub>2</sub>, it was intentionally impregnated into the pores of active carbon cloth (ACC) through a melt-diffusion method to enhance its electron access following previous reported method.<sup>[80][81]</sup> Meanwhile, ACC can also inhibit the migration of dissolved I<sub>2</sub> towards the Mg anode due to the strong adsorption of I<sub>2</sub> in the ACC pores (Figure 3-2), thus mitigating the expected shuttle effect. The synthesis of the ACC/I<sub>2</sub> cathode is schematically shown in Figure 3-3. In brief, a mixture of ACC and I<sub>2</sub> was first sealed into an

argon filled container, and then heated to 135 °C for 12 hours. At this temperature, the fluid I<sub>2</sub> will be infiltrated into the pores of the ACC through the capillarity effect (the melting point of I<sub>2</sub> is 113.7 °C). The weight ratio of I<sub>2</sub> in the composite electrode can be evaluated with Thermogravimetric Analysis (TGA). For an electrode with I<sub>2</sub> loading 2.8 mg/cm<sup>2</sup>, the mass ratio of I<sub>2</sub> is ~27 %. Scanning Electron Microscopy (SEM) images of the ACC/I<sub>2</sub> cathode demonstrates no residual I<sub>2</sub> on the surface (Figure 3-1bc), and a very uniform distribution of I<sub>2</sub> in carbon can be observed in the energy dispersive spectrum of I (Figure 3-1c). X-ray diffraction (XRD) shows that the I<sub>2</sub> peak disappears after impregnation (Figure 3-1d), suggesting that I<sub>2</sub> loses its long range order structure and is uniformly dispersed inside the pores of the carbon fiber.

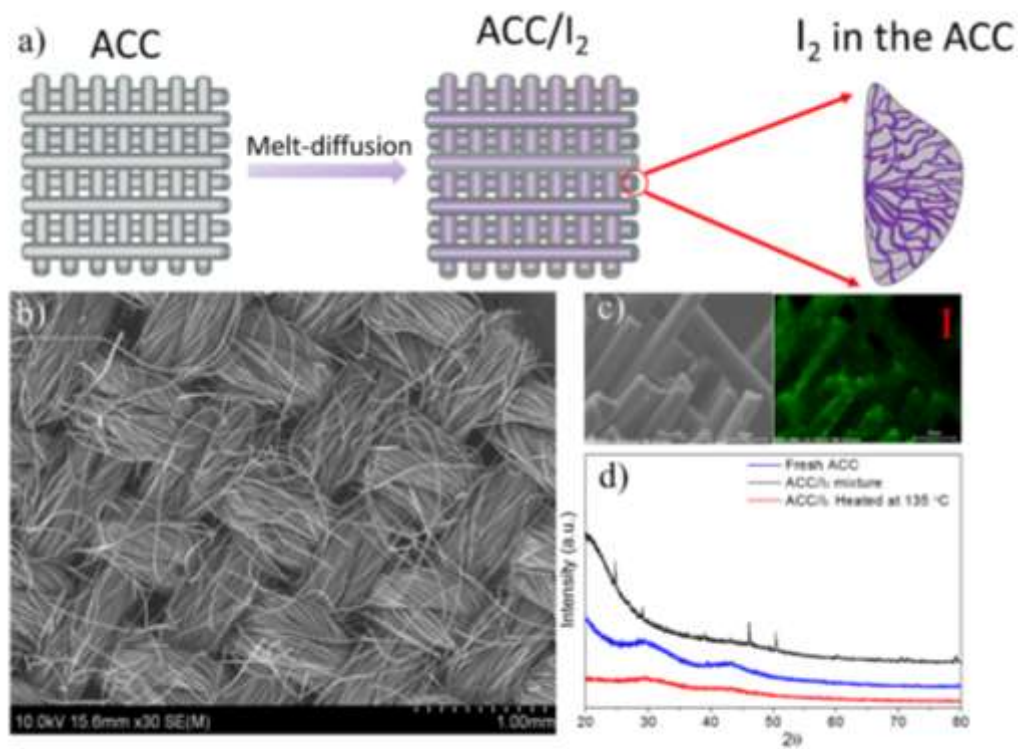


Figure 3-3. (a) Procedure for preparing the ACC/I<sub>2</sub> electrode; (b) SEM and (c) EDS mapping of I in the ACC/I<sub>2</sub> electrode; (d) XRD of ACC/I<sub>2</sub> electrode.

## Electrolyte

The electrolyte was synthesized by reacting magnesium bis(trimethylsilyl)amide ((HMDS)<sub>2</sub>Mg) with aluminum chloride (AlCl<sub>3</sub>) and magnesium chloride (MgCl<sub>2</sub>) in tetraglyme (TEGDME) in-situ. The preparation procedure is given in the Experimental section. For convenience, the electrolyte is abbreviated as Mg-HMDS. The deposition/stripping process of the electrolyte was measured by three-electrode cell and coin cell (Figure 3-4, Figure 3-5).

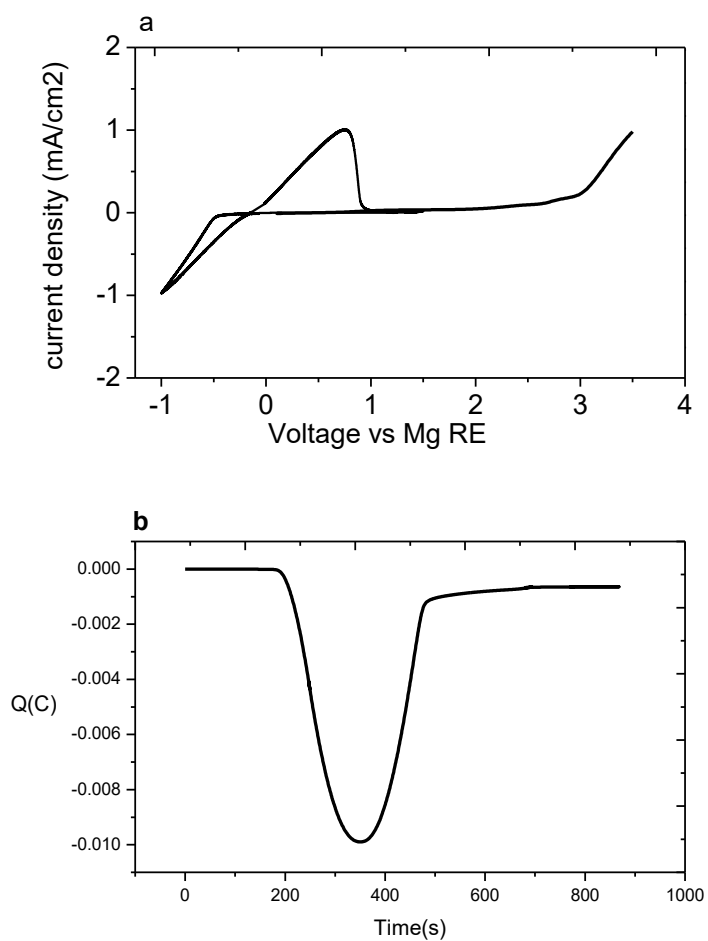
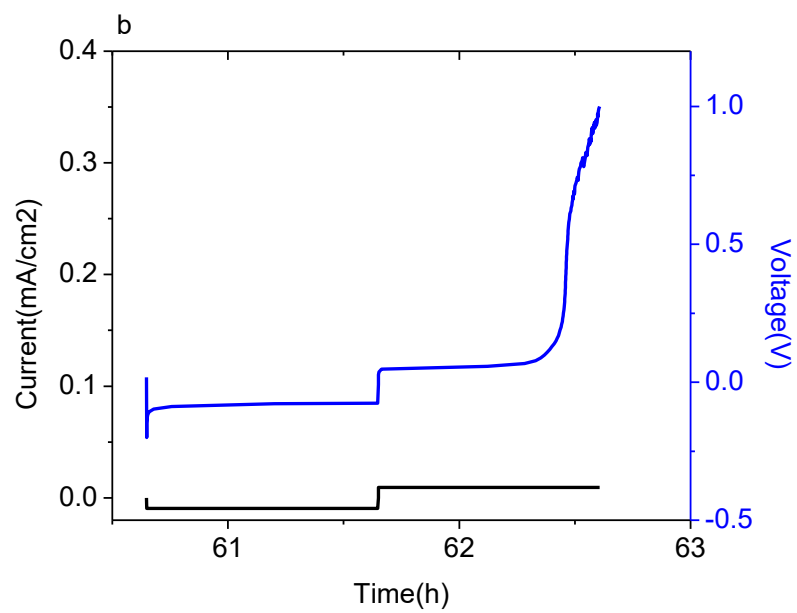
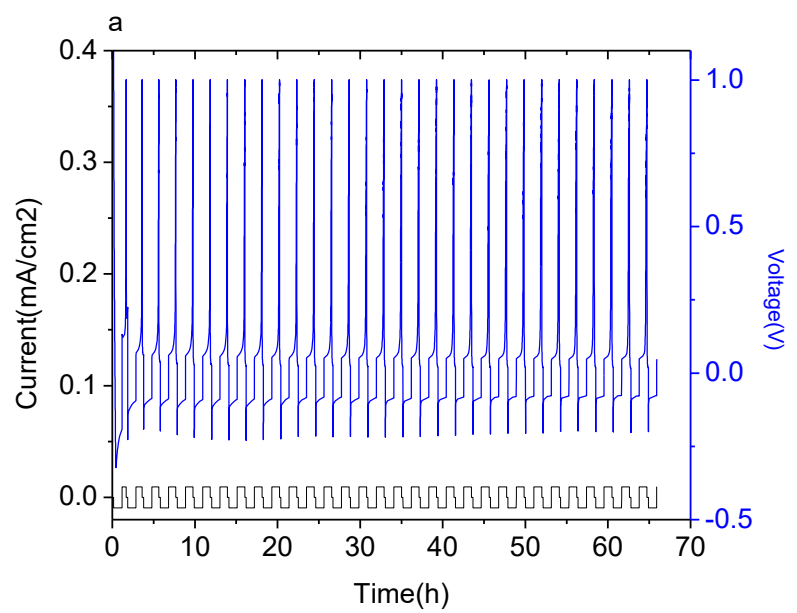


Figure 3-4. a) Cyclic Voltammetry of electrolyte (2M Mg-HMDS in TEGDME). Scan rate: 100 mV/s, voltage:-1V-3.5V. Working electrode: Pt, Reference electrode: Mg foil, Counter electrode: Mg foil. b) capacity-time curve

The basic properties of the electrolyte have been well documented in literature by Karger et al.<sup>[84]</sup>. Here we conducted cyclic voltammeter (CV) test in a three-electrode set-up to illustrate the Mg deposition/dissolution process and its electrochemical stability window. During the cathodic scan, Mg deposition starts at -0.5 V and deposition current increases rapidly with increasing overpotential. During the reverse scan, Mg stripping starts at -0.16 V. The Coulombic Efficiency of the deposition/stripping process can be evaluated by integrating current with time (Figure 3-4b). The Columbic efficiency of 2M Mg-HMDS electrolyte is 94.5%. The electrolyte is quite stable until the voltage reaches > 2.7 V when oxidative current can be observed. Strong decomposition occurs when voltage exceeds 3.0V.



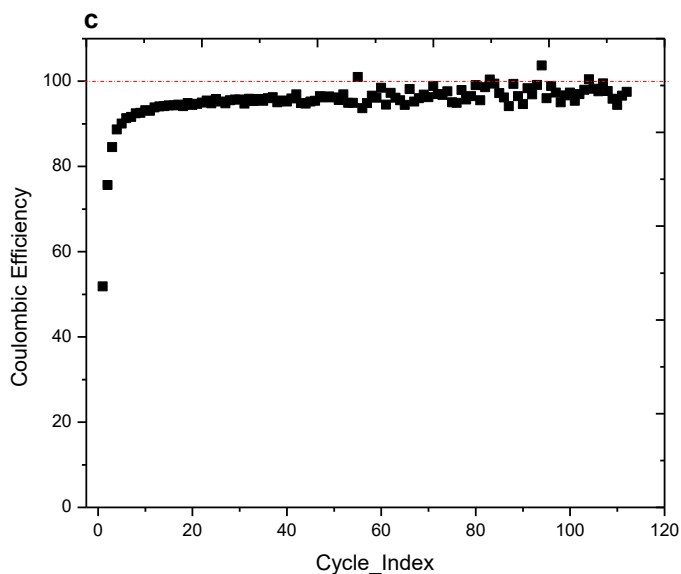


Figure 3-5. a) Galvanostatic discharge/charge of Cu|Mg coin cell. Current: 0.1 mA/cm<sup>2</sup>. Discharge time: 1h. Charge cut-off voltage: 1V; b) A typical discharge/charge curve; c) Coulombic Efficiency for Mg depositing/stripping on Cu foil

We further measured the Mg deposition/stripping process in coin cells using Cu foil as working electrode and Mg foil as anode (Figure 3-5). Figure 3-5a gives the galvanostatic discharge/charge curve. In each cycle Mg was deposited onto Cu foil at a current density of 0.1 mA/cm<sup>2</sup> for 1h, and then stripping occurs at the same current until voltage reaches 1V. A typical discharge (deposition) and charge (stripping) curve is given in Figure 3-5b. During deposition, after the initial large overpotential to initiate the nucleation process, voltage stabilize at an overpotential below 0.1 V. During stripping, overpotential is also below 0.1 V until the end of the charge. Figure 3-5c gives the Coulombic efficiency during cycling. After the initial activation cycles, an efficiency of close to 100% can be achieved.

## Electrochemical Performance

The Mg/I<sub>2</sub> battery was assembled by coupling an ACC/I<sub>2</sub> disk, a glass fiber separator and an Mg foil anode into a Swagelok cell. The typical I<sub>2</sub> loading of the ACC/I<sub>2</sub> disk in the electrochemical tests is ~1.0 mg cm<sup>-2</sup> and the electrolyte volume is 100 μL. A typical discharge/charge curve of the Mg/I<sub>2</sub> cell in 0.5 M Mg-HMDS electrolyte is shown in Figure 3-6. The open-circuit voltage (OCV) of the Mg/I<sub>2</sub> cell is 2.25 V. During discharge, the ACC/I<sub>2</sub> cathode experiences a quick potential drop, and then reaches a plateau at ~1.95 V. The first discharge shows a capacity of ~310 mAh g<sup>-1</sup>, corresponding to an I<sub>2</sub> utilization of ~94.7%, excluding the contribution from the ACC. The Coulombic efficiency is ~75%, suggesting the presence of shuttle effect during charging. Since I<sub>2</sub> and Mg(I<sub>3</sub>)<sub>2</sub> are highly soluble in the electrolyte, it is inevitable to have I<sub>2</sub> loss during charge/discharge, which causes the shuttle effect and results in low Coulombic efficiency.

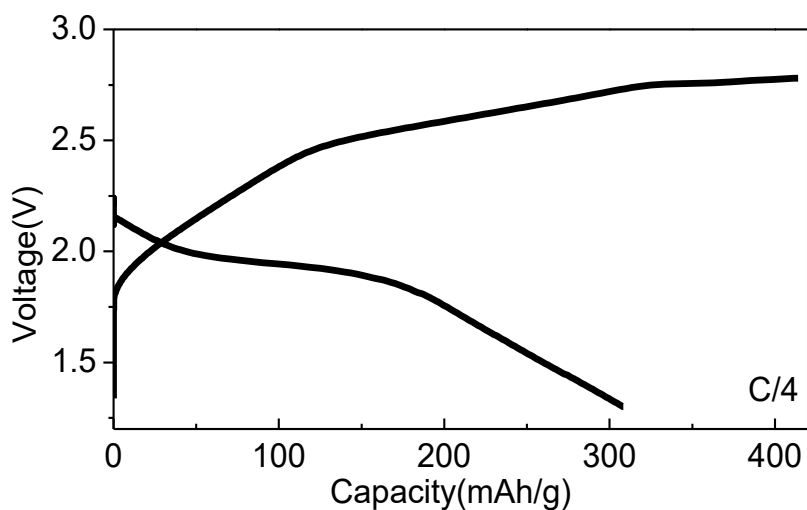


Figure 3-6. The discharge/charge curve of Mg/I<sub>2</sub> battery with ACC/I<sub>2</sub> cathode at C/4 with 0.5 M Mg-HMDS electrolyte.

To mitigate the shuttle effect, an electrolyte with a high salt concentration (2 M Mg-HMDS) was used in the Mg/I<sub>2</sub> battery since concentrated electrolytes were proven effective for this purpose.<sup>[85]</sup> The discharge curves of the ACC/I<sub>2</sub> cathode in this concentrated electrolyte shows a discharge behavior similar to that in the low concentration electrolyte: a short plateau at 2.2 V followed by a long plateau at 1.9 V (Figure 3-7a). However, a remarkable difference can be observed for the charge curves. In the high concentration electrolyte (2 M Mg-HMDS), the ACC/I<sub>2</sub> cathode shows a clear charge plateau at ~2.5 V with a potential spike at the end of the charge (Figure 3-7a), while the ACC/I<sub>2</sub> cathode in the low concentration electrolyte (0.5 M Mg-HMDS) does not show any potential rising at the end of charge even when the capacity exceeded the theoretical value. The shuttle effect of polyiodide was thus effectively mitigated as evidenced from the significantly increased Coulombic efficiency (close to 100%). To understand the reaction mechanism of the Mg/I<sub>2</sub> chemistry, we performed cyclic voltammetry with the Mg/I<sub>2</sub> battery at a slow scan rate of 0.1 mV s<sup>-1</sup> (Figure 3-7b). Two cathodic peaks at ~2.2 V and ~1.8 V can be observed, corresponding to I<sub>2</sub>/ I<sub>3</sub><sup>-</sup> redox couple and I<sub>3</sub><sup>-</sup> / I<sup>-</sup> redox couple, respectively. Two anodic peaks at 2.2 V and 2.7 V can also be observed. Both the charge/discharge curve and cyclic voltammogram prove the good reversibility of the I<sub>2</sub> redox couple in the Mg-HDMS electrolyte. As a result, the Mg/I<sub>2</sub> battery exhibits excellent long-cycle stability, with a high-capacity retention of 94.6% after 120 cycles at a rate of C/2, and could provide a specific capacity of ~180 mAh g<sup>-1</sup> at this rate (Figure 3-7c). Most importantly, the Mg/I<sub>2</sub> battery exhibits a superior rate capability as illustrated in Figure 3-7d, in which all RMB intercalation cathodes reported to date are plotted for comparison. It can even provide a specific capacity of 140 mAh g<sup>-1</sup> at high rate of 1C. Thus the Mg/I<sub>2</sub> battery demonstrates significantly better rate performance than all RMB intercalation cathodes, especially at high current densities

(> 200 mA g<sup>-1</sup>). This observation confirms our hypothesis that a two-phase conversion reaction can dramatically enhance the kinetics of RMB's.

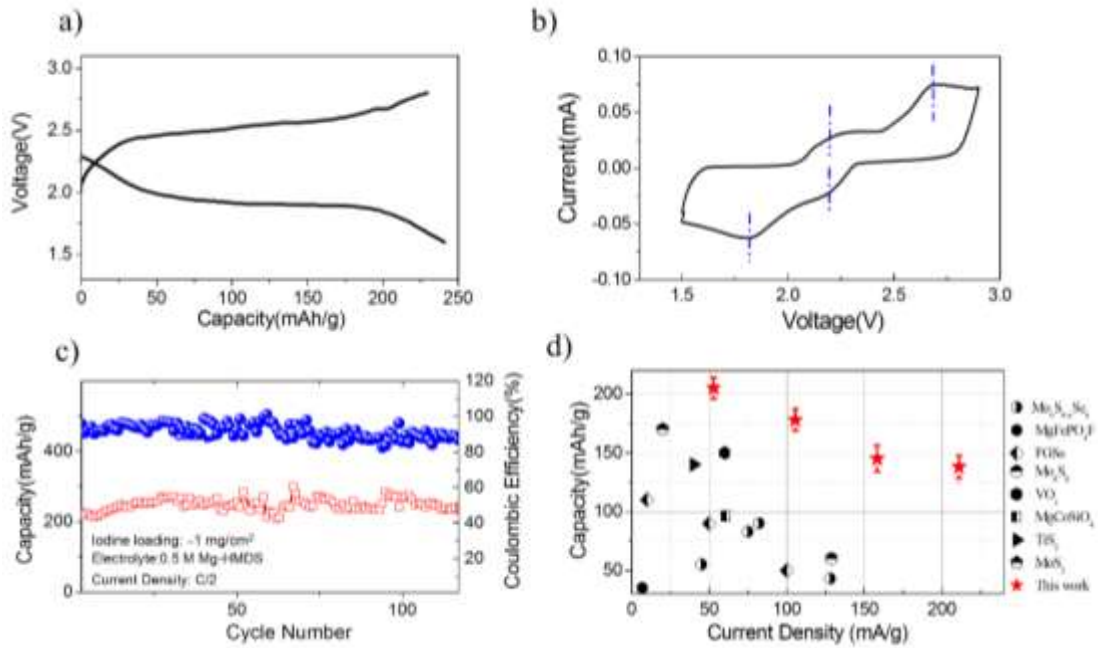


Figure 3-7. (a) Typical charge/discharge curve of the Mg/I<sub>2</sub> battery with ACC/I<sub>2</sub> cathode; (b) Cyclic Voltammogram of the Mg/I<sub>2</sub> battery with ACC/I<sub>2</sub> cathode. Scan rate: 0.1 mV/s; (c) Cycling stability of the Mg/I<sub>2</sub> battery at 0.5 C (105.5 mA/g) with ACC/I<sub>2</sub> cathode; (d) Rate capability of Mg/I<sub>2</sub> battery with ACC/I<sub>2</sub> cathode. Error bar was plotted. The contribution of carbon has been excluded here for assessing the real capacity of iodine redox couple. The rate capability of other cathode materials are plotted for comparison

## Two-phase reaction mechanism

A series of microscopic and spectroscopic measurements were conducted to understand the reaction mechanism of the Mg/I<sub>2</sub> battery. We examined the solubility of different iodine species in etheral solvents (Table 1). I<sub>2</sub> and Mg(I<sub>3</sub>)<sub>2</sub> are highly soluble in TEGDME and the transparent solution quickly turned dark purple once a solute was added, while MgI<sub>2</sub> has negligible solubility in TEGDME and the MgI<sub>2</sub>-TEGDME solution maintains transparent (Figure 3-8).

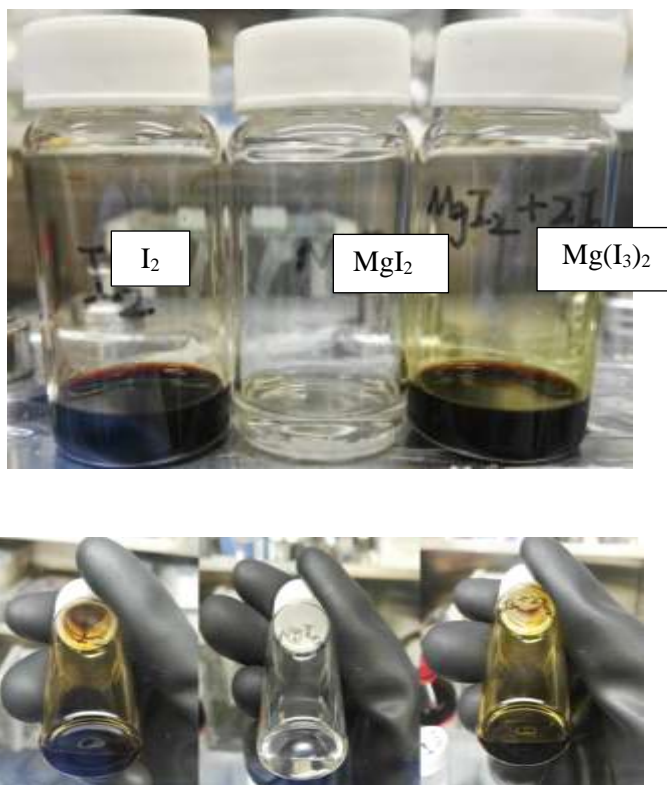


Figure 3-8. Images of saturated I<sub>2</sub>, MgI<sub>2</sub> and Mg(I<sub>3</sub>)<sub>2</sub> solutions. Saturated I<sub>2</sub> and MgI<sub>2</sub> solutions are made by adding sufficient I<sub>2</sub> and MgI<sub>2</sub> into TEGDME until precipitates show. I<sub>3</sub><sup>-</sup>, the most common polyiodide species, was made by adding a mixture of I<sub>2</sub>/MgI<sub>2</sub> (I<sub>2</sub>:MgI<sub>2</sub>=2:1) into the solvent.

A two-electrode flooded cell using ACC as a current collector, 0.15 M I<sub>2</sub> in Mg-HMDS electrolyte as catholyte, and Mg foil as anode was assembled for in-situ observation of the color change of the catholyte during CCCV discharge (constant current and then constant voltage discharge) (Figure 3-9). As can be seen, the dark purple color of the catholyte faded gradually during discharge as I<sub>2</sub> was continuously reduced, and the color nearly disappeared when the cell was discharged to 1.3 V, indicating the soluble I<sub>2</sub>/Mg(I<sub>3</sub>)<sub>2</sub> species were almost entirely converted to the insoluble MgI<sub>2</sub>. After a full discharge, the insoluble MgI<sub>2</sub> product could be observed in the cell. The color change phenomena from I<sub>3</sub><sup>-</sup> to I<sup>-</sup> was also observed in related researches on I<sub>3</sub><sup>-</sup> / I<sup>-</sup> redox.<sup>[86]</sup> Due to lack of standard FT-IR peaks for I<sub>3</sub><sup>-</sup> species, the FT-IR spectra of I<sub>2</sub>, I<sup>-</sup>, and I<sub>3</sub><sup>-</sup> were first characterized as references (Figure 3-9b and Figure 3-9c). The electrolyte was analyzed at different states during discharge using calibrated FT-IR spectroscopy. During discharge, the peak at 1044 cm<sup>-1</sup> was gradually enhanced due to the formation of I<sub>3</sub><sup>-</sup> (Figure 3-9d and Figure 3-9e), since the 1044 cm<sup>-1</sup> peak had been observed in I<sub>3</sub><sup>-</sup> solution (Mg(I<sub>3</sub>)<sub>2</sub> in TEGDME) due to C–O stretching vibrations.<sup>[87]</sup> In addition, a negative shift of two peaks around 1350 cm<sup>-1</sup> and 1250 cm<sup>-1</sup> from 2.2 V to 2.1 V was observed, which is due to the formation of I<sub>3</sub><sup>-</sup>.<sup>[88]</sup> Therefore, I<sub>2</sub> was reduced to I<sub>3</sub><sup>-</sup> after discharging to 2.1 V. After that, those two peaks began to positively shift upon further discharge to 1.5 V. The positive shift could be attributed to the reduction of I<sub>3</sub><sup>-</sup> to I<sup>-</sup> (Figure 3-9b and Figure 3-9c). The FT-IR results demonstrated that iodine undergoes reduction reaction from I<sub>2</sub> to I<sub>3</sub><sup>-</sup> and then to I<sup>-</sup> during discharge in the Mg/I<sub>2</sub> battery.

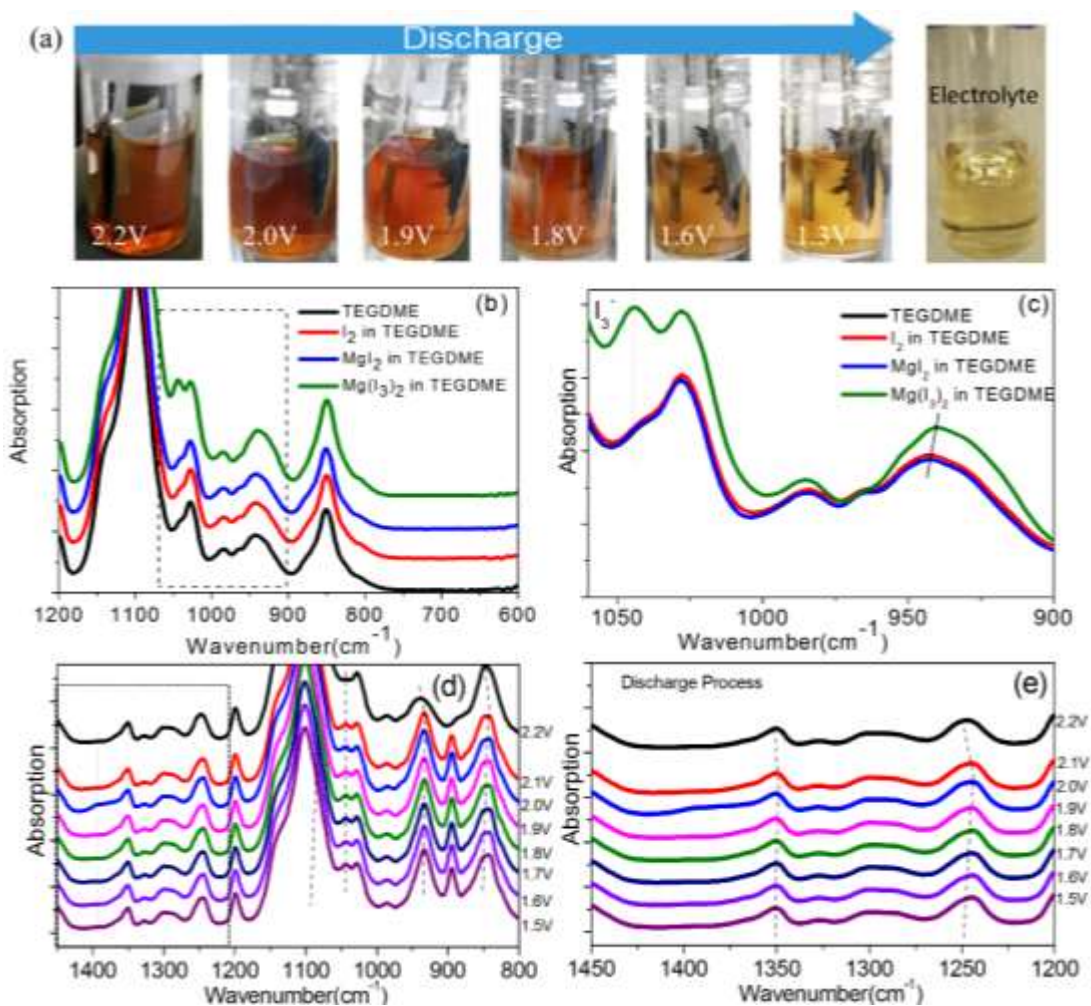


Figure 3-9. (a) Visual observation of the discharge process of Mg/I<sub>2</sub> battery at different discharge stages; the controlled FT-IR spectra of (b) I<sub>2</sub>, MgI<sub>2</sub> and Mg(I<sub>3</sub>)<sub>2</sub> in TEGDME; (c) Magnified view of the regions outlined in (b); (d) the ex-situ FT-IR spectra of Mg/I<sub>2</sub> cell during the discharge process and (e) Magnified view of the regions outlined in (d).

X-ray photoelectron spectroscopy (XPS) was employed to examine the surface chemistry changes of the ACC/I<sub>2</sub> cathode and the Mg anode during discharge/charge at different states. The oxidation states of iodine in pristine ACC/I<sub>2</sub>, fully discharged ACC/I<sub>2</sub>, and fully charged ACC/I<sub>2</sub> were monitored through XPS (Figure 3-10a). The high resolution I 3d spectrum of the

fresh ACC/I<sub>2</sub> cathode is mainly composed of elemental iodine, as evidenced by I 3d<sub>5/2</sub> peak located at 620 eV.<sup>[89]</sup> Two extra I 3d<sub>5/2</sub> peaks located at 622.7 eV and 618.0 eV correspond to I-O bond and I-C bond respectively,<sup>[89]</sup> which may come from the electrode preparation process. After a full discharge to 1.3V, the I 3d<sub>5/2</sub> peak shifts to 619.2 eV, indicating that I<sub>2</sub> has been reduced to a lower oxidation state (I<sup>-</sup>). This result confirms the formation of MgI<sub>2</sub> as the fully discharged product. After a full charge to 2.8 V, I 3d<sub>5/2</sub> peak shifts back to 620.2 eV, suggesting oxidation of MgI<sub>2</sub> back to elemental iodine. High resolution Mg 1s spectrum shows a peak shift from 1303.2 eV to 1303.8 eV after discharge, indicating an increase in Mg's oxidation state (Figure 3-10b). The I 3d spectrum of the Mg anode after discharge evidences the formation of a MgI<sub>2</sub> layer due to the expected shuttle effect (Figure 3-10c).

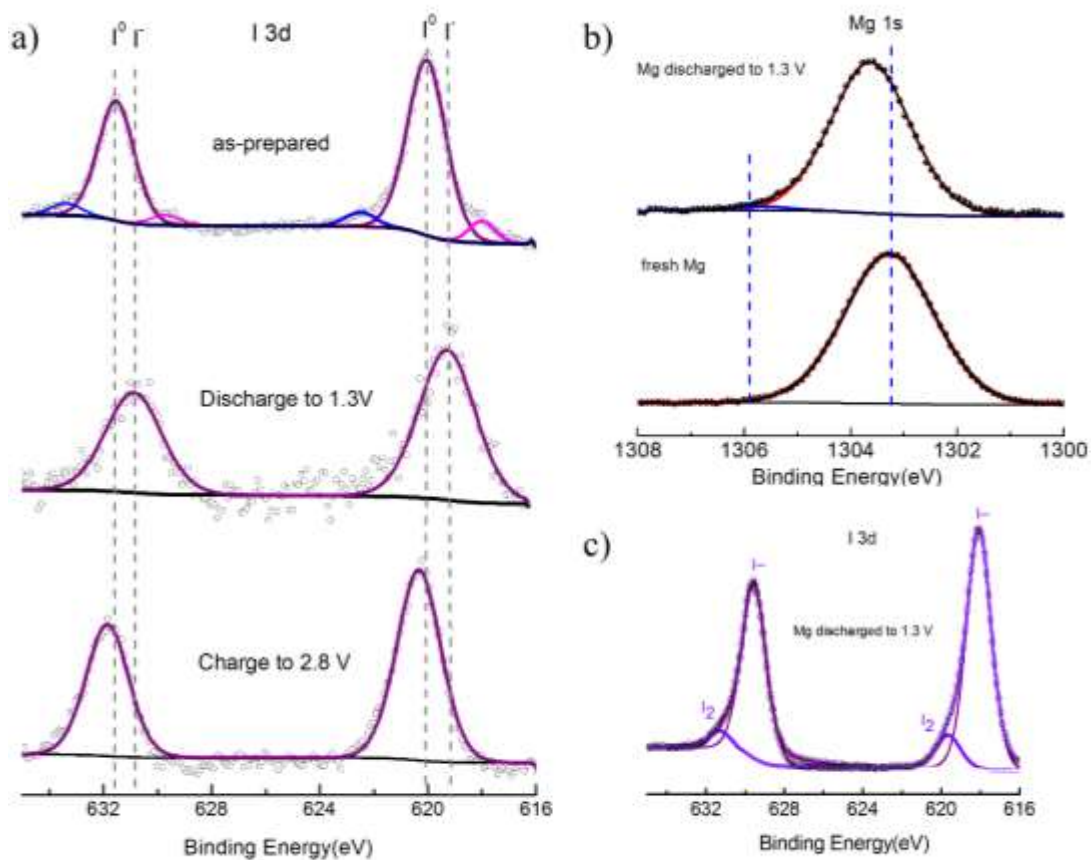
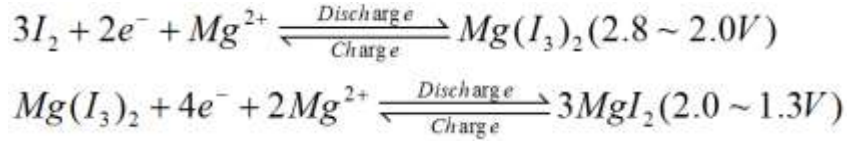


Figure 3-10. (a) High resolution I 3d spectra of the ACC/I<sub>2</sub> cathode; (b) High resolution Mg 1s spectra and (c) high resolution I 3d spectrum of the Mg anode.

We measured the ionic/electronic conductivities of MgI<sub>2</sub>, and the results show it has an ionic conductivity of  $\sim 2.0 \times 10^{-5} \text{ S cm}^{-1}$  and an electronic conductivity of  $\sim 2.1 \times 10^{-9} \text{ S cm}^{-1}$  consistent with previous report.<sup>[90]</sup> Therefore the formed MgI<sub>2</sub> layer is likely to function as a solid electrolyte interface (SEI) that can prevent further reaction of iodine species with Mg. A small elemental I<sub>2</sub> peak is also observed on the Mg anode after discharge, probably due to the

disproportion of  $Mg(I_3)_2$  in the residual electrolyte during sample preparation. Combining the XPS results with the FT-IR results, we can propose the following mechanism for the rechargeable  $Mg/I_2$  batteries:



Electrochemical impedance spectroscopy (EIS) tests were conducted to examine the charge transfer kinetics of the  $Mg/I_2$  battery. As can be expected, the charge transfer resistance of the  $Mg/I_2$  battery is one order lower than that of a rocking-chair battery ( $Mo_6S_8/Mg$ ). This can be explained by the significantly increased quantity of reaction sites in the  $Mg/I_2$  battery, since the liquid-solid two phase reaction can theoretically take place anywhere on the carbon-electrolyte interface. In contrast, in a rocking-chair battery reactions mainly occur on the three-phase interface (active material-carbon-electrolyte), where the active material can readily access both electrons and ions.

The above experimental results have also confirmed our hypothesis that  $I_2$  undergoes a liquid-solid two phase reaction in the  $Mg/I_2$  battery during reduction. This two phase reaction is highly reversible and offers remarkable reaction kinetics due to the bypass of solid state  $Mg^{2+}$  diffusion and the large interfacial area for charge transfer reaction. Due to the high solubility of  $I_2$  and polyiodide, the inevitable shuttle effects leads to low Coulombic efficiency and passivation of the Mg anode. This property of the  $I_2$  redox couple is very similar to that of sulfur in Li/S chemistry. Since the shuttle effect in Li/S chemistry can be significantly mitigated by tailoring the physical and chemical properties of the sulfur host.<sup>[91][92][10][80][93][94][95]</sup> we believe that the polyiodide shuttle effect can also be substantially prevented through host optimization. We show in our preliminary experiment that the shuttle effect can be greatly mitigated by using

micro porous carbon (MPC) with smaller pore size ( $\sim 0.5$  nm).<sup>[96]</sup> The results show clear discharge/charge plateaus and a Coulombic efficiency close to 100 % (Figure 3-11). Self-discharge test of the Mg/I<sub>2</sub> battery using the MPC/I<sub>2</sub> cathode shows negligible open circuit voltage drop for 36 hours (Figure 3-12), indicating the strong I<sub>2</sub> entrapment by using MPC. Further work on tailoring the physical/chemical properties of the host for better I<sub>2</sub> entrapment is still ongoing. In theory all effective methods used in Li/S batteries can be adopted in Mg/I<sub>2</sub> batteries. For example, increasing the salt concentration in electrolytes can effectively reduce the shuttle effect and increase the Coulombic efficiency (Figure 3-7a). Moreover, due to the high reversibility of the I<sub>2</sub> redox couple in the Mg-HDMS electrolyte and the high solubility of I<sub>2</sub> and polyiodide, a semi-flow battery can be constructed based on the Mg/I<sub>2</sub> chemistry. The flooded cell results (Figure 3-9a) have justified this feasibility and detailed work is also ongoing in our lab.

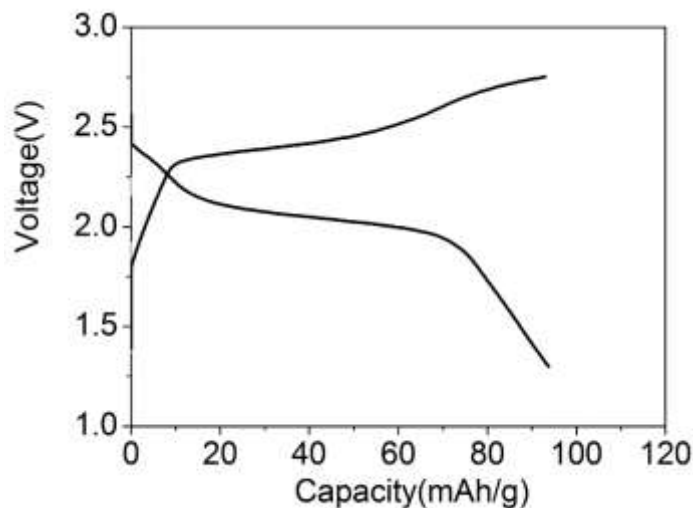


Figure 3-11. The discharge/charge curve of Mg/I<sub>2</sub> battery based on MPC/I<sub>2</sub> cathode at C/4.

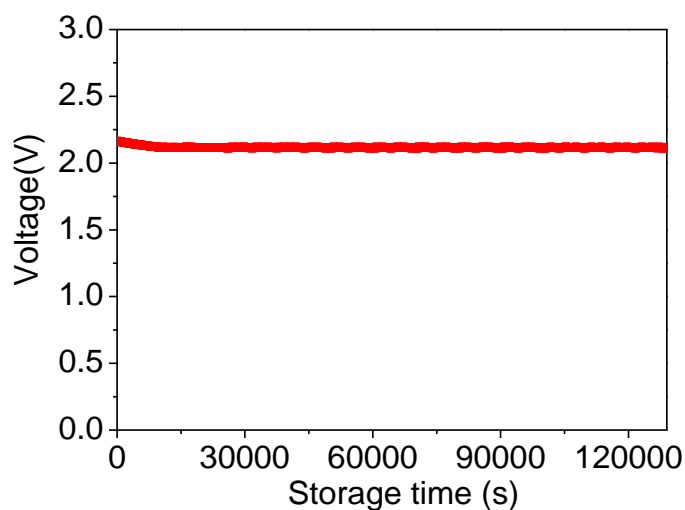


Figure 3-12. The self-discharge test on fresh Mg/I<sub>2</sub> cell based on MPC/I<sub>2</sub> cathode. The OCV of the cells was monitored to evaluate the shuttle effect of the cell.

### **Conclusion**

In summary, we demonstrated for the first time a rechargeable Mg/I<sub>2</sub> chemistry. Compared with traditional RMBs using intercalation cathodes, the I<sub>2</sub> cathode provided a high operating voltage (~2.0 V) and a much higher obtainable energy density (~400 Wh kg<sup>-1</sup>). More importantly, the liquid-solid reaction ensures remarkable reaction kinetics and reversibility mainly due to its free of the solid state Mg<sup>2+</sup> diffusion, which has been considered as a major hurdle for the development of cathode materials for RMBs. The shuttle effect due to the high solubility of I<sub>2</sub> and polyiodide can be effectively mitigated through host optimization and/or electrolyte optimization. The chemical insights obtained in this work will guide the future design of rechargeable Mg/I<sub>2</sub> battery or semi-flow battery. Above all, the successful demonstration of this proof-of-concept Mg/I<sub>2</sub> undoubtedly opens a new avenue for future

development of high performance RMB cathodes by utilizing soluble redox couples whose reactions do not rely on solid state  $\text{Mg}^{2+}$  diffusion.

# Chapter 4 Magnesium/Sulfur Battery: Thermodynamics and Kinetics

## Introduction

Since the hybrid battery, in which high voltage intercalation cathode can be used, requires a large electrolyte volume to work at high capacity, we shift our focus to high capacity conversion cathode, bearing the goal of increasing the energy density of rechargeable Mg battery. As a high capacity cathode material (1,675 mAh/g), sulfur has attracted intense interest in Li-S and Na-S systems.<sup>[10]</sup> Because the reduction of sulfur in the presence of cations ( $\text{Li}^+$ ,  $\text{Na}^+$  or  $\text{Mg}^{2+}$ ) is non-topotactic and does not depend on solid-state ion transport, use of sulfur cathodes could presumably yield a fast cathode reaction for RMBs. Realization of a Mg/S battery is also of great interest because the full cell theoretical capacity could achieve up to 957 mAh/(g-total electrode mass) with an average voltage of 1.77 V as estimated based on the Gibbs formation energy of magnesium sulfide, -341.8 kJ/mol. The theoretical specific energy is hence 1722 Wh/kg, over four times of that of a commercial  $\text{LiCoO}_2$ /graphite cell and close to that of a  $\text{Li}_2\text{S}$ /silicon cell (Table 1), making it an exceptionally promising battery chemistry for large scale ( $10^3\sim 10^6$  Wh) applications like electric vehicle and grid storage that require both high energy density and low cost.

Motivated by this promise, several concept Mg/S cells were brought up after the first sulfur compatible electrolyte was invented in 2011.<sup>[57][82][81][97][98]</sup> They showed capacities of 800-1200 mAh/gs and major discharge plateaus at 1.1-1.7 V for tens of cycles, proving the feasibility of rechargeable Mg/S battery. Despite of the promising electrochemical results, there are many

fundamental questions remained unanswered regarding the Mg/S chemistry. One example is the strong discrepancies among the reported discharge curves. In Fichtner and Wang's work, two discharge plateaus at ~1.6 V and ~1.0 V were observed<sup>[82][81][99]</sup>; however, there is only one discharge plateau in other studies.<sup>[57][97][100]</sup> Such discrepancy of discharge curves also exists for studies from the same group using different sulfur/carbon composites.<sup>[82][99]</sup> Binary Mg-S or ternary Mg-S-electrolyte phase diagram would help solve the mystery, because it governs phase transition when mixing magnesium with sulfur and therefore determines the staging and potential of the discharge curve. Unfortunately, there is no available study in literature. Another intriguing phenomena is the kinetics of the Mg/S cells. Due to the high charge density of Mg<sup>2+</sup>, the insertion/extraction of Mg<sup>2+</sup> is usually accompanied by large overpotential, especially for oxides and oxygen (usually > 1.0 V).<sup>[39][38][58]</sup> In contrast, recent results show that the overpotential of the dominant voltage plateau in Mg/S and Mg/Se cells is remarkable lower than that of oxides or oxygen.<sup>[81][97][101]</sup> The fast Mg reaction kinetics ensures minimum voltage loss, which is critical for Mg cathode since the voltage of its corresponding full cell is already low compared to its Li counterpart. Although the solid-liquid two phase reaction was suggested as a probable cause for the fast kinetics, it remains opaque if any other factors exist and how they interact with each other. Compared to the sister Li/S system, the studies on Mg/S are still of preliminary nature. Understanding of the aforementioned fundamental issues is therefore especially important, since it provides the basics for realizing practical cells starting from these concept work.

In this work, we aim to fill this knowledge gap by investigating the thermodynamics and kinetics of sulfur cathode in magnesium chemistry and the associated reaction mechanism. Combining both experimental and computational results, we are able to examine the reaction

pathway, as well as reveal the kinetics limitation of Mg/S chemistry for rechargeable batteries.

### Experiment

**Electrode Fabrication.** We use sulfur/carbon composite electrode as the cathode in this study. The composite cathode was prepared with a melt-diffusion method by impregnating sulfur into the pores of carbon. The microporous carbon is active carbon cloth (ACC-507-20, Kynol Inc. USA). The cloth were cut to circular discs with a diameter of 8 mm. Elemental sulfur (99.98%, Sigma-Aldrich) was spread on the bottom of a stainless reactor and then the ACC disks were laid on top of the sulfur powder. The reactor was then sealed and heated to 155 C for 12 h. Sulfur loading was measured by subtracting the mass of blank ACC from the loaded ACC.

**Electrolytes Preparation.** Electrolytes were prepared under pure argon atmosphere in MBraun, Inc. glovebox (<1 ppm of water and oxygen). MgTFSI<sub>2</sub> (99%, Solvonic, France) was dried in vacuum at 240 °C for >10 hours and dimethoxyethane (DME, 99%, Sigma-Aldrich) was dried with molecular sieves for >24 hours prior to use. Ultra-dry MgCl<sub>2</sub>(99%, Sigma-Aldrich) was directly used without further treatment. The simple salt electrolyte was prepared by dissolving MgTFSI<sub>2</sub> into DME and stirring overnight. The complex electrolyte was prepared by adding MgTFSI<sub>2</sub> and MgCl<sub>2</sub> in the molar ratio of 2:1 into DME and stirring overnight. The concentration both simple and complex both refers to the concentration of MgTFSI<sub>2</sub> salt. For example, 0.25 M complex electrolyte refers to a mixture of 0.25M MgTFSI<sub>2</sub>-0.5M MgCl<sub>2</sub>.

**Electrochemical Measurement.** The coulombic titration of sulfur cathode was performed in three-electrode T-cells with sulfur/carbon composite as the working electrode and Mg disks

(Goodfellow, Inc.) for both the reference and counter electrodes. The cells were discharged at certain current for given time and then rest. This operation was repeated until the voltages reached cut-off condition. The open circuit voltage after each rest was recorded as the equilibrium voltage.

**Mg Polysulfide Synthesizing.** We use solution phase synthesis method, which was commonly used in Li/S battery research to make polysulfide, to make Mg polysulfide in this work. 80 mM (25.6 mg) of sulfur powder (99.9%, Sigma-Aldrich) was first added into 10 mL of DME in eight glass vials. Then different amount of Mg powder (325 mesh, Sigma-Aldrich), i.e. 0, 10, 13.3, 20, 40 and 80 mM,

**Material Characterization:** XPS was collected with a Kratos Axis 165 spectrometer operating in hybrid mode, using monochomatized Al K $\alpha$  X-rays (1486.7 eV). Survey and high resolution spectra were collected with pass energies of 160 eV and 40 eV respectively. Peak fitting was done using CASA XPS software. Data was fit with a Shirley background using peaks with a 30 % Lorentzian, 70 % Gaussian product function. Peaks fit to the C 1s were constrained to have the same full width at half maximum (FWHM). S 2p spectra were fit with spin-orbit split 2p 3/2 and 2p 1/2 doublets, constrained by 1.16 eV separation consistent with spin-orbit splitting, a characteristic 2:1 area ratio and the same FWHM for each doublets. The carbon/sulfur composite cathode samples were soaked in DME for 24 hours then washed three times in order to remove any residual electrolyte on the surface before XPS measurement. The preparation and transfer of samples were all done in Ar environment. Because the C 1s spectrum of the carbon/sulfur composite exhibits a broad, asymmetric tail towards higher binding energy, the typical feature of sp<sup>2</sup> carbon, we use 284.0 eV for C 1s as the reference to

calibrate the XPS data. MgS was synthesized by ball milling equimolar amount of Mg powder (325 mesh) with sulfur powder under Ar. 284.8 eV was used for C 1s as the reference to calibrate the XPS data of synthesized MgS.

**AIMD calculations:** The *ab initio* molecular dynamics (AIMD) simulations in this study are performed using the VASP package.<sup>[102][103][104]</sup> The ion–electron interaction is described with the Projector Augmented Wave (PAW) method, and the exchange–correlation energy is described by the functional of the Perdew–Burke–Ernzerhof (PBE) form of the generalized gradient approximation (GGA). Plane wave energy cut-off of 400 eV are chosen and a minimal  $\Gamma$ -centered 1 x 1 x 1 k-point grid is used.

**Amorphous structure:** In the present calculations, amorphous MgS<sub>x</sub> (x=1, 2, 3, 4, 6, 8,15) model structures, containing 96 atoms, are prepared by AIMD within VASP. These structures are heated up to a temperature above the melting temperature (e.g., 2500 K). At this temperature, the systems are equilibrated for 5000 MD steps with a 1 fs time step and then rapidly quenched to 300 K at a rate of 0.6 K/fs, along with volume optimization. Here, the temperature is controlled via velocity rescaling.

**Dynamic behaviors:** The obtained samples are then heated up to the desired temperature 1073 K by velocity scaling over 1000 time steps (2 ps) in the ensemble with a constant volume Nosé–Hoover thermostat. And the MD simulations for dynamic behaviors are then performed in the NVT ensemble for 40 ps with the time steps of 2 fs. The diffusion coefficient is defined as the mean square displacement (MSD) over time:

$$D = \lim_{t \rightarrow \infty} \frac{\langle [r(t)]^2 \rangle}{6t}$$

The average mean square displacement  $\langle [r(t)]^2 \rangle$  was calculated as:

$$\langle [r(t)]^2 \rangle = \frac{1}{N} \sum_i \langle [r_i(t + t_0)]^2 - [r_i(t_0)]^2 \rangle$$

Where  $r_i(t)$  is the displacement of the  $i$ -th Li ion at time  $t$ . The calculated displacement  $r_i(t)$  is the displacement of an individual Li atom. And  $N$  is the total number of ion in the system. The coefficient is finally attained from the slope of the average MSD vs. time plot for each temperature, from which an Arrhenius plot is obtained which yielded the activation energy. The MSD are calculated by pymatgen<sup>[105][106]</sup> and the structural matching results are visualized using VESTA<sup>[107]</sup> in this study.

### Thermodynamics

The thermodynamics of sulfur electrode at different magnesianation degree was investigated by coulombic titration with galvanostatic intermittent titration technique (GITT). The equilibrium potential curves of sulfur are given in Figure 4-1(red). To exclude the effect of anode overpotential, the titration experiment was performed in three-electrode T-cells. The open circuit voltage is ~2.4 V vs. Mg RE. Similar to Li/S system,<sup>49</sup> the discharge profile shows clear staging features, indicating several different processes occurring in a successive order upon sulfur reduction. Three consecutive regions can be clearly identified: a convex slope (2.4-1.5V), a plateau (1.5V) and a concave slope (1.5V-0.5V). The cumulative discharge capacity is close to the theoretical capacity, indicating the full sulfur utilization at quasi-equilibrium

condition. This full sulfur utilization is also realized by discharging at gradually decreasing current (Figure 4-2). We can also deduce that kinetic limitation is one main reason why previous Mg/S cells were unable to deliver full capacity.<sup>242526</sup> In contrast to discharge, complete recharge is not possible even under the same equilibrium condition, implying the formed (poly)sulfide is electrochemically difficult to be oxidized. This could partially explain Zhao-Karger's finding that the oxidative scan (charge) of cyclic voltammetry (CV) shows much weaker peak than the cathodic scan (discharge).<sup>42</sup> On the other hand, the staging phenomena becomes not so clear during charge, suggesting the charge reaction does not mirror the discharge one. An equilibrium curve which only discharges to 1.4V, just below the long plateau, was also obtained (Figure 4-1c). In contrast to Figure 1a, a much high reversibility is achieved, ~86% of the discharge capacity is recovered compared to that of ~60% when the cell is discharged to 0.5V. This result suggests that the reaction reversibility is highly dependent on the final discharge product. Similarly, the charge shows a slope curve which does not mirror the discharge plateau.

The electrons transfer per S atom is also plotted in Figure 4-1a with the corresponding polysulfide intermediates labeled. Note the chemical formulas used here are more for describing the average composition of the intermediates instead of the real chemical species. In this work, we focus on elaborating the thermodynamics of sulfur/sulfide redox couple and the corresponding kinetics. Probing the chemical signatures of polysulfide, which are challenging,<sup>50515253545556</sup> will be the focus of future studies. The three consecutive regions correspond to I)  $S_8 \rightarrow MgS_x, x > 8$  transition, II)  $MgS_8 \rightarrow MgS_2$  transition and III)  $MgS_2 \rightarrow MgS$  transition, respectively. Interestingly, Li/S cells also show similar staging phenomena in ether electrolyte. Due to the large solubility of long-chain lithium polysulfide species in ether solvents<sup>57</sup>, the discharge of Li/S cell undergoes in four steps: I)  $S_8 \rightarrow Li_2S_8$  (solid-liquid two

phase reaction, a short plateau at 2.2-2.3V), II)  $\text{Li}_2\text{S}_8 \rightarrow \text{Li}_2\text{S}_4$  (solution phase reaction, a slope in 2.3-2.0V), III)  $\text{Li}_2\text{S}_4 \rightarrow \text{Li}_2\text{S}_2 + \text{Li}_2\text{S}$  (liquid-solid two phase reaction, a long plateau at 2.0V) and IV)  $\text{Li}_2\text{S}_2 \rightarrow \text{Li}_2\text{S}$  (solid phase reaction, a slope in 2.0-1.5V).<sup>49</sup>

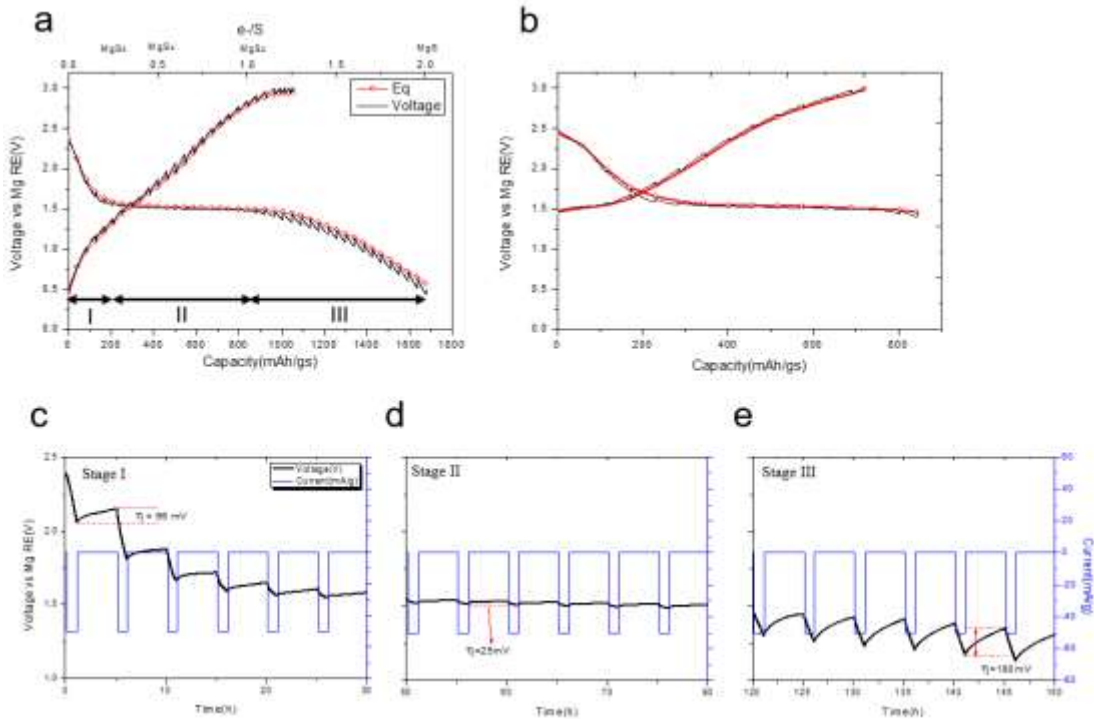


Figure 4-1. Coulombic Titration Experiment. a) Thermodynamic equilibrium curve discharged to 0.5V. Current: 50 mA/gs, Rest 4 hours; b) thermodynamic equilibrium curve discharged to 1.4V. Current 50 mA/gs, Rest 1 hour. c-e) Transient voltage during Coulombic Titration experiment. Sulfur loading: 1 mg/cm<sup>2</sup>, sulfur/carbon ratio= 0.125. Red: equilibrium curve; black: transient voltage; blue: current.

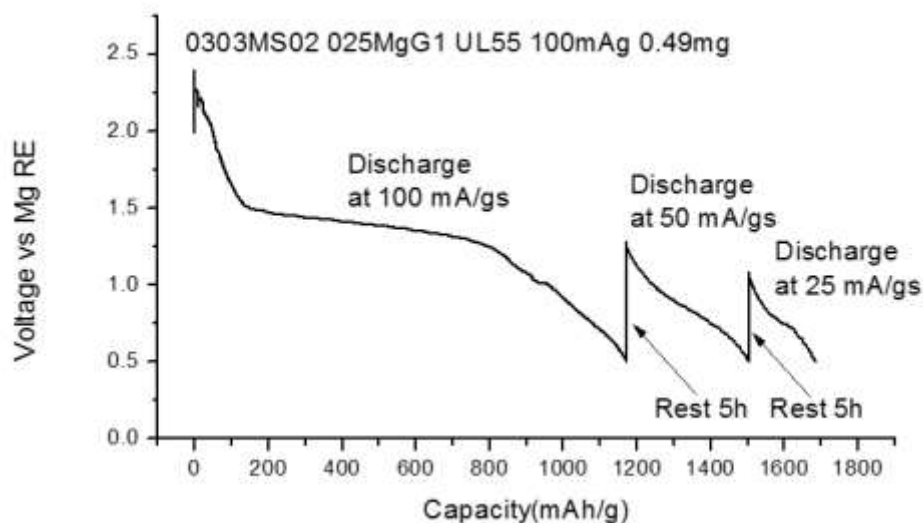


Figure 4-2. First discharge of sulfur cathode in simple electrolyte at gradually decreasing current.

To examine if there is any polysulfide dissolved during battery discharge, we use Electrospray-Ionization Mass Spectroscopy (ESI-MS) to study the electrolyte before and after discharge (Figure 4-3). The possible polysulfide species are given in Table 4-1. The result suggests only long-chained polysulfide ( $S_{x}^{2-}, x=8,7,6,5$ ) and  $S_3^{\cdot-}$  radical are soluble while short-chained polysulfide ( $S_{x}^{2-}, x=3,2$ ) are not. The presence of  $S_4^{2-}$  cannot be determined from the ESI-MS results since its position overlaps with the signals from electrolyte. This evidence indicates that discharge is accompanied by the dissolution of long-chained polysulfide. To measure the solubility of polysulfide, we added '6.25 mM' Mg powder into electrolyte containing 50 mM sulfur (corresponding to '6.25 mM'  $MgS_8$ ). After several days stirring, some Mg powder dissolves and the transparent sulfur solution turns yellow, implying the formation of polysulfide. Nevertheless, Mg powder does not fully dissolve, suggesting the solubility of

polysulfide (in the unit of atomic sulfur) is < 50 mM. Note this solubility is at least two orders of magnitude less than the solubility of  $\text{Li}_2\text{S}_8$  (6046 mM) in ether electrolyte.<sup>57</sup>

Table 4-1. The possible polysulfide species in electrolytes

Polysulfide species	m/z (amu)
$\text{S}_5^{2-}$	79.93
$\text{S}_3^-, \text{S}_6^{2-}$	95.91
$\text{S}_7^{2-}$	111.90
$\text{S}_8^{2-}$	127.88
TFSI fragment ions	m/z (amu)
$\text{CF}_3\text{SO}_2\text{NH}^-$	147.96801

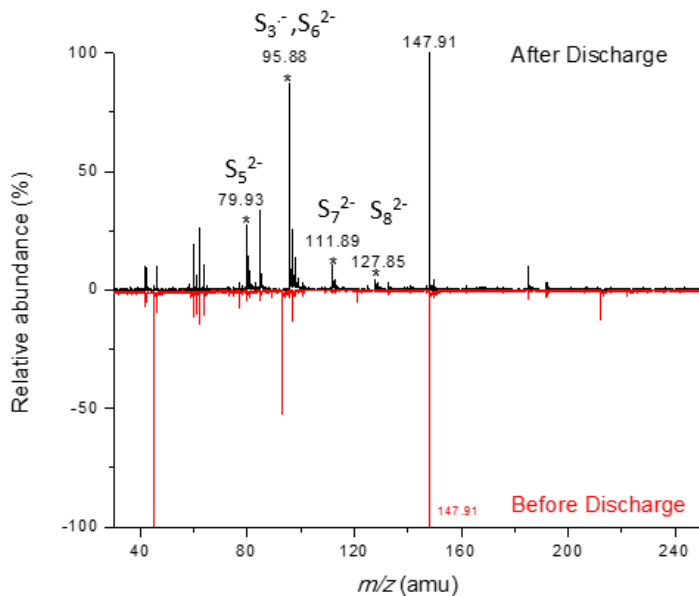


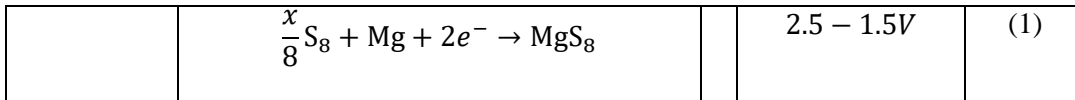
Figure 4-3. ESI-MS spectra of electrolyte before and after discharge.

Despite of the dissolution of polysulfide, it is surprising that the charging does not show the plateau of polysulfide shuttle effect. A possible scenario is suggested to explain this

phenomenon: the solubility of Mg polysulfide is low so that the shuttle effect (a form of self-discharge during charging) is not significant. This scenario is widely seen in Li/S battery using concentrated electrolyte<sup>58</sup> or ionic liquid electrolyte<sup>5759</sup> where polysulfide shuttle is inhibited due to the low solubility of polysulfide. Meanwhile, since shuttle effect is intrinsically the chemical discharge inside the battery, the rate of this chemical self-discharge process is dependent on how fast metal anode can reduce the polysulfide species. Given the less reductive nature of Mg compared to Li, it is reasonable to expect that polysulfide reduction on Mg surface is much slower than that on Li surface. Moreover, the passivation of Mg surface by insoluble short-chained polysulfide can further impedes the reaction.

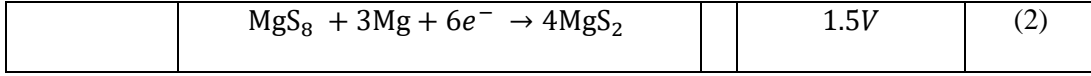
Based on these observations, we proposed the following reaction pathway during the reduction of sulfur.

**Stage I:** A single phase reaction from elemental sulfur to MgS<sub>8</sub>. In this stage, sulfur is partially reduced and forms a long chain polysulfide. The sloping voltage also indicates that solubility of polysulfide (in the unit of atomic sulfur) does not increase remarkably during the reduction, otherwise a short plateau for solid-liquid two phase reaction would appear similar to the S<sub>8</sub>-Li<sub>2</sub>S<sub>8</sub> plateau in ether electrolyte Li/S battery. The decreasing voltage indicates the declining chemical potential of Mg<sup>2+</sup> in the MgS<sub>x</sub>.

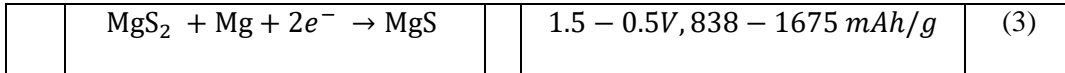


**Stage II:** According to Gibbs phase rule, the long plateau (invariant of chemical potential) indicates the co-existence of two phases. Therefore, the reaction is a phase transition reaction from soluble long-chained polysulfide to insoluble short-chained polysulfide. Considering the solubility of polysulfide (< 50 mM in the unit of atomic sulfur) is small, there should be parallel reduction reactions occurring in the solid state. Based on the calculated composition, the overall

reaction is given in Equation 3. The reaction in this stage is accompanied by the shortening of polysulfide chain.



**Stage III:** According to the calculated compositions, the overall reaction in Stage III is given in Equation 3. Since no  $\text{S}_2^{2-}$  or  $\text{S}^{2-}$  can be found in the electrolyte, the reaction occurs all in the solid state. Similar to the Stage IV in Li/S system,<sup>49</sup> this step occurs with very slow kinetics. Large overpotential was clearly observed in the coulombic titration experiment. The transient voltages in each stage are plotted in Figure 4-1c-e for better illustrating the overpotential. For Stages I and II, cell voltages are close to or have already reached equilibrium four hours after each discharge. In Stage III, however, cell voltages are still under dynamic change even after four hours rest. Therefore, the red curve in this Stage does not refer to the equilibrium voltage of the Mg/S cell, but we keep the terminology for convenience.



To verify the proposed mechanism, we tried different post-modern analysis to acquire the chemical signatures of the intermediate products. X-ray diffraction was not useful since sulfur is in a highly dispersed state after entering the pores in the sulfur/carbon composite,<sup>60</sup> and Raman spectroscopy also failed since the spectrum is dominated by carbon signal and the signal-to-noise ratio of the interested region (Raman shift: 100-800  $\text{cm}^{-1}$ ) is quite low for making any useful deduction. In this work, X-ray photoelectron spectroscopy (XPS) was used. The S 2p spectra at different states are given in Figure 4-4. MgS powder was synthesized and its S 2p peak was measured for identifying the binding energy of  $\text{S}^{2-}$ .

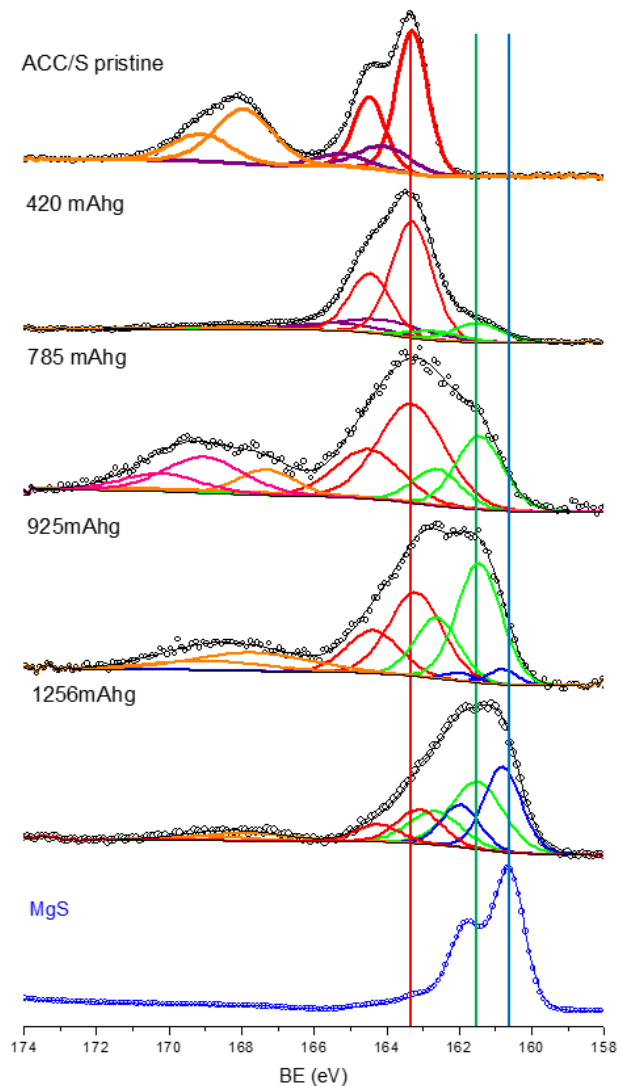


Figure 4-4. High Resolution XPS S 2p Spectra. a) Sulfur Cathode at Different States; b) MgS; c) Schematic for the reaction mechanism

S 2p spectra were fitted with constrained spin-orbit split doublets with equal full width at half maximum. The pristine carbon/sulfur composite shows two S  $2p_{3/2}$  peaks located at 163.3 eV (red) and 164.1 eV (purple) corresponding to elemental sulfur, in agreement with previous study.<sup>36</sup> The S  $2p_{3/2}$  peaks at binding energy >166.0 eV (orange and pink) correspond to  $SO_x$ , which may result from the residual salt from the electrolyte (TFSI<sup>-</sup> anion) or samples' short

exposure to air. To remove the surface contamination, all samples recovered from disassembled cells were etched by Ar<sup>+</sup> sputtering for 30 minutes. Upon discharge to 420 mAh/gs, a new S 2p<sub>3/2</sub> peak at ~161.5 eV (green) appears, indicating the formation of Mg polysulfide MgS<sub>x,x=2-8</sub> in which the oxidation state of sulfur is between -2 (160.6 eV) and 0 (163.3eV). Further discharge to 785 mAh/gs strengthens this peak and continuously weakening the peaks of elemental sulfur. Another new peak emerges after the discharge capacity (925 mAh/gs) exceeds half of the theoretical capacity, suggesting the formation of MgS. Continuous discharge to 1256 mAh/gs leads to growth of MgS peak and weakening of both elemental sulfur peak and MgS<sub>x</sub> peak. Upon charge, the peaks corresponding to MgS<sub>x</sub> and MgS disappear and the peak corresponding to elemental sulfur is recovered. The broadening of this peak signals an increasing degree of disorder in sulfur, which is a result of the magnesianation and demagnesianation process.

The XPS results confirms the formation of Mg polysulfide MgS<sub>x,x=2-8</sub> as the intermediate product and the formation of MgS as the final product, and the recovery of elemental sulfur peak in the fully charged sample evidences the discharge/charge (electrochemical reduction of S and oxidation of MgS<sub>x</sub>) is a chemically reversible process. The fact that MgS peak (blue) does not appear until capacity exceeds 840 mAh/gs agrees with the above proposed mechanism that the chain length shortening of Mg polysulfide occurs in Stage II. Meanwhile, the continuous growth of MgS peak and weakening of MgS<sub>x</sub> peak after capacity exceeds 840 mAh/gs is in accordance with the notion that Stage III involves phase transition from MgS<sub>x</sub> to MgS. The fact that elemental sulfur peak does not disappear even at capacity exceeding 840 mAh/gs was also observed in studies using similar carbon/sulfur composites cathode.<sup>6162</sup> We speculate this could be due to the presence of some elemental sulfur far from the reaction frontier(the electrode/electrolyte interface). This is possible if the rate of phase transformation

( $S \rightarrow MgS_x \rightarrow MgS$ ) and  $Mg^{2+}$  diffusion does not overtake the rate of magnesianation. As a consequence, a non-uniform distribution of reactions products perpendicular to the reaction frontier can be expected with Mg rich phase laying outside of Mg poor phase. Nevertheless, a continuous declining intensity of S  $2p_{3/2}$  peak located at 163.3 eV suggests the consumption of elemental sulfur during battery discharge.

Since the solubility of polysulfide is low, most polysulfide should exist in the solid state. To reveal their structures, we performed AIMD simulation, in which a  $MgS_x$  ( $x=1, 2, 3, 4, 6, 8$ ) model containing 96 atoms are heated, then given sufficient time to equilibrate and finally quenched to room temperature. The obtained structures are illustrated in Figure 4-5. All polysulfides ( $MgS_{x,x=2-8}$ ) have amorphous structures in which Mg atoms are randomly distributed in the S matrix and lack long-range order, implying that the crystalline  $MgS_x$  does not exist. However, an ordered structure with orthorhombic lattice emerges when the composition reaches MgS. The calculation result here coincides with previous experimental observations that  $Li_2S$  is the only crystalline products during sulfur reduction in Li/S system,<sup>63</sup> implying the similarity of sulfur speciation in Li and Mg chemistries.

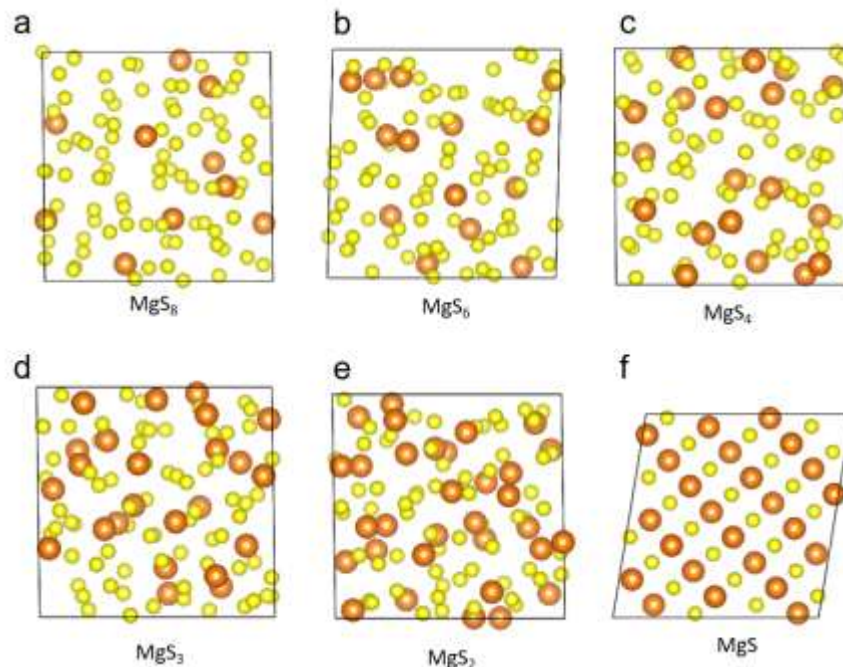


Figure 4-5. Structure of MgS<sub>x</sub> by DFT calculation.

To further examine the structural evolution, the partial pair distribution functions (PDF) are calculated for characterizing the distance of Mg-S and S-S pair for each amorphous MgS<sub>x, x=2-8</sub> and crystal MgS (Figure 4-6). At very low Mg concentration (MgS<sub>8</sub>), the nearest S-S pair has a distance of 2.0 Å (black, i) and the second nearest S-S pair (black, ii) has distance of 3.4 Å. At highest Mg concentration (MgS), the nearest Mg-S pair (red, i) has a distance of 2.6 Å, the second nearest Mg-S pair (red, ii) has a distance of 4.4 Å and the nearest S-S pair (blue) has a distance of 3.6 Å. These values are in good agreement with the experimental S-S and Mg-S pair distances (Table 4-2 and Figure 4-7). It demonstrates that the calculated PDFs well reflect the experimental bond lengths of the two ending composition during the magnesianation of sulfur. Starting from MgS<sub>8</sub>, increasing Mg concentration leads to a continuous peak sharpening of the nearest Mg-S pair (red, i), indicating an increasing number of Mg-S bond. Meanwhile, the nearest S-S pair (black, i) persistently weakens, implying the breaking of S-S bonds. When the

composition reaches MgS, all S-S bond at 2.0 Å is gone. Upon magnesiation, the second nearest S-S pair (black, ii) is gradually replaced by the S-S pair in MgS at 3.6 Å (blue). The whole process during magnesiation is summarized in the schematic (Figure 4-8). Red refers to Mg-S bond and black refers to S-S bond. Clearly, with the increasing of Mg concentration, the numbers of Mg-S bond grows while the number of S-S bond declines. These results well supports the conclusion made above that during magnesiation polysulfide  $MgS_x$  is experiencing a continuous chain shortening and eventually turns into MgS.

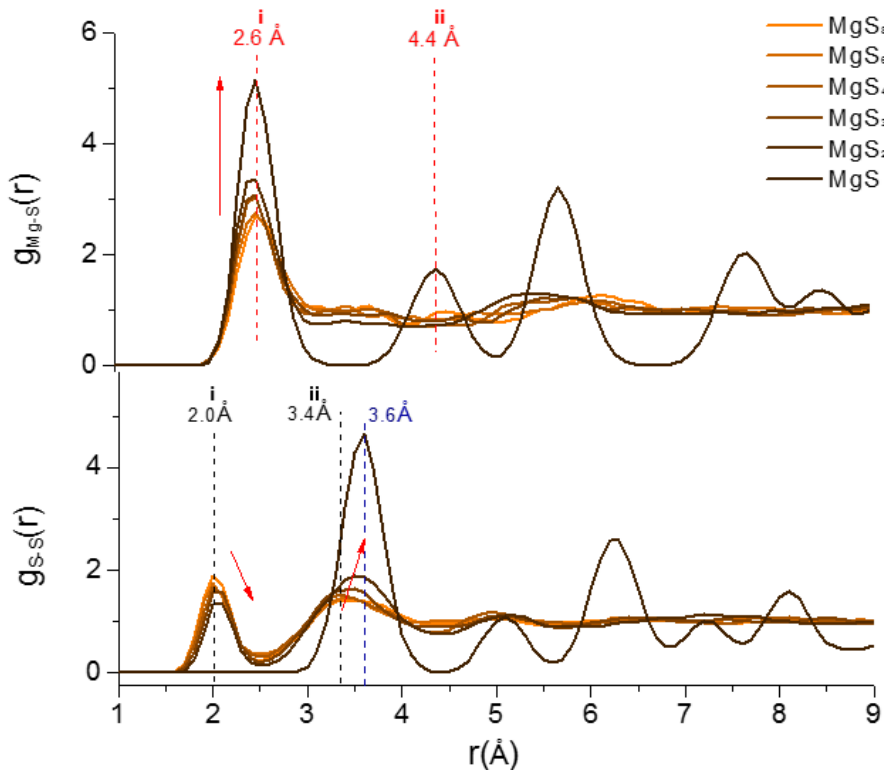


Figure 4-6 Pair Distribution Functions (PDF) of  $MgS_{x,x=8-2}$  and MgS

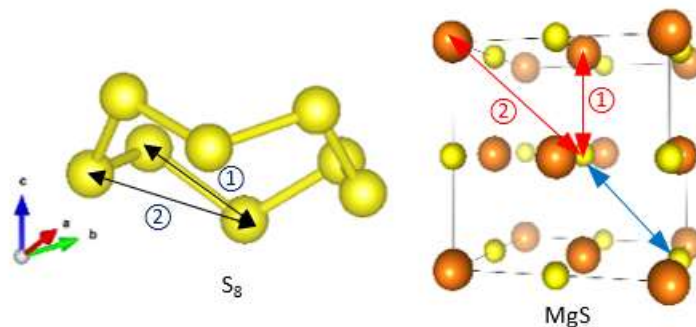


Figure 4-7. First and second closest atom pair in sulfur molecule and MgS crystal

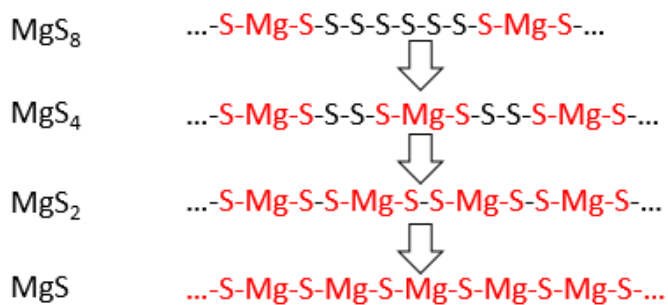


Figure 4-8. Chain length shortening scheme of  $\text{MgS}_{x,x-8-2}$

Table 4-2. The experimental bond length of sulfur and MgS (unit: Å)

	S-S (i)	S-S (ii)	Mg-S(i)	Mg-S(ii)
Sulfur	2.06	3.36	-	-
MgS	3.68	5.20	2.60	4.50

### Kinetics

Charge transfer reaction in batteries is a heterogeneous reaction that can be described by a general equation:  $M^{z+} + ze^- + H \rightarrow MH$ , in which  $M^{z+}$  is the electroactive ion,  $e^-$  is the electron and  $H$  is the ion-electron pair host. Usually, charge transfer reaction occurs at the

triple-phase-interface of the electron conducting network (carbon), ion conducting network (electrolyte) and the host (active material) where the all reactants ( $M^{z+}$ ,  $e^-$ , and  $H$ ) are readily available. It can also occur at two-phase interface in some cases, for example, if the host is soluble in the electrolyte (Li/S battery), or if the host is highly electronic conductive (LiCoO<sub>2</sub>). Due to its insulating nature, sulfur is usually mixed with carbon to enhance its availability of electrons. In the above thermodynamics analysis, we use carbon/sulfur composite with sufficient carbon (S/C=0.12) to assure the electronic conductivity so that we can reach complete sulfur utilization and have a comprehensive view of the Mg-S phase diagram. By comparing the equilibrium potential (red) with transient voltage (black) we obtained the overpotentials of the whole electrochemical reaction (Figure 4-1 c-e). The three-stage reaction pathway can also be identified from the overpotential map (Figure 4-9a). Overall, the reaction kinetics is much more facile in Stage I and II than in Stage III. The overpotential declines from 95 mV and reaches into a plateau of 25 mV after entering Stage II. In Stage II, the overpotential is small (25 mV). However, the overpotential climbs up by one order of magnitude (from 25mV to 180 mV) as long as reaction enters Stage III, implying the sluggish kinetics of the solid state reaction.

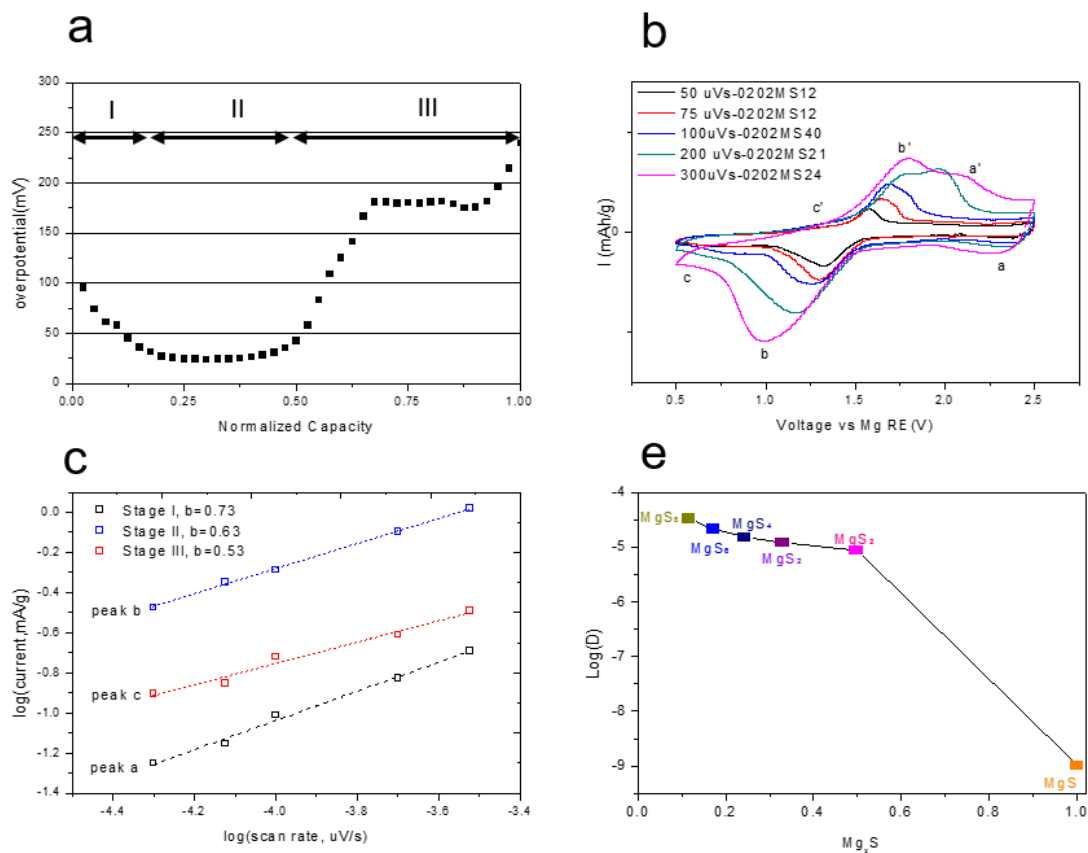


Figure 4-9. Kinetics Study by Experiment and AIMD Simulation. a) overpotential during coulombic titration tests; b) Cyclic Voltammetry curves at different scan rates; c) kinetic fitting of the peak current by using equation  $i=avb$ ; d) Diffusivity of  $Mg^{2+}$  in  $MgS_x$ ,  $x=8-1$  obtained through AIMD simulation.

To examine the rate limiting step during sulfur reduction, we adopt the electrochemical technique developed by Lindquist,<sup>64</sup> in which the contributions from surface process (Faradic or Non-Faradic) and ion diffusion to the overall electrode capacity can be quantified and separated due to their different response mode upon same scanning voltage stimulus. Cyclic voltammometry experiments at various scanning rates were first performed (Figure 4-9b). Three cathodic peaks (a, b, c) were observed with three corresponding anodic peaks (a',b',c'). Clearly,

they correspond to Stage I, Stage II and Stage III respectively. The current densities of the reduction peaks a, b and c at different sweeping rates are plotted in Figure 4-9c with log axis and linear trends can be observed for all three peaks. The kinetic dominating process of the redox reaction can be determined from b-value by fitting equation  $i = av^b$ , in which  $b=1$  suggests a surface-controlled reaction and  $b=0.5$  suggests a diffusion-controlled reaction. The b values for stages I and II are 0.73 and 0.63, which suggests the reactions are mix-controlled. This also agrees with the aforementioned notion that the dissolution of long-chain polysulfide triggers a liquid-solid reaction that is in parallel with the solid state reduction. The b value for stage III is 0.53, indicating a diffusion controlled reaction, which confirms the solid state reaction route in this stage.

Several steps occur during the magnesiation of sulfur. First,  $Mg^{2+}$  diffuses from the bulk electrolyte into the pores and then arrives at the interface. Then, charge transfer reaction occurs and Mg bonds with sulfur molecules. Part of the formed polysulfide will dissolve into the electrolyte but the rest stays in the solid phase. As a result, a Mg-rich phase forms near the interface, while far away from the interface lays a Mg-poor phase. Concentration gradient (or in the viewpoint of energy, chemical potential gradient) of Mg will drive Mg to diffuse away from the interface and move into Mg-poor phase. The time for diffusion depends on the thickness of the solid layer on the wall of pores, determined by the carbon type and sulfur loading, and the chemical diffusion coefficient of  $Mg^{2+}$  (Diffusion time scale:  $\tau = L/\tilde{D}$ ). Slow diffusion (long diffusion time) causes Mg to accumulate near interface, which imposes a large energy barrier for following Mg insertion and impedes the further magnesiation reaction. This kinetic view is in accordance with the above XPS results, in which the co-existence of Mg-poor phases(S,  $MgS_x$ ) and Mg-rich phase (MgS) are detected.

To understand the dynamic behavior of Mg diffusion in the solid state, we performed *ab initio* molecular dynamics (AIMD) simulations. Within the simulation time (40 ps), Mg shows higher total MSD (Mean square displacement) at lower Mg concentration, suggesting the faster movement of  $\text{Mg}^{2+}$  at low Mg concentration. The diffusivity of  $\text{Mg}^{2+}$  was also calculated (Figure 4-9e). The highest diffusivity is seen when magnesianation just starts ( $\text{MgS}_8$ ,  $D=3.38 \times 10^{-5} \text{ cm}^2/\text{s}$ ), then it declines monotonically as more  $\text{Mg}^{2+}$  is inserted, but the decrease is within one order of magnitude before the composition reaches  $\text{MgS}_2$  ( $D=0.87 \times 10^{-5} \text{ cm}^2/\text{s}$ ). However, a four order of magnitude drop is seen when the composition reaches  $\text{MgS}$  ( $D= 1.04 \times 10^{-9} \text{ cm}^2/\text{s}$ ). This dramatic decline partially explains the rapid rise of overpotential when the reaction enters into Stage III. Once  $\text{MgS}$  is formed at the interface,  $\text{Mg}^{2+}$  diffusion becomes extremely difficult and a large driving force is required to motivate  $\text{Mg}^{2+}$  to diffuse away from interface and into the bulk. The extremely low diffusivity in  $\text{MgS}$  is not surprising since we find that  $\text{MgS}$ , once formed, tends to crystallize while  $\text{MgS}_{x,x=8-2}$  tends to maintain an amorphous structure.

To examine the influence of electronic conductivity on the kinetics, we obtained the coulombic titration curves of sulfur/carbon composites with increasing sulfur/carbon ratio (Figure 4-10). The three-stage reaction pattern is maintained in all curves, however, the overall capacity decreases severely with increasing sulfur/carbon ratio, as only  $\sim 430 \text{ mAh/g}$ s capacity can be obtained when sulfur/carbon ratio=1.00. The capacity contributed by each Stage is compared in Figure 4-10b. Stages I and III diminish severer than Stage II: Stage I becomes negligible when sulfur/carbon ratio reaches 0.45 and Stage III becomes negligible when sulfur/carbon ratio reaches 1.00.

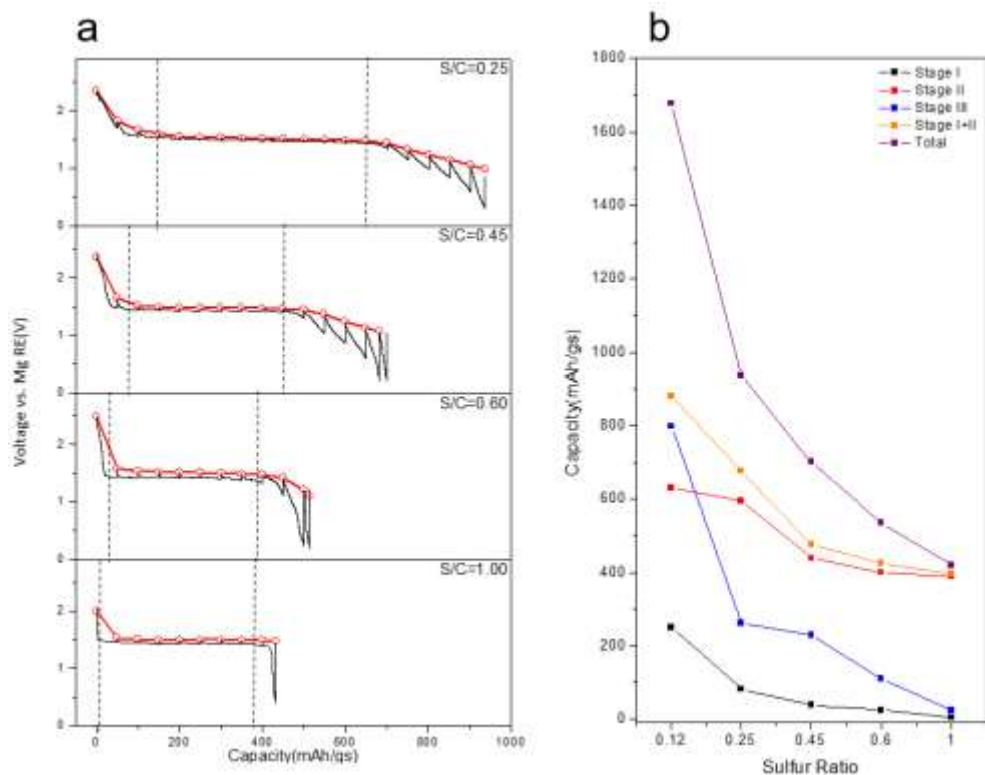


Figure 4-10. The Influence of Electronic Conductivity. a) Coulombic titration curves of sulfur/carbon composite cathode with different sulfur loading. The sulfur weight ratio is given in the figure. b) the contributed capacities of each Stage

Assuming sulfur is uniformly distributed in the porous carbon, the average thickness of sulfur layer in the pores increases with sulfur/carbon ratio. It is notable that the overpotentials in Stages I and II are small for all sulfur/carbon ratios, which suggests the fast kinetics in Stages I and II are insensitive to the amount of carbon, i.e. the transport of electrons from carbon to the reaction frontier is not rate limiting. This is probably due to 1) the soluble long-chain polysulfide, once formed, can easily diffuse to a fresh carbon surface where electrons are more readily available, and then 2) it can function as a redox mediator, which carries electrons and delivers them to other reaction sites by a disproportionation reaction. Similar argument is also confirmed in Li/S batteries in recent years.<sup>6566</sup> Bearing this in mind, it is surprising at first

glance that the capacity in Stages I and II (838 mAh/g) is not fully utilized. A close look shows that the discharge enters Stage III earlier at higher sulfur/carbon ratio. Unlike Li/S chemistry, in which the sufficient dissolution of the formed intermediate polysulfide (whose solubility is 6046 mM) enables continuous exposure of inner sulfur, the partial dissolution of polysulfide (whose solubility  $< 50$  mM) in Mg/S chemistry renders most  $\text{MgS}_x, x \geq 2$  to be in the solid state. Once MgS forms at the interface, large overpotential is needed to drive Mg and electron to transport through it, leading to sharp voltage drop in Stage III and early termination of discharge. Nevertheless, the equilibrium potential (red), determined by the average Mg concentration, is close to the 1.5V plateau but far away from the cut-off voltage. Despite the specific capacity (mAh/g) in Stage III decreases by several orders with increasing sulfur/carbon ratio, we found that the capacity (mAh) in this Stage is on the same order. This suggests similar thickness of MgS layer for different sulfur/carbon ratios at the end of discharge. Another factor that can contribute to the severe capacity decrease at high sulfur/carbon ratio is the non-uniform sulfur distribution. At sulfur/carbon ratio, sulfur tends to accumulate on the surface of carbon fiber instead of diffusing into the deep of the pores due to the small pore size ( $< 2$  nm). This can exaggerate the above effect for sulfur on the surface and reduce the utilization of sulfur deep inside.

### Electrochemical Performance

After we examined the thermodynamics and kinetics, it is of great interest to investigate the electrochemical performance of sulfur cathode. The galvanostatic discharge/charge curves of the sulfur/carbon composite are presented in Figure 4-11. The discharge curves show the characteristic three-stage pattern, but the obtainable capacity is lower than the theoretical value due to kinetic limitation. Stage I and II together contributes  $\sim 600$  mAh/g while Stage III only

contributes ~300 mAh/g due to its inferior kinetics. Unlike the coulombic titration curves in Figure 4-1, the three-state feature is also found in the charging profiles with a shorter plateau. In the second discharge, Stage II (plateau at 1.5V) becomes shorter while Stage I becomes wider. Discharge/charge in 1.4-3.0V was conducted to avoid the further reduction of  $\text{MgS}_x$  to  $\text{MgS}$  (Figure 4-11b). It shows a much higher initial coulombic efficiency of 97.6% than 83.6% in Figure 4-11a. This difference agrees well with previous thermodynamic study, which illustrates the facileness to re-oxidize  $\text{MgS}_x$  but not  $\text{MgS}$ . During cycling, both Stage II and Stage III fade gradually while Stage I is very stable providing a capacity of 300 mAh/g above 1.5V. The typical voltage profiles were replotted in Figure 4-11c-d to examine the reaction kinetics at each stage. Clearly, the discharge/charge curves show some symmetry but do not mirror each other in the simple electrolyte. The overpotential increases with Mg concentration in Stage I. Remarkably, Stage II shows negligible overpotential ( $<0.1\text{V}$ ). Stage III shows the largest overpotential. This result is consistent with our kinetics analysis above.

The cycling performance are given in Figure 4-11e-f. Coulombic efficiency gradually increases in the first initial cycles to ~100% when the Mg/S cell is discharged to 0.5V, but it is close to 100% in the first cycle if the cell is only discharged to 1.4V. These results have demonstrated that the sulfur/sulfide redox is partially reversible in Mg chemistry. Several reasons may account for the capacity loss in the simple electrolyte during cycling: 1) loss of active material due to the dissolution of S and  $\text{MgS}_x$  (despite their solubility is low); 2) difficulty to oxidize the formed  $\text{MgS}$ ; 3) volume expansion during magnesiation and the associated fracture of the composite electrode renders some active material to lose contact with carbon matrix. Despite in Mg/S cells volume of the active material only expands by 22% after fully discharge compared to that of ~80% in Li/S cells, the solid state reaction route can exaggerate the

influence of mechanical strain. To make the Mg/S chemistry practical, improving the reaction reversibility will be the focus of future work.

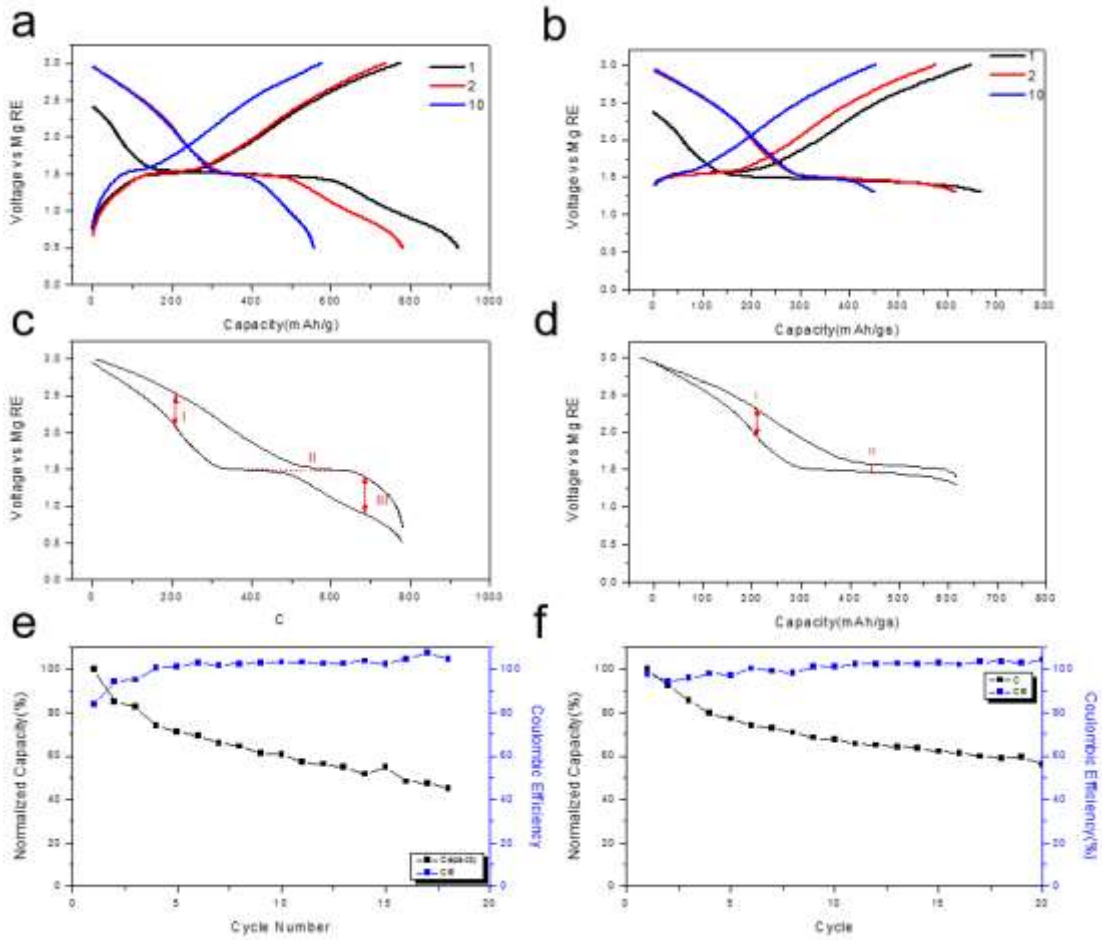


Figure 4-11. Electrochemical Performance of Sulfur cathodes. a-b) Galvanostatic discharge/charge curves at different cycles; c-d) voltage profiles for a typical cycle; e-f) Cycling performance and Coulombic efficiency, current: 100 mA/gs.

## Discussion

The discharge voltage profiles under both equilibrium (Figure 4-1) and non-equilibrium (Figure 4-11) conditions are in good agreement with Karger's work and our previous study.<sup>2425</sup> Similar to other electrolyte Li/S system, the presence of multiple stages implies the existence of intermediate polysulfide species during sulfur reduction. The nearly complete utilization under equilibrium condition justifies the high capacity potential of sulfur cathode in Mg chemistry. However, the reaction reversibility needs further improvement for practical battery application. The fast kinetics of the Stages I and II is due to the synergetic effect of liquid-solid reaction and fast Mg diffusion in the amorphous  $\text{MgS}_x$ . In contrast, a solid state reaction in which  $\text{Mg}^{2+}$  has an extremely low diffusivity leads to the sluggish kinetics in Stage III. The charge curve shows less staging pattern, implying the absence of consecutive phase transition from Mg rich  $\text{MgS}$  to  $\text{S}_8$ . We speculate that a straightforward surface oxidation of  $\text{MgS}$  and  $\text{MgS}_{x,x=2-8}$  to  $\text{S}_8$  occurs, similar to what has been observed for the oxidation of sulfide in Li chemistry.<sup>67</sup>

Overall, the reaction pathway is schematically summarized in Figure 4-12. In stage I, the dissolved sulfur and sulfur on the surface is reduced. Part of the formed polysulfide chain dissolves and the rest bonds with  $\text{Mg}^{2+}$  and exists in the solid state. In stage II, phase transition occurs between dissolved long-chain polysulfide and insoluble short-chain polysulfide. This stage is featured by fast kinetics due to the L-S reaction and fast  $\text{Mg}^{2+}$  diffusion. In stage III, phase transition occurs between insoluble short-polysulfide and  $\text{MgS}$ , which is kinetically very slow since  $\text{MgS}_2$  and  $\text{MgS}$  is insoluble and  $\text{Mg}^{2+}$  diffusion through the formed surface  $\text{MgS}$  is extremely difficult. Since across the sulfur layer there is an Mg concentration gradient, the inner sulfur may not have opportunity to participate in the reaction before the surface sulfur is fully reduced. Once surface  $\text{MgS}$  reaches a critical thickness, the reaction will be shut down by the large overpotential needed to drive  $\text{Mg}^{2+}$  tunnel through  $\text{MgS}$  layer.

Notably, the coulombic titration curve of Li/S system in LiTFSI-DEMETFSI ionic liquid electrolyte also shows three-stage pattern:<sup>68</sup> stages I and II shows fast kinetics and contributes to half of the theoretical capacity, while stage III shows sluggish kinetics and only contributes ~200 mAh/g. This is in great coincidence with what we observed here, implying the similarity in sulfur reduction pathway where the dissolution polysulfide is inhibited.<sup>68</sup>

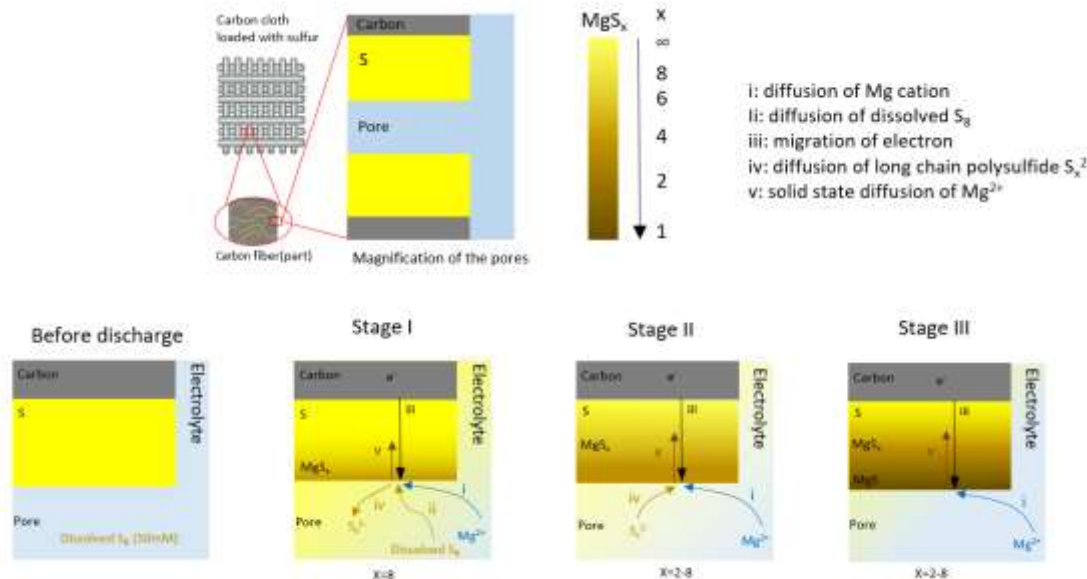


Figure 4-12. Schematic for Overall Sulfur Reduction Pathway.

### Conclusion

In this work, for the first time we investigated the thermodynamic, reaction pathway and kinetics of sulfur cathode in Mg battery chemistry. The equilibrium voltage profile, together with ESI-MS spectra and XPS results demonstrate that sulfur reduction occurs through three consecutive steps: Stage I) single phase reaction from sulfur to long-chain polysulfide (voltage slope in 2.4-1.5V), Stage II) two phase reaction from soluble long-chain polysulfide to insoluble short-chain polysulfide (voltage plateau at 1.5V) and Stage III) solid state transition from short-chain polysulfide to MgS (voltage slope in 1.5-0.5V) in the simple MgTFSI<sub>2</sub>-DME

electrolyte. The reaction in Stage II shows fast kinetics due to the synergetic effect of liquid-solid reaction and fast  $\text{Mg}^{2+}$  diffusion in the amorphous  $\text{MgS}_x$ , but the Stage III reaction is sluggish since formed  $\text{MgS}$  impedes the diffusion of  $\text{Mg}^{2+}$ . Electrochemical cycling shows that  $\text{Mg/S}$  cells can work reversibly in the simple electrolyte. Our work provides the fundamental understanding toward the reaction mechanism and kinetics of  $\text{Mg/S}$  system, and also paves the way for the performance improvement for practical usage. Future work will focus on understanding of the chemical speciation of sulfur using various characterizations and performance improvement based on the knowledge of this work



## Chapter 5 Enhancing the Reversibility of Magnesium/Sulfur Battery Chemistry through Li<sup>+</sup> Mediation

### *Introduction*

Despite of its high energy density promise, the development of rechargeable magnesium/sulfur battery is plagued by lack of proper electrolyte. The magnesium organohaloaluminate electrolyte that allows reversible Mg deposition is synthesized by in-situ reaction between Lewis acid (AlCl<sub>3</sub>) and nucleophilic Lewis base (RMgCl), which reacts with the electrophilic sulfur cathode.<sup>[126]</sup> This incompatibility has not been addressed until 2001, Kim et al. proposed a new electrolyte system using non-nucleophilic hexamethyldisilazide magnesium chloride (HMDSMgCl), and reported the first proof-of-concept Mg/S battery.<sup>[57]</sup> This electrochemical couple operates at a very low potential (0.89 V), and loses ~70% capacity at the 2<sup>nd</sup> discharge. Following Kim's initial efforts, Zhao-Karger et al. developed a novel non-nucleophilic electrolyte based on magnesium-bis(hexamethyldisilazide) [(HMDS)<sub>2</sub>Mg] using various ether solvents and ionic liquid additives, and investigated the reaction mechanism of a Mg/S cell by XPS.<sup>[82]</sup> However, despite the two discharge plateaus at 1.5 V and 0.7 V during initial sulfur reduction, no plateau was observed in the following cycles. Indeed, the capacity dropped more than 60% after the 2<sup>nd</sup> cycle. In summary, so far, no real reversible Mg/S battery has been demonstrated, primarily due to the electrochemical inactivity of the formed lower order Mg polysulfides (Mg-PS) toward oxidation.

We introduce herein a new strategy to enhance the reversibility of Mg/S chemistry in the non-nucleophilic Mg-HMDS electrolyte. LiTFSI is used as an additive to enable the conjugation of reversible polysulfide redox reaction on cathode with Mg deposition/stripping on anode.

Reversible discharging/charging of the Mg/S cell is demonstrated for over 30 cycles with specific cathode capacity comparable to the sister Li-S system. Two possible mechanisms for the enhanced reversibility are suggested: 1)  $\text{Li}^+$  participates in the cathode reaction to form readily rechargeable Li polysulfide (Li-PS) or incorporates into Mg-PS to form hybrid Mg/Li polysulfide (MgLi-PS) during discharge, or 2) The hard Lewis acid  $\text{Li}^+$  strongly coordinates to the surface  $\text{S}^{2-}$  of lower order Mg-PS, hence enhancing its solubility, decreasing its re-oxidation energy barrier and making it electrochemically active. The first role can be deduced from the facts that the cathode redox couple in a RMB can be tailored by changing the relative activity of  $\text{Mg}^{2+}$  and  $\text{Li}^+$ ,<sup>24-29</sup> and that crystalline MgS starts to lithiate in Li electrolyte when potential decreases to 1.7 V vs Li/Li<sup>+</sup> (1 V vs Mg/Mg<sup>2+</sup>).<sup>30</sup> On the other hand, the positive effect of Lewis acids on the reversibility of sulfides is well known, which provides strong supports for the second role of  $\text{Li}^+$ .<sup>31</sup> Though further studies are needed to realize a practical Mg/S system, specifically in terms of electrolyte volume and Li salt concentrations, we strongly believe that system optimization based on the new scientific insights obtained in this work will pave the path for the realization of practical rechargeable Mg/S battery

Table 5-1 Theoretical Capacity and Energy Density Comparison of different Battery Systems

Full Cell system	Cathode		Anode		Full Cell Capacity (mAh/g)	Full Cell Energy (Wh/kg)
	Theoretical Capacity (mAh/g)	Voltage (V)	Theoretical Capacity (mAh/g)	Voltage (V)		
LiCoO <sub>2</sub> /graphite	140	4	370	0.1	102	396
Li-S	1675	2.1	3828	0	1165	<b>2447</b>

Li <sub>2</sub> S/Silicon	1165	2.1	4211	0.1	913	<b>1825</b>
Li <sub>2</sub> S/graphite	1165	2.1	372	0.1	454	908
Mg/Mo <sub>6</sub> S <sub>8</sub>	128	1.2	2233	0	121	145
Mg/S	1675	1.8	2233	0	957	<b>1722</b>

### Experiment

**Electrolyte preparation:** Electrolytes was prepared under pure argon atmosphere in VAC, Inc. glove box (<1 ppm of water and oxygen). The non-nucleophilic Mg electrolyte based on (HMDS)<sub>2</sub>Mg (denoted as Mg-HMDS) was synthesized following previously reported procedure.<sup>23</sup> The electrolyte was prepared by adding lithium bis(trifluoromethanesulfonyl)imide (LiTFSI) into the non-nucleophilic (HMDS)<sub>2</sub>Mg-based electrolytes (denoted as Mg-HMDS) and stirring overnight. The LiTFSI salt was baked at 80 °C in glove box overnight before use.

**Battery fabrication:** ACC/sulfur cathode was made following previous procedure.<sup>32</sup> Typical sulfur loading is 0.5 mg/cm<sup>2</sup> in this study. The thickness of the ACC is ~0.47 mm. Mg foil was used as anode and Whatman Glass fiber as separator.

**Electrochemical Measurement:** Galvanostatic tests were carried out in Swagelok cell with Arbin Instrument. Inconel alloy rod was used as current collector, due to its electrochemical stability against the electrolyte<sup>33</sup>. Cyclic voltammetry of the electrolytes was performed in a three-electrode cell with Pt disk as working and Mg foil as both counter and reference electrodes on Gamry Reference 3000.

**Material Characterization:** The morphology of the deposition in the dual-ion electrolyte and the morphology of ACC/S cathode were examined using a Hitachi SU-70 field-emission scanning electron microscope. X-ray powder diffraction patterns were obtained on Bruker Smart 1000 (Bruker AXS Inc., USA) using  $\text{CuK}\alpha$  radiation with an air-tight holder from Bruker. Raman measurements were performed on a Horiba Jobin Yvon Labram Aramis using a 532 nm diode-pumped solid-state laser, attenuated to give 900 mW power at the sample surface. FT-IR tests were performed on a Thermo Nicolet NEXUS 670. XPS analysis was measured with a Kratos AXIS Ultra DLD instrument using monochromated Al  $\text{K}\alpha$  x-rays as the excitation source. For ICP measurements 400  $\mu\text{L}$  of TEGDME from each corrosion test were evaporated and the remaining solids were diluted in 3%  $\text{HNO}_3$  solution (4.125 mL). ICP-OES measurements were performed using a Shimadzu ICPE-9820 Dual View Spectrometer. Intensities were measured at 280.270 nm for Mg and calibration curves were made from Mg standards (Sigma Aldrich), traceable to the National Institute of Standards and Technology (NIST).

### Results and Discussion

To find the origin of the inactiveness of  $\text{MgS}_x$ , we conducted a corrosion test. It is known that Li metal will be corroded by elemental sulfur in ethereal solvent, leading to the formation of soluble Li-PS with a yellow/brown color (Figure 5-1a). However, in our experiment, the visible corrosion of Mg under similar conditions never happen even after three weeks (Figure 5-1b). Though no clear appearance of PS is obtained in the liquid, the formation of an  $\text{MgS}$  layer on the Mg foil was detected by XPS (Figure 5-2). This surface layer protects the bulk of the Mg from further corrosion by sulfur, similar to the manner where natural layer of  $\text{MgO}$  passivate

Mg from oxidation in ambient conditions. Interestingly, the addition of LiTFSI to Mg/S/TEGDME under the same condition turns TEGDME to yellow (typical for polysulfide in glymes) after only 12 hours (Figure 5-1c) and to brown after 54 hours (Figure 5-1d). This strongly suggests that the surface layer of MgS is dissolved by the action of  $\text{Li}^+$  and Mg surface could not be passivated anymore. In order to confirm whether MgS is indeed dissolved, we used ICP-OES to examine the presence of dissolved Mg in TEGDME solution after the corrosion experiment. The concentration of Mg in the TEGDME was negligible when no  $\text{Li}^+$  was present ( $<8 \mu\text{g/L}$ ), indicating negligible presence of Mg-PS in TEGDME. However the concentration of Mg increased by 3 orders of magnitude ( $>0.65 \text{ mg/L}$ ) in the presence of  $\text{Li}^+$  after 12 hours of LiTFSI addition. The corrosion of Mg continued (Figure 5-1d), increasing the concentration of Mg by another order of magnitude after 54 hours ( $>8.4 \text{ mg/L}$ ). The result is consistent with our XPS observation on Mg foil in electrolyte with and without LiTFSI (Figure 5-3), and double confirms our hypothesis that the mediation role of  $\text{Li}^+$  on the rechargeability of low order Mg-PS is originating from its effect on Mg-PS solubility: either hard Lewis acid ( $\text{Li}^+$ ) strongly coordinates with the hard base surface  $\text{S}^{2-}$  in the formed low order Mg-PS and assists its dissolution, or  $\text{Li}^+$  is driving the solubility of surface MgS through ion exchange reaction (MgS to  $\text{Li}_2\text{S}$ ). It is also possible that MgS is first lithiated by  $\text{Li}^+$  due to the natural negative potential of the Mg metal and then the formed MgLi-PS enables further reaction with the dissolved elemental sulfur to form soluble higher order MgLi-PS.

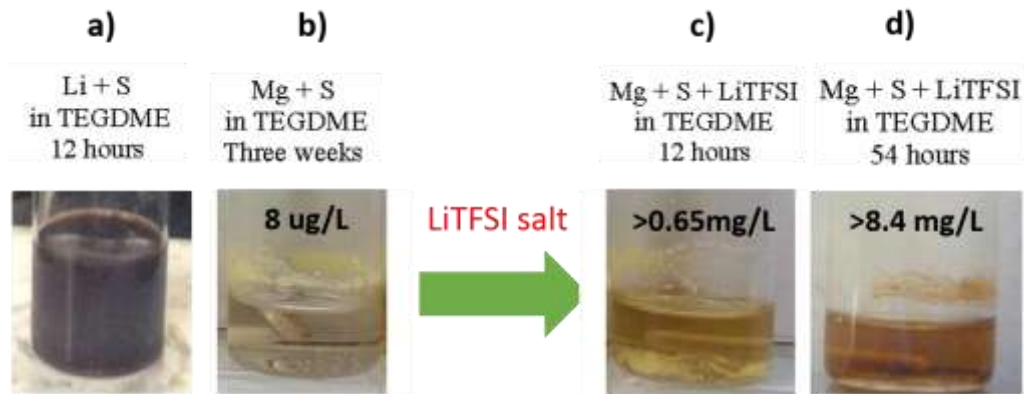


Figure 5-1. Corrosion Test of Mg foil in TEGDME solution

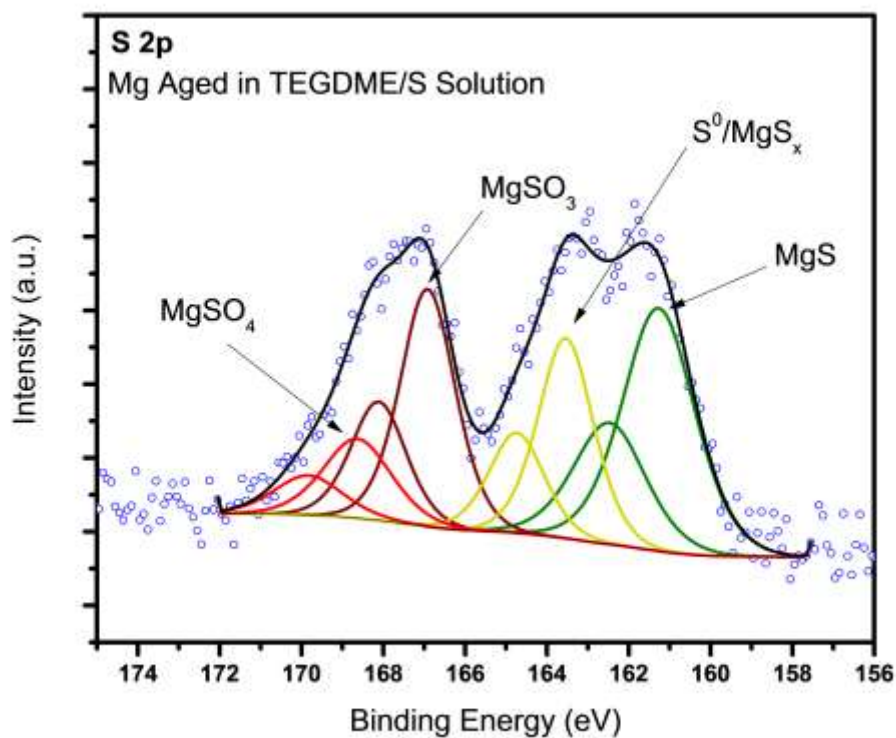


Figure 5-2. XPS of Mg foil aged in TEGDME/sulfur, clearly demonstrating MgS layer on the Mg surface.

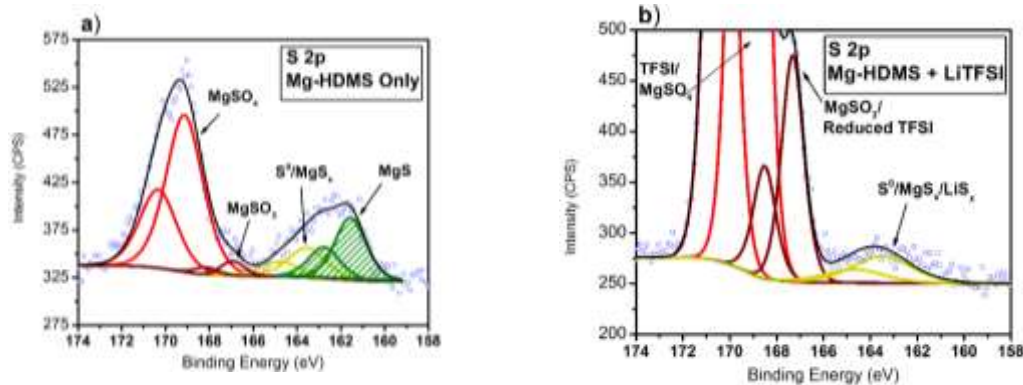


Figure 5-3. Comparison of surface XPS measurements of Mg anode cycled in Mg-HDMS in the absence (a) and presence (b) of LiTFSI

We next fabricated full cells with Mg anodes and sulfur cathodes in the electrolytes. The active carbon cloth/sulfur (ACC/S) cathode was closed in a custom-built three-electrode cell with Mg foil as both counter and reference electrodes. Typical charge-discharge voltage profiles measured during galvanostatic cycling in 0.1 M Mg-HMDS + 1.0 M LiTFSI electrolyte are presented in Figure 5-4a. The capacity increases in initial cycles, a typical behavior of ACC/S cathodes in Li/S cells due to slow penetration of electrolyte into the pores inside carbon. During this infiltration process, sulfur utilization gradually increases with cycling, and reaches its maximum at the 8<sup>th</sup> cycle. Continued cycling yields a stable capacity of roughly 1000 mAh/g<sub>s</sub>. The 8<sup>th</sup> discharge voltage profile (Figure 5-4a) contains two plateaus, the first of which (~550 mAh/g<sub>s</sub>) is observed at ~1.75 V, followed by a slope leading to the 2<sup>nd</sup> plateau at ~1.2 V (~300 mAh/g<sub>s</sub>). The two reduction plateaus are in good agreement with those reported in Zhao-Karger's work, indicating the formation of high-order and low-order polysulfides, respectively. However, since Li-PS redox reaction takes place at similar potentials, it is likely that Li-PS also forms simultaneously. MgLi-PS may also form due to Li<sup>+</sup> incorporating into

Mg-PS at this potential domain. However, despite  $\text{Li}^+$  may involve in sulfur reduction, the discharge path way is more likely dominated by Mg-PS instead of Li-PS, since Li-PS reduction as reported in literature shows a short plateau of  $\sim 250 \text{ mAh/g}_s$  followed by a long plateau of  $\sim 700 \text{ mAh/g}_s$  for ACC/sulfur cathode,<sup>[80]</sup> which is distinctly different from the voltage profile presented in Figure 5-4a, in which the 1<sup>st</sup> plateau is longer ( $\sim 550 \text{ mAh/g}_s$  vs typical  $250 \text{ mAh/g}_s$  for Li/S systems) and the 2<sup>nd</sup> plateau at the lower voltage is shorter ( $\sim 300 \text{ mAh/g}_s$  vs  $700 \text{ mAh/g}_s$ ). Two plateaus are observed in the recharge process as well, the first of which at  $\sim 1.8 \text{ V}$  corresponds to the oxidation of low order PS. This plateau is seldom seen in previous Mg/S cell, thus its appearance suggests enhanced electrochemical activity of short chain PS in the presence of  $\text{Li}^+$ . The 2<sup>nd</sup> plateau at  $\sim 2.7 \text{ V}$  arises from oxidation of the high order PS.

Potential rise usually seen at the end of recharge plateau in Li/S cells was not observed even at high rate (1C) in this work, possibly due to electrolyte decomposition or shuttle phenomena. For this reason the recharge process presented in Figure 5-4a was conducted at a high rate (1C), and was immediately cut off when theoretical capacity is reached in order to minimize possible side reactions. Negligible overpotential was required for Mg dissolution and an initial overpotential of  $-0.55 \text{ V}$  was needed to drive Mg deposition on Mg foil, but it drops gradually to  $-0.1 \text{ V}$  during cycling (Figure 5-5). Since thermodynamically polysulfide should be reduced on the metallic Mg anode, shuttle effect should also exist in our system, as supported by XPS of the anode.

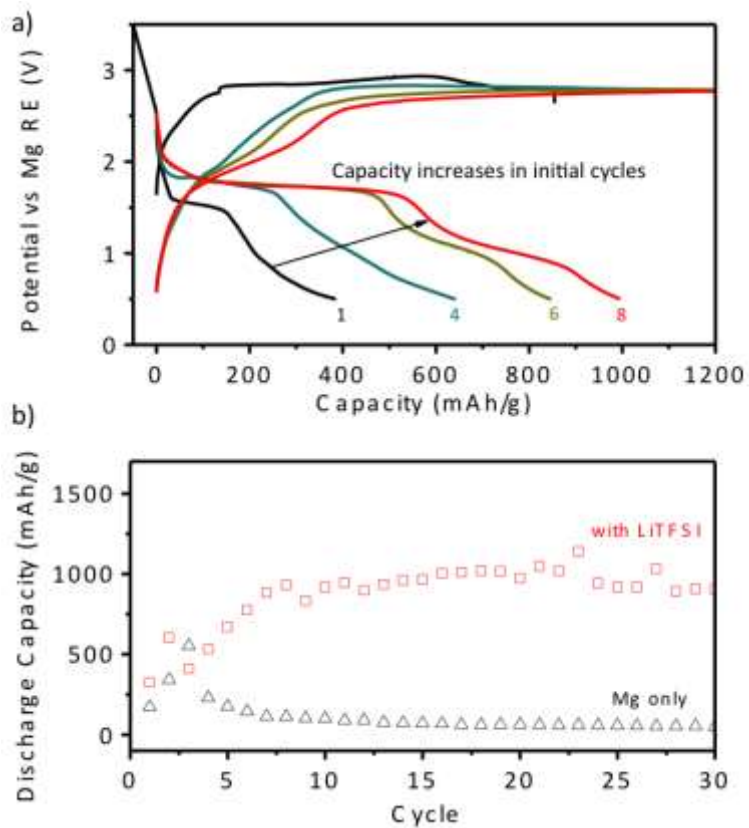


Figure 5-4. a) Charge/discharge curves of sulfur cathode in 0.1 M Mg-HMDS+1.0 M LiTFSI electrolyte in a three electrode cell at a current of 71 mAh/g at room temperature. Arrow illustrates the capacity increasing trend of the ACC/S composite cathode as a result of slow electrolyte penetration. b) Cycling stability of the Mg/S battery in electrolyte with and without LiTFSI.

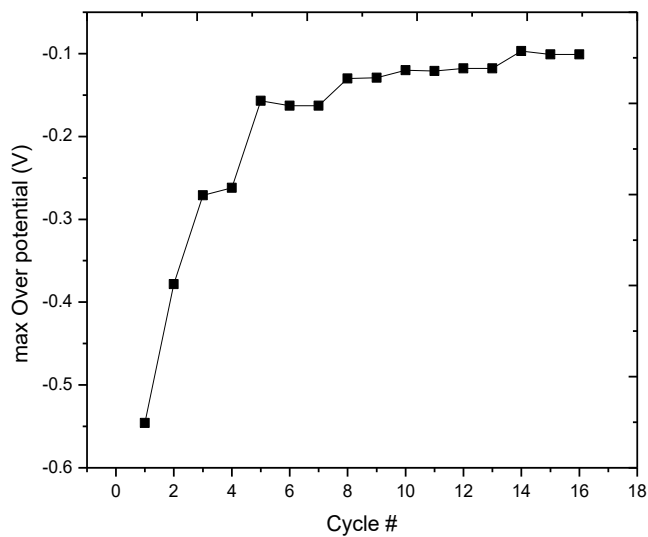
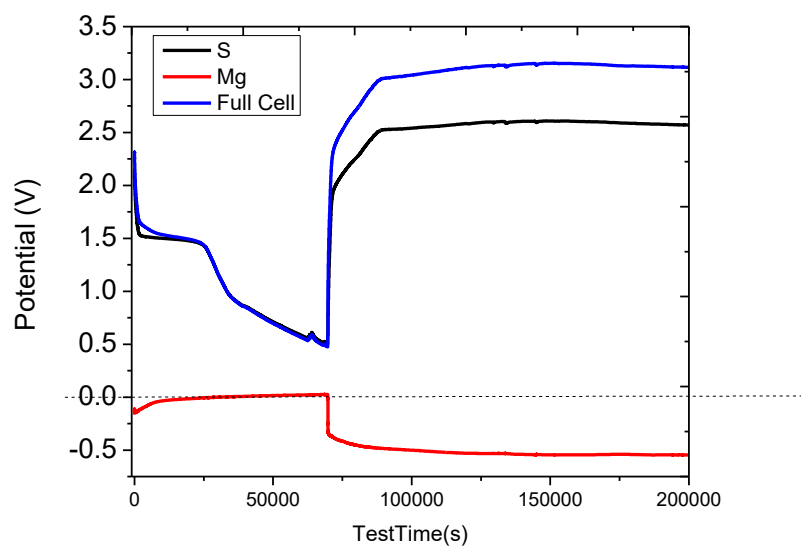


Figure 5-5. a) First cycle potential of sulfur cathode, Mg anode vs. Mg RE and full cell potential in 0.2 M Mg-HMDS + 0.5 M LiTFSI electrolyte and b) Overpotential for Mg deposition during cycling

Previous work on Mg/S system claim that sulfur reduction reaction takes place in two steps in ether solvents: a fast solid-liquid two phase reduction forming high order polysulfide ( $\text{MgS}_8$ ,  $\text{MgS}_6$ ,  $\text{MgS}_4$ ), followed by a sluggish liquid-solid reduction forming insoluble  $\text{MgS}_2$  and  $\text{MgS}$ . The low order Mg-PS produced during the first discharge in Mg/S cell loses its electrochemical activity in the subsequent recharge due to high kinetic barriers originating from its insulating nature and insolubility. However, as demonstrated in the corrosion experiment, the solubility of short chain Mg-PS increases dramatically due to assistance of  $\text{Li}^+$ , potentially lowering the kinetic barrier for re-oxidation of Mg-PS. We therefore suggest that the reduction of sulfur in our battery occurs via the following sequences:

- 1) Sulfur reduction starts by the formation of soluble long chain  $\text{MgLi-PS}$ . Since the first discharge plateau provides about one third of sulfur's theoretical capacity (558mAh/g), the formed product should have the stoichiometry of  $\text{MS}_3$ ,  $\text{M}=\text{Mg}_x\text{Li}_y$ .
- 2) Further reduction will lead to either reversible short chain Li-PS ( $\text{Li}_2\text{S}$  and  $\text{Li}_2\text{S}_2$ ), or short chain Mg-PS ( $\text{MgS}$  and  $\text{MgS}_2$ ).

The oxidation of discharged product during recharge occurs via following steps:

- 1) During charge, the short chain Li-PS ( $\text{Li}_2\text{S}$  and  $\text{Li}_2\text{S}_2$ ) will oxidize to form longer chain PS ( $\text{Li}_2\text{S}_8$ ).
- 2) The presence of  $\text{Li}^+$  enables reactivation of the short chain Mg-PS ( $\text{MgS}$  and  $\text{MgS}_2$ ) either through an ion exchange reaction and transforms them into rechargeable  $\text{Li}_2\text{S}$  and  $\text{Li}_2\text{S}_2$ , or through strong coordination of  $\text{Li}^+$  with the surface  $\text{S}^{2-}$  and  $\text{S}_2^{2-}$  of  $\text{MgS}$  and  $\text{MgS}_2$  that increase their solubility and reduce the re-oxidation kinetic barrier by forming  $\text{MgLi-PS}$ . A schematic illustration of the proposed mechanism, and the correlated voltage profile, is presented in Figure 5-6.

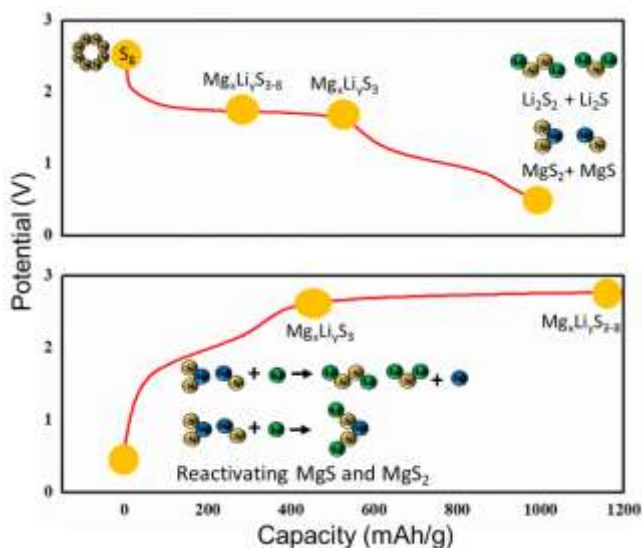


Figure 5-6. Working mechanism of the Mg/S battery with LiTFSI additive

### Conclusion

We demonstrated a rechargeable Mg/S battery with much improved reversibility by using LiTFSI as additive. We show that our system combines the dendrite free deposition/stripping of Mg anode with reversible redox reaction of sulfur cathode through activation of inactive MgS and MgS<sub>2</sub> by Li<sup>+</sup>. The cell demonstrated a capacity of 1000 mAh/g<sub>s</sub> with two discharge plateaus at 1.75 V and 1.0 V, corresponding to an obtainable energy density of 874 Wh/kg. It showed stable capacity up to 30 cycles. The assisting effect of Li<sup>+</sup> on Mg/S solubility in TEGDME, a key parameter controlling the reversibility of sulfur cathodes, is revealed by XPS on cycled Mg anode and confirmed by corrosion experiments. It is, to our knowledge, the first realization of a convincingly reversible Mg/S battery chemistry. Although the amount of electrolyte required is dictated by the required Li<sup>+</sup>, necessitating an excess electrolyte volume, this work undoubtedly opens a new avenue that could lead to a fully rechargeable Mg/S system with further optimization, while shedding light on the mechanism of how Li<sup>+</sup> mediates the electrochemical reactions.



## Chapter 6 Rechargeable Aluminum/Sulfur Battery based on ionic liquid electrolyte

### Introduction

Rechargeable Aluminium Batteries (RAB) based on Al metal anode attracts lots of attentions recently as one promising beyond-lithium-ion-battery system because Al provides a very high capacity (2.98 Ah/g and 8.05 Ah/cc) and it is the most abundant metal element in earth crust. Although reversible Al deposition/stripping in non-aqueous electrolyte at room temperature is challenging due to Al's tendency to form surface passivation layer,<sup>[127]</sup> it was shown possible in ionic liquid based electrolyte with up to 100% Coulombic efficiency.<sup>[62]</sup> Generally, previous reports of RABs using ionic liquid electrolyte can be summarized into two categories according to their distinctive cathode reaction. The first category operates by anion ( $\text{Cl}^-$ ,  $\text{Al}_x\text{Cl}_y^-$ , etc.) insertion into graphite or other carbonaceous material.<sup>[128][129][130][131]</sup> This dual-ion operation mechanism inevitably induces electrolyte concentration decline during battery charging. Consequently, the attainable energy density of the battery is compromised by the amount of salt in the electrolyte. The other category is a rocking chair system which operates by  $\text{Al}^{3+}$  intercalation at cathode. This type is more preferred since the overall electrolyte concentration maintains constant during battery operation. Nevertheless, previous investigations show inferior performance.<sup>[132][133]</sup> In order to realize the promising metrics of RAB, there is a dire need for developing high voltage/capacity cathodes.

As a high capacity cathode material (1,675 mAh/g), sulfur has attracted intense interest in Li/S,<sup>[10][80]</sup> Mg/S<sup>[82][134]</sup> and Na/S<sup>[135][136]</sup> systems. A rechargeable Al/S battery is also of great

interest because of its high cell capacity (1072 mAh/g-total electrode mass), reasonable voltage (1.25 V) (see Calculation Section) and low cost. Overall, the gravimetric energy density is 1340 Wh/kg, over three times of a commercial LiCoO<sub>2</sub>/graphite cell and close to that of a Li<sub>2</sub>S/silicon cell.<sup>[134]</sup> The high energy density and low cost make Al/S system a very promising battery chemistry for electric vehicles and grid energy storage. Motivated by the potential, Cohn et al. recently demonstrated a primary Al/S battery with capacity close to the theoretical value.<sup>[68]</sup> Up to now, there was no demonstration of reversible Al/S battery due to the inability to oxidize AlS<sub>x</sub>.

Herein, we demonstrate the first reversible Al/S battery in ionic liquid electrolyte by enhancing the oxidation kinetics of AlS<sub>x</sub> via encapsulating sulfur into microporous active carbon (pore size < 2 nm). Electrochemical, spectroscopic and microscopic observations indicates that sulfur undergoes a solid state conversion reaction. Kinetics analysis infer that the system is limited by this slow solid state sulfur conversion reaction. Raising temperature was proved an effective approach to mitigate the kinetic limitation thus decrease the voltage hysteresis.

### **Experiment**

**Cathode Fabrication:** Activated carbon cloth (ACC)/sulfur cathode was prepared through a melt-diffusion method following previous reports. The ACC samples (ACC-507-20) were obtained from Kynol Inc. (USA) and were cut to circular discs with a diameter of ~ 8 mm. Elemental sulfur (99.98%, Sigma-Aldrich) was spread on the bottom of a stainless reactor and then ACC disks were laid on top of the sulfur powder. The reactor was then sealed and heated to 155 °C for 12 hours. Sulfur loading was measured by subtracting the mass of blank ACC from the loaded ACC. Typical sulfur loading is 0.8-1.0 mg/cm<sup>2</sup> in this study.

**Electrolyte Preparation:** Electrolytes were prepared under pure argon atmosphere in VAC, Inc. glove box (<1 ppm of water and oxygen). The electrolyte was made by adding anhydrous aluminium chloride ( $\text{AlCl}_3$ , 99.99%, Sigma Aldrich) into 1-ethyl-3-methyl-imidazolium chloride (EMICl, 97%, Acros Organics) slowly under rigorous stirring. EMICl was dried in glove box at 150 °C overnight before use.

**Electrochemistry:** Al foil was used as anode. Separators are Whatman Glass fiber or W-scope COD 16. Inconel alloy rod was used as current collector. 100  $\mu\text{L}$  electrolyte was added for each cell. Galvanostatic charge/discharge tests were carried out in Swagelok cell with Arbin Instrument.

**Solubility Measurement:** Sufficient sulfur,  $\text{Al}_2\text{S}_3$  and mixture of sulfur/ $\text{Al}_2\text{S}_3$ (atomic ratio S: $\text{Al}_2\text{S}_3$ =15:1) were added into three separate glass vials containing ionic liquid electrolyte. After >1 week rest, 100  $\mu\text{l}$  of the upper transparent solution were taken out from the glass vials and diluted to 20 mL with 2%  $\text{HNO}_3$  for ICP-OES measurement. The mixture of sulfur/ $\text{Al}_2\text{S}_3$  in the atomic ratio of S: $\text{Al}_2\text{S}_3$ =15:1 was termed as Al polysulfide( $\text{Al}_{2/3}\text{S}_6$ ). The sulfur loss of the ACC/S cathode into electrolyte was quantified by measuring sulfur content of the cycled separator with ICP-OES. ICP-OES measurements were performed using a Shimadzu ICPE-9820 Dual View Spectrometer. Intensities were measured at 280.270 nm for Al and calibration curves were made from Al standards (Sigma Aldrich), traceable to the National Institute of Standards and Technology (NIST).

**Material Characterization:** X-ray diffraction patterns (XRD) were obtained on Bruker Smart 1000 (Bruker AXS Inc., USA) using  $\text{CuK}\alpha$  radiation. Since the highly dispersed sulfur in the ACC/sulfur composite show no XRD peaks, we use a simple carbon/sulfur electrode to investigate the crystalline change of sulfur after discharge. A mixture of sulfur powder:carbon black:PTFE=5:4:1 was hand-milled and then calendared into thin-film as the electrode. The

discharged sample was sealed by a plastic tape from exposure to air and moisture. SEM was conducted using a Hitachi SU-70 fieldemission scanning electron microscope. XPS was collected with a Kratos Axis 165 spectrometer operating in hybrid mode, using monochomatized Al K $\alpha$  X-rays (1486.7 eV). Survey and high resolution spectra were collected with pass energies of 160 eV and 40 eV respectively. Peak fitting was done using CASA XPS software. Data was fit with a Shirley background using peaks with a 30 % Lorentzian, 70 % Gaussian product function. Peaks fit to the C 1s were constrained to have the same full width at half maximum (FWHM). S 2p spectra were fit with spin-orbit split 2p 3/2 and 2p 1/2 doublets, constrained by 1.18 eV separation consistent with spin- orbit splitting and a characteristic 2:1 area ratio. All peaks were constrained to have the same FWHM. Nitrogen (N<sub>2</sub>) adsorption and desorption isotherms were measured with a Micromeritics ASAP 2020 Porosimeter Test Station. Samples were degassed at 100 °C under vacuum for 12 hours before the test. The specific surface areas and micropore volume were calculated from the nitrogen adsorption branch using the BET and t-Plot method, respectively.

### Calculation

The theoretical energy density of a rechargeable Aluminum/sulfur battery can be estimated from the formation energy of aluminium sulfide. Assuming complex sulfur reduction during battery discharge, the reaction equation of an aluminium/sulfur battery and its Gibbs reaction energy (equal to the Gibbs formation energy of aluminium sulfide) are



Complete sulfur reduction is accompanied by 6 e<sup>-</sup> transfer per Al<sub>2</sub>S<sub>3</sub>. Theoretical capacity of Al/S battery based on total mass of cathode and anode can thus be calculated

$$C = \frac{nF}{M} = \frac{6 \times 26800 \text{ mAh/mol}}{2 \times 27 \frac{\text{g}}{\text{mol}} + 3 \times 32 \frac{\text{g}}{\text{mol}}} = 1072 \text{ mAh/g}$$

The electromotive force (e.m.f) of an Al/S battery can also be calculated

$$V = -\frac{\Delta G_f}{nF} = \frac{724 \frac{\text{kJ}}{\text{mol}}}{6 \times 96485 \frac{\text{C}}{\text{mol}}} = 1.25 \text{ V}$$

The theoretical energy density of an Al/S battery based on the total electrode mass is

$$E = C \times V = 1340 \text{ Wh/kg}$$

Or from the Gibbs formation energy of  $\text{Al}_2\text{S}_3$

$$E = -\frac{\Delta G_f}{M} = \frac{724 \frac{\text{kJ}}{\text{mol}}}{150 \frac{\text{g}}{\text{mol}}} = 1340 \text{ Wh/kg}$$

## **Results and Discussion**

### **Electrolyte**

The room temperature ionic electrolyte was made by mixing  $\text{AlCl}_3$  with 1-ethyl-3-methylimidazolium chloride (EMIC) in an atomic ratio of 1.3:1. Al deposition/stripping and the anodic stability of the electrolyte on glassy carbon are given in Figure 6-1. The deposition of Al occurs through the reduction of  $\text{Al}_2\text{Cl}_7^-$  to  $\text{Al}$ ,<sup>[62]</sup> which starts at a low over-potential and proceeds at very fast kinetics ( $-30 \text{ mA/cm}^2$  at  $-0.5 \text{ V}$  vs Al RE). Charge balance curve (the inset of Figure 6-1) shows the deposition/stripping process is highly reversible with a Coulombic efficiency close to 100%.

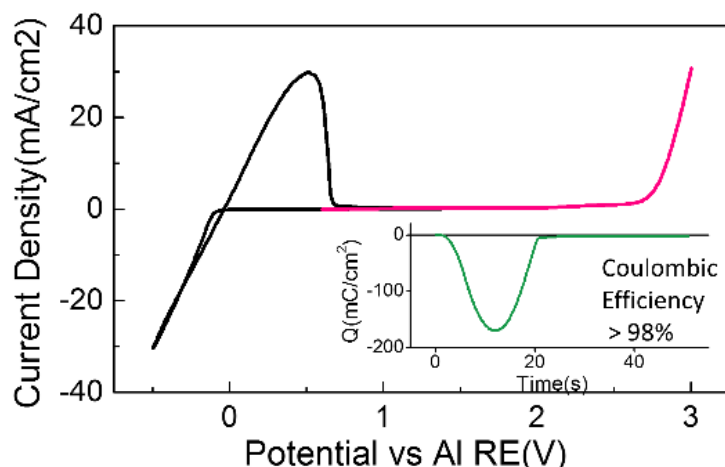


Figure 6-1. Al deposition/stripping in EMIC:AlCl<sub>3</sub>=1:1.3 electrolyte(black) and the electrochemical stability of the electrolyte (pink). Inset: Charge-time curve of Al deposition/stripping. Scan rate:100 mV/s, WE: Glassy carbon; CE and RE: Al wire.

The electrolyte is thermodynamically stable up to ~2.7 V on inert current collector (glassy carbon) (Figure 6-1), where anodic decomposition occurs ( $4\text{AlCl}_4^- \rightarrow 2\text{Al}_2\text{Cl}_7^- + \text{Cl}_2 \uparrow + 2e^-$ ).<sup>[62]</sup> Figure 6-2 gives the cyclic voltammetry results on non-inert current collector (Inconel alloy). At low voltage ( $V < 0.6$  V), there is a very small cathodic current pike ( $< 40 \mu\text{A}/\text{cm}^2$ , and fades rapidly with cycle), corresponding to underpotential deposition(UPD) of Aluminum.<sup>[62]</sup> At intermediate voltage (0.6-2.5 V), a clear anodic peak appears at ~1.35 V, which is a result of the corrosion of Inconel alloy by the electrolyte. Nevertheless, the anodic peak becomes weaker and weaker with cycling, and almost disappears at the 4<sup>th</sup> cycle. This is probably because the corrosion of Inconel alloy leads to the formation of passivation layer on its surface, which prohibits further corrosion reaction. We also referred to the XPS survey spectra of cycled ACC/S cathode and Al anode (Figure 6-3). No appearance of nickel or chromium was detected, strongly suggesting that the corrosion of the Inconel resulted in passivation layer formation, rather than dissolution of the current collector. Therefore, the

Inconel alloy is not thermodynamically but kinetically stable at this potential. At large voltage ( $> 2.5$  V), another anodic peak emerges and its intensity climbs up rapidly. This peak is similar to the one observed on inert electrode Glassy Carbon (Figure 6-1a), and they can both be attributed to the anodic decomposition of the electrolyte to chlorine gas.<sup>[62]</sup> The image of the Inconel alloy current collector before and after cycling in the Al/S battery are given in Figure 6-4. After cycling the surface in close contact with the ionic liquid electrolyte experienced a clear color change, from a shiny silver color (left) to a dark grey color (right). Note not all the surface of the Inconel alloy suffered the color transition because our ACC disk has a smaller diameter than the Inconel alloy (Inconel Alloy: 9.52 mm, ACC: 8 mm). This observation provides visual evidence on the passivation of Inconel alloy upon exposure to the ionic liquid electrolyte for repeated cycles. The absence of Ni or Cr presence on the XPS survey spectra suggests the corrosion of current collector is not affecting the cathode chemistry, and that the measured electrochemical response is indeed from reversible sulfur redox reaction.

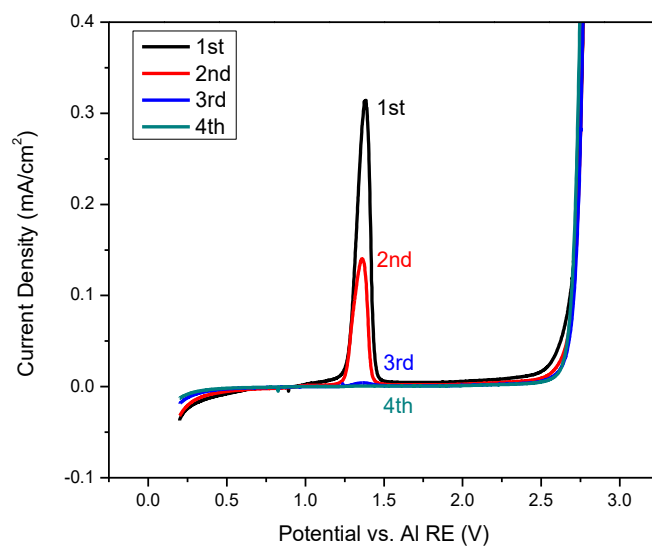


Figure 6-2. Cyclic Voltammetry of Inconel alloy in a three-electrode set-up. WE: Inconel foil; CE: Al wire; RE: Al wire; Electrolyte: EMIC:AlCl<sub>3</sub>=1:1.3. Scan rate: 10 mV/s.

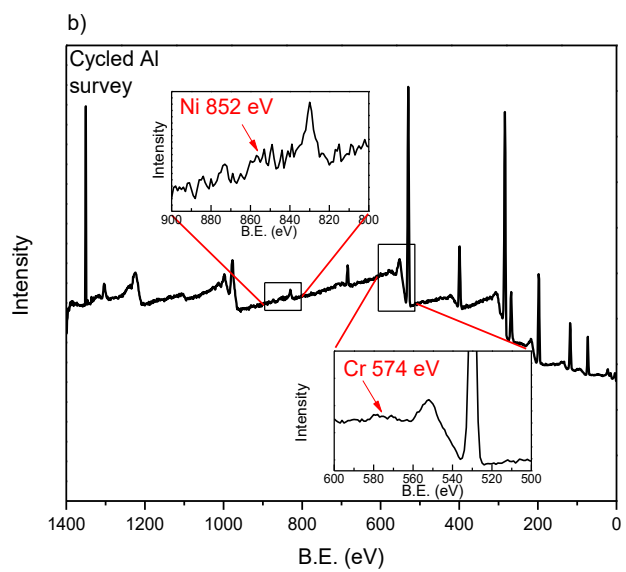
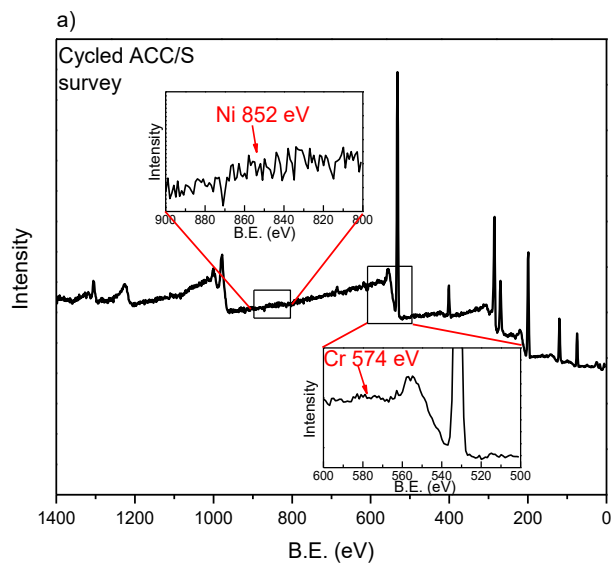


Figure 6-3. XPS survey spectra of a) cycled ACC/S cathode and b) cycled Al anode

Before cycle

After cycle



Figure 6-4. Images of Inconel alloy before and after cycle.

### **Electrochemical Performance**

The active carbon cloth (ACC)/sulfur composite was fabricated following previous reports.<sup>[80][137]</sup> N<sub>2</sub> adsorption/desorption isotherm show type I behavior (Figure 6-5), indicating the microporous structure of ACC. The Brunnauer-Emmett-Teller (BET) specific surface area decreases significantly from 2376.6 m<sup>2</sup>/g to 1532.8 m<sup>2</sup>/g and the micropore volume decreases from 0.93 cm<sup>3</sup>/g to 0.61 cm<sup>3</sup>/g after sulfur impregnation. A typical charge/discharge curve of the ACC/S cathode in Li/S battery is given in Figure 6-6.

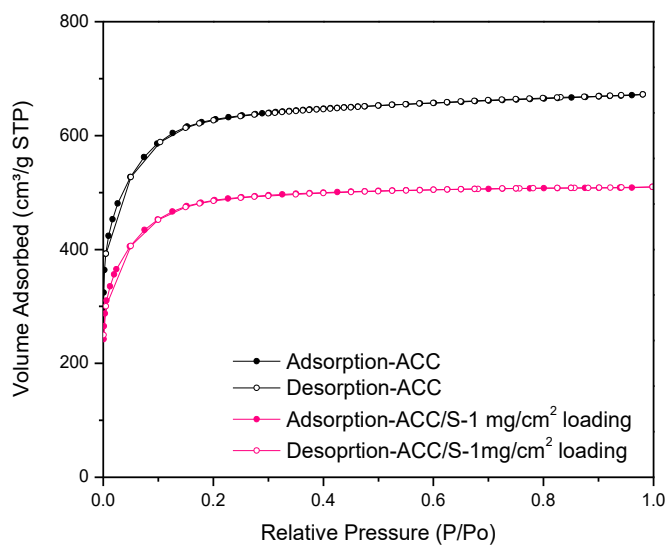


Figure 6-5. N<sub>2</sub> adsorption/desorption isotherms measured at 77 K

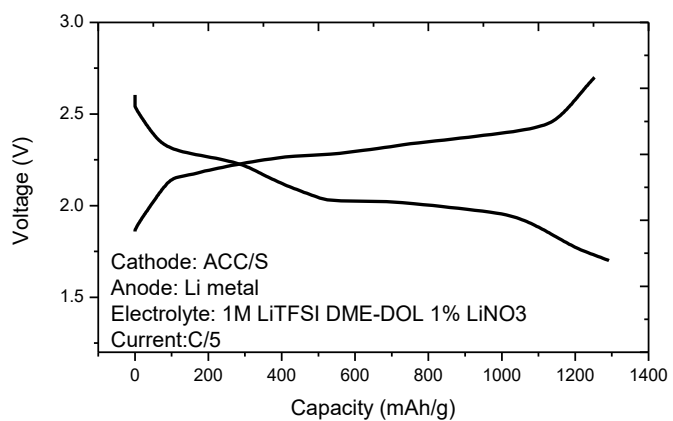


Figure 6-6. The typical charge/discharge curve of the ACC/S cathode in Li/S battery.

The Al/S battery was made by coupling ACC/S cathode with Al foil anode in Swagelok cell.

The typical charge/discharge profile of the Al/S cell at 50 mA/g<sub>s</sub> shows a single discharge

( $\sim 0.65$  V) and charge plateau (1.40 V) (Figure 6-7). This behavior is quite distinctive from the typical two-stage voltage profile in Li/S system<sup>[80][110]</sup> (Figure 6-6) or Mg/S system<sup>[82][134]</sup> using ether-based electrolyte, but resembles Li/S system based on some ionic liquid electrolyte,<sup>[138][119]</sup> and solid state Li/S battery<sup>[139]</sup>, implying similar reaction mechanism: a solid state conversion reaction of sulfur to aluminum sulfide. To confirm this hypothesis we first measured the solubility of different sulfur species in the ionic liquid electrolyte. As presented in Figure 8, sulfur, ‘aluminum polysulfide’ ( $\text{Al}_{2/3}\text{S}_6$ ) and aluminum sulfide ( $\text{Al}_2\text{S}_3$ ) have similar low solubility (very slightly soluble). Their solubility is comparable to that of sulfur in tetraglyme, but is two orders of magnitude lower than Li polysulfide ( $\text{Li}_2\text{S}_6$ ) (see more explanation of the terms in experiment part).<sup>[118][140]</sup> Moreover, ICP-OES shows low sulfur loss into the electrolyte after cycling ( $5.9 \pm 1.1$  wt% of all loaded sulfur compared to 25 wt% in ether-based Li/S cells<sup>[10]</sup>). These results support the notion that sulfur undergoes a solid state conversion reaction. A maximum capacity of  $\sim 1320$  mAh/g<sub>s</sub> can be obtained at 50 mA/g<sub>s</sub>, corresponding to a sulfur utilization of 58% after excluding the contribution of active carbon. Remarkably, cycling stability demonstrates 1000 mAh/g<sub>s</sub> for over 20 cycles (Figure 6-9), illustrating the substantially improved reversibility for sulfur reduction/oxidation reaction in our system. High loading electrodes ( $> 1$  mg/cm<sup>2</sup>) suffers lower sulfur utilization, but they also show reversible behavior.<sup>[68]</sup> This enhanced reversibility could be explained by the confinement of the reduced  $\text{AlS}_x$  species in the micropores ( $< 2$  nm), which effectively facilitate sulfide oxidation kinetics upon charging due to its ready electron access, large reaction area and shortened solid state  $\text{Al}^{3+}$  diffusion length. Additionally, the low sulfur loss also benefits the high stability of this system.

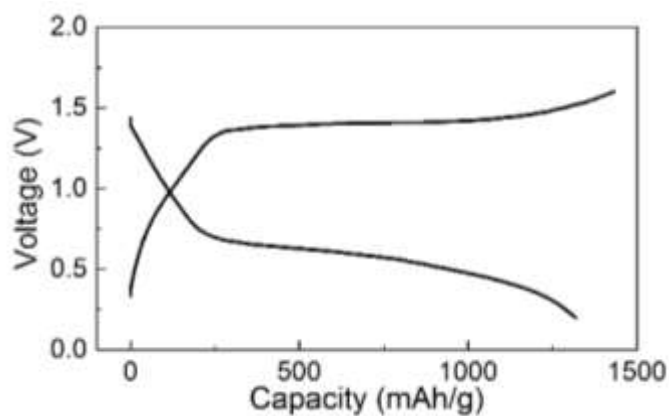


Figure 6-7. A typical charge /discharge curve of the Al/S battery with ACC/S cathode, ionic liquid electrolyte and Al foil anode. Current: 50 mA/gs. Room Temperature.

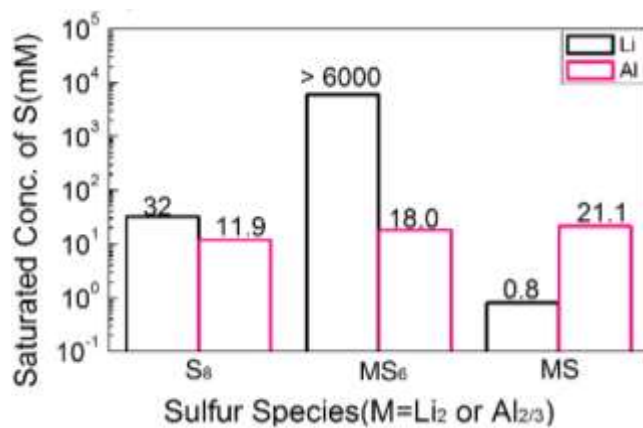


Figure 6-8. Solubility of different sulfur species (in units of sulfur atomic concentration) in Li and Al electrolytes. Li electrolyte is 1M LiTFSI in TEGDME. The solubility of lithium polysulfide is from reference 20 and 21

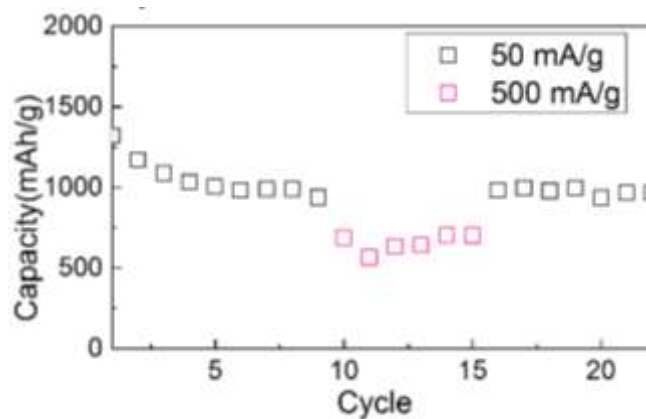


Figure 6-9. Cycling stability of the Al/S cell.

### Reaction Mechanism

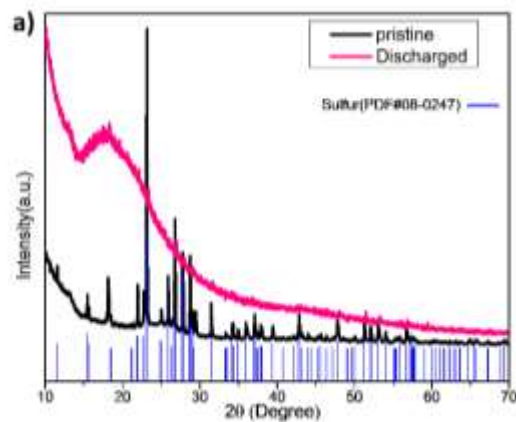


Figure 6-10. XRD of sulfur cathode before and after discharge. The bump at 15° comes from the sealing tape.

Spectroscopic and microscopic measurement were performed to understand the reaction mechanism. X-ray diffraction (XRD) was first conducted to examine the phase change of sulfur in the Al/S battery (Figure 6-10, for material characterization see experiment section). After

discharge all sulfur peaks disappeared due to its electrochemical reduction but no new peaks emerges. X-ray photoelectron spectroscopy (XPS) was conducted to examine the oxidation state change of sulfur species. The S 2p and Al 2p spectrum of  $\text{Al}_2\text{S}_3$  powder (98%, Sigma-Aldrich) was first measured as reference for analyzing sulfur oxidation states of discharged sample(Figure 6-11). The strong peak lying at 161.8 eV corresponds to  $\text{Al}_2\text{S}_3$ . Note this value is higher than those of  $\text{Li}_2\text{S}$  (160.7 eV)<sup>[123]</sup>,  $\text{Na}_2\text{S}$  (160.0 eV)<sup>[123]</sup> and  $\text{MgS}$  (160.9 eV)<sup>[57]</sup> but close to  $\text{ZnS}$  (161.5 eV)<sup>[141]</sup>, which can be explained by Al's stronger electronegativity than alkali and alkali earth elements (Electronegativity in Pauling scale: Al=1.61, Zn=1.65, Mg=1.31, Li=0.98, Na=0.93). The broad peak at 168.6 eV is attributed to some oxidized form of sulfur (sulfate) on the surface of  $\text{Al}_2\text{S}_3$ . The Al 2p spectrum shows one peak at 74.3 eV corresponding to  $\text{Al}_2\text{S}_3$ .

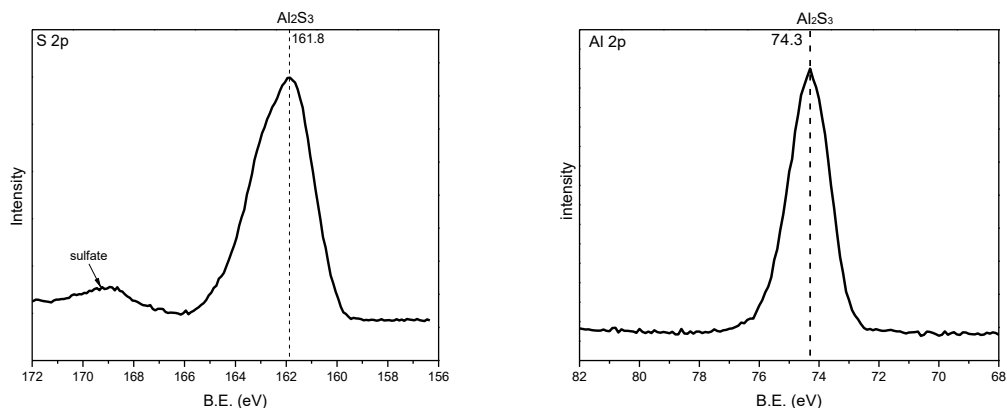


Figure 6-11. High Resolution S 2p and Al 2p spectra of  $\text{Al}_2\text{S}_3$

In order to remove the residual electrolyte on electrode surface and obtain a meaningful XPS data, we adopted similar sample treatment as in previous study<sup>[123]</sup>: we sputtered the sample with Ar beam for different durations. XPS survey and high resolution C, S, Al, O spectra were

collected for pristine ACC/S and for fully discharged ACC/S with no sputtering, 1 hour sputtering and 4 hours sputtering. To examine the effect of Ar sputtering for removing surface layer on discharged sample, the atomic ratio of each element were quantified and listed in Table 6-1.

Table 6-1. Atomic ratio (%) of each element on the surface of discharged ACC/S quantified from XPS

Element	C	O	N	S	Al	Cl	S/C
Discharged No sputtering	39.4	34.5	5.2	0.04	9.5	11.3	0.0010
Discharged 1 hour sputtering	42.9	25.3	2.1	1.6	20.6	7.5	0.037
Discharged 4 hours sputtering	63.9	13.0	3.3	3.8	10.2	5.9	0.059
Pristine	86.49	6.18	-	7.33	-	-	0.085

On the fresh surface of the discharged sample, the amount of N (5.2%) and Cl (11.3%) are significant and the sulfur content is extremely low (0.04%) compared to pristine ACC/S cathode (7.33 %). These results suggest that the surface is covered by the residual ionic liquid electrolyte and sulfur species have very low solubility in the electrolyte. After sputtering, the sulfur content increases remarkably to 1.6% (1 hour) and further to 3.8% (4 hours), and the N, Cl content decline are noticeable. Meanwhile, the S/C ratio of fresh discharged sample is 0.001, which climbs remarkably after 1 hours sputtering (S/C=0.037) and get even closer to pristine sample(S/C=0.085) after 4 hours sputtering(S/C=0.059). These results show that Ar sputtering can effectively remove the residual ionic liquid that covers on the electrode surface.

With the appreciably enhanced signal of sulfur species from the discharged sample after Ar sputtering, we were able to perform a meaningful analysis regarding its chemical oxidation states. The high resolution C 1s and S 2p spectrum are presented in Figure 6-12. Because the C 1s spectrum of the pristine sample exhibits a broad, asymmetric tail towards higher binding energy (Figure 6-12a), which is the typical feature of  $sp^2$  carbon, we use 284.0 eV as the reference to calibrate the XPS data. In contrast, the discharged no sputtering sample were referenced to 284.8 eV due to the expected adventitious carbon contamination on top of the ionic liquid and the signal from the carbon not bonded to nitrogen in the ethyl group of the ionic liquid. After Ar sputtering, the surface of active carbon cloth should be partially exposed due to the removal of adventitious carbon and ionic liquid electrolyte. Therefore,  $sp^2$  carbon becomes the dominant carbon species and 284.0 eV was again used as the reference for the discharged samples with sputtering.

For C 1s spectra, pristine sample exhibits typical  $sp^2$  carbon peak. For discharged sample, Four components corresponding to C-C/C-H (284.8 eV), C-N ( $286.0 \pm 0.1$  eV), N-C-N ( $287.1 \pm 0.1$  eV) and COOR ( $289.0 \pm 0.2$  eV) emerges. The C-C/C-H signal comes from the adventitious carbon and terminal carbon of the ethyl group. The C-N and N-C-N signals come from the residual ionic liquid electrolyte on sample surface. Ar sputtering partially removed the ionic liquid and exposed carbon surface, which can be seen from the reduced intensity of C-C/CH, C-N and N-C-N signals and the appearance of  $sp^2$  carbon, evidenced by the relative shift to lower binding energy of the main carbon component away from the C-N and N-C-N peaks.

The S 2p spectra were fitted with constrained spin orbit split doublets. Pristine ACC/S spectrum consists of minor sulfate (168.0 eV), minor elemental sulfur from cyclic elemental sulfur, such as  $S_5-S_8$  (164.0 eV) and a major component at 163.3 eV, due to the formation of short chain elemental sulfur species such as  $S_2-S_4$  due to the confinement of the micropores.<sup>[142]</sup> The lower binding energy of the S 2p for short chain sulfur ( $S_2-S_4$ ) makes sense due to the increased electron density expected around the nucleus due to the shorter S-S bond lengths<sup>[142]</sup> compared to the cyclic  $S_5-S_8$  molecules. Our data is in excellent agreement with previous studies using similar carbon/sulfur electrodes with a binding energy difference ( $\Delta BE$ ) of 120.7 eV between C 1s and S 2p, compared to  $120.8 \pm 0.1$  eV in the literature.<sup>[142][143][96][123]</sup> It should be noted however that our main elemental S 2p peak falls at  $\sim 163.3$  eV which is lower than that reported in the aforementioned references (163.7-164.1 eV,) this is simply due to the difference in our reference point of 284.0 eV for  $sp^2$  carbon versus 284.4-284.8 eV.

Discharged sample shows very noisy S 2p spectrum before sputtering due to the negligible amount of sulfur (0.04%) on surface. Because of the extremely low signal-to-noise ratio, no

curving fitting can be performed for analyzing sulfur's oxidation states. After sputtering, the intensity of sulfur signal increased dramatically. Curve fitting of S 2p spectra for discharged sample with both 1 hour and 4 hours sputtering reveals four components located at  $161.7 \pm 0.1$  eV,  $162.5 \pm 0.1$  eV,  $163.4 \pm 0.1$  eV and  $165.7 \pm 0.1$  eV. These four sets of peaks were assigned to fully reduced sulfur ( $S^{2-}$ ), partially reduced sulfur ( $S^{\cdot-}$ ), elemental sulfur and sulfite respectively based on XPS data of  $Al_2S_3$  standard and pristine electrode. Note that not all sulfur has been fully reduced, which is in good agreement with the electrochemical results, showing that at room temperature the sulfur utilization in the ACC/S cathode cannot reach 100%. Noteworthy, the surface of Al anode is free of dendrite after cycling (Figure 6-13). Based on these results, the reaction mechanism during discharge/charge was suggested as scheme 1:



**Scheme 1.** Discharge/Charge reaction mechanism of the Al/S battery at cathode and anode.

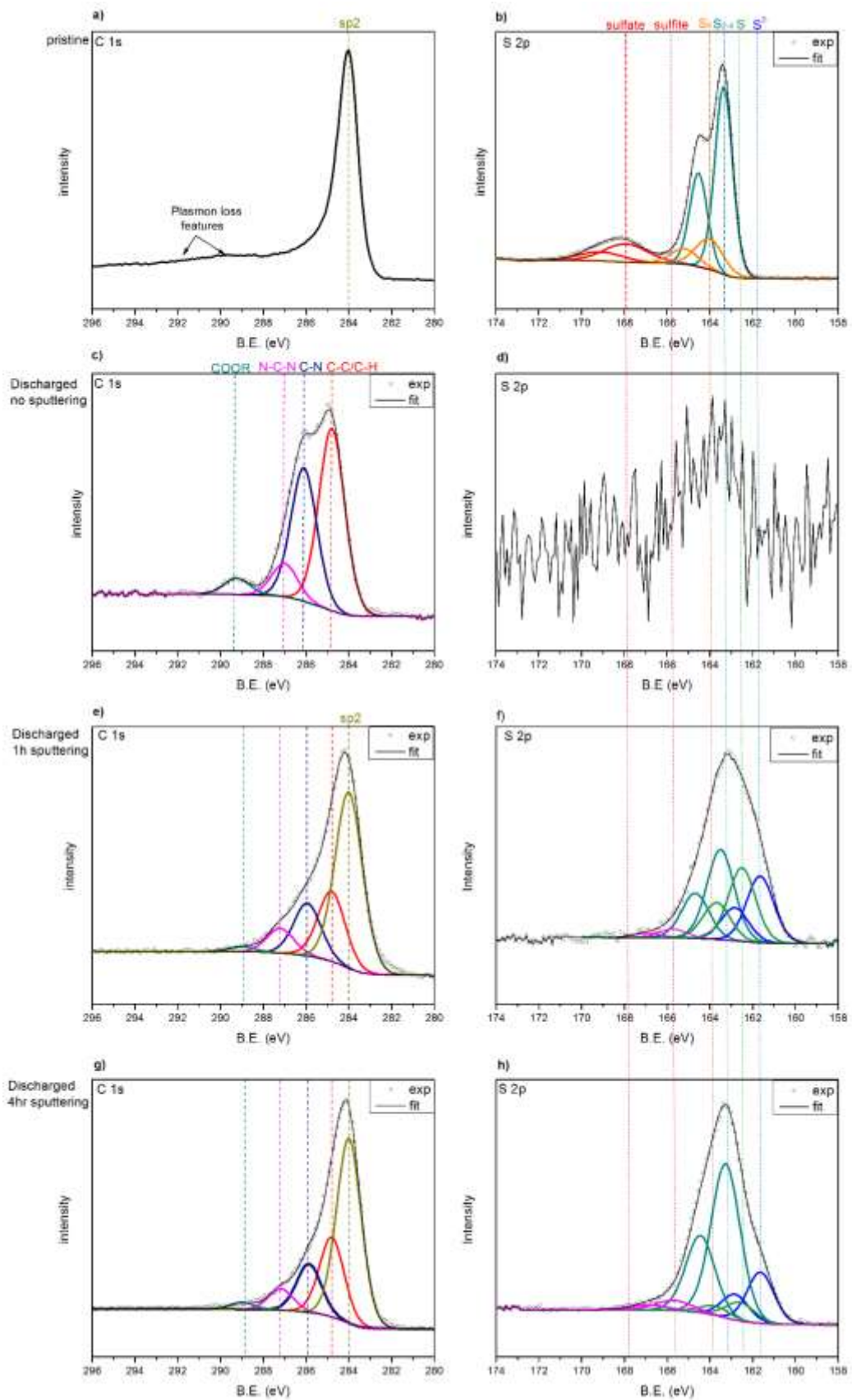


Figure 6-12. The high resolution C 1s and S 2p spectra of pristine ACC/S, discharged ACC/S with no sputtering, with 1 hour sputtering and with 4 hours sputtering.

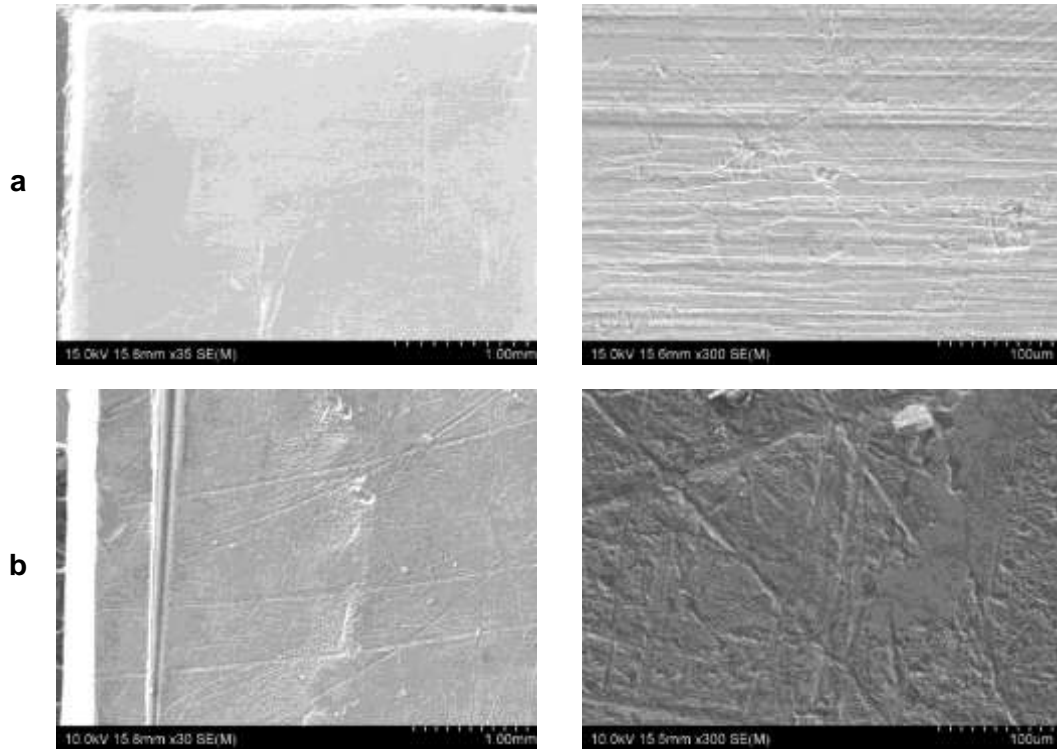


Figure 6-13. SEM images of pristine Al metal anode a) and Al metal anode after cycling b)

### Kinetics

A large voltage hysteresis ( $\sim 0.78$  V at 50 mA/g) was observed during charge/discharge (Figure 6-7, Figure 6-14), which leads to a low roundtrip efficiency of the Al/S system.

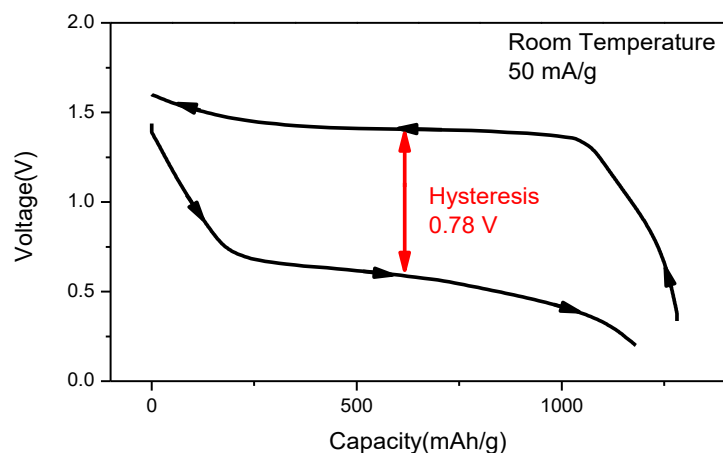
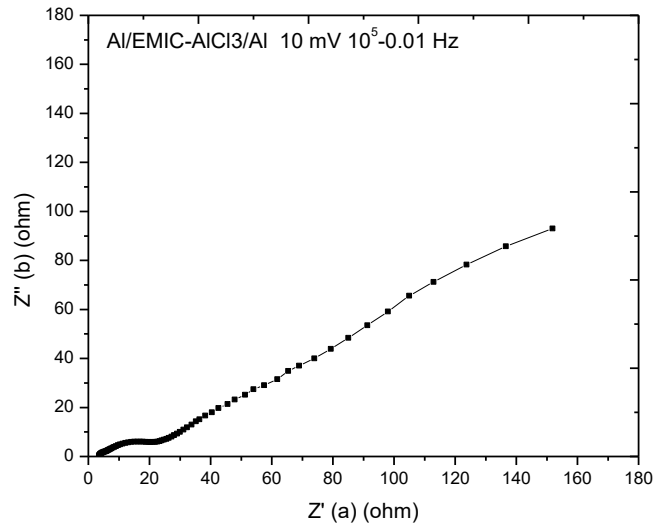
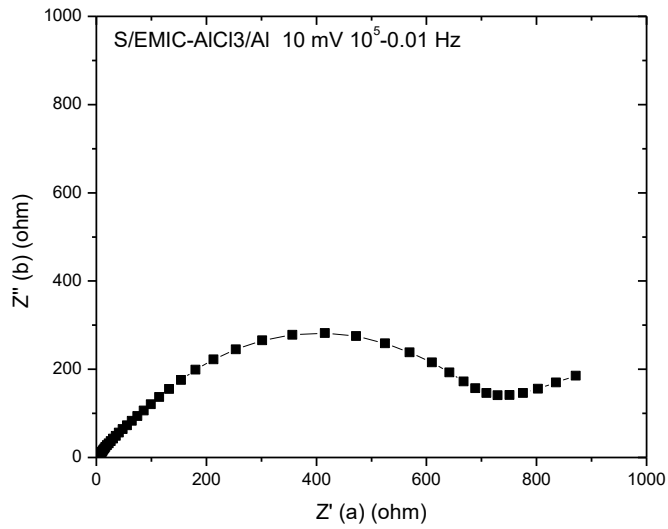


Figure 6-14. The voltage hysteresis of a Al/S cell at 50 mA/g, and room temperature

Among all kinetics inhibitors, ohmic resistance and anode charge transfer resistance are negligible owing to the electrolyte's high conductivity (15 mS/cm at 30 C)<sup>[62]</sup> and fast Al deposition/stripping kinetics (Figure 6-1). Electrochemical impedance spectroscopy (EIS) results confirmed this hypothesis and further pointed out that cathode charge transfer contributes significantly to the overall voltage loss (Figure 6-15), which is expected for the solid state sulfur conversion reaction.



a)



b)

Figure 6-15. a) EIS of a symmetrical Al/EMIC-AlCl<sub>3</sub>/Al cell after several cycles.  $R_{ohm}=3.5$  ohm,  $R_{ct} = 20$  ohm. b) EIS of an Al/S cell after several cycles.  $R_{ohm}=2.78$  ohm,  $R_{ct}=750$  ohm. From the impedance result we can infer in an Al/S cell, the ohmic resistance is  $\sim 3$  ohm, charge transfer resistance of anode reaction (Al deposition/stripping) is  $\sim 10$  ohm, while

charge transfer resistance of cathode reaction is almost two orders higher (750 ohm-10 ohm=740 ohm).

Additionally, polarization due to the sluggish  $\text{Al}^{3+}$  diffusion in  $\text{AlS}_x$  and  $\text{S}/\text{AlS}_x$  phase boundary movement should also pose a large impact on the kinetics. A depolarization experiment was performed to evaluate the magnitude of these polarizations (Figure 6-16): A sudden voltage jump of  $< 0.15$  V, accounting for the fast removal of ohmic overpotential and charge transfer overpotential, was observed immediately after the applied current was withdrawn. In contrast, it takes more than 24 hours to eliminate other polarizations ( $>0.3$  V) and relax the battery potential to equilibrium. In summary, the Al/S battery is kinetically limited by the solid state sulfur conversion reaction (including interfacial charge transfer, subsequent  $\text{Al}^{3+}$  diffusion and phase boundary movement).

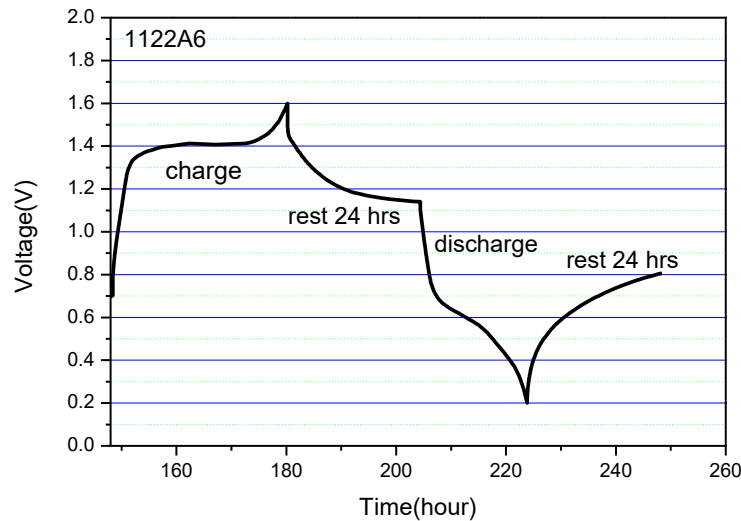


Figure 6-16. Voltage-time curve of a typical Al/S cell. It takes  $> 24$  hours for the system to completely remove all polarization and reach equilibrium. This indicates that diffusion of  $\text{Al}^{3+}$  in solid phase and  $\text{S}/\text{AlS}_x$  phase boundary movement are very slow during the operation

of the Al/S cell. The sluggish diffusion of  $\text{Al}^{3+}$  in solid phase can be expected from its large charge/radius ratio.

To mitigate the polarizations, we intentionally elevated experiment temperature to 50 °C. The discharge plateau was raised to 0.75 V and the charge plateau was lowered to 1.25 V as a result of the expedited kinetics (Figure 6-17a). Clear decline in voltage hysteresis to 0.5 V was observed from dQ/dV curve after raising the temperature (Figure 6-17b). A high capacity of 1750 mAh/g<sub>s</sub> (including the capacitive storage of carbon) reveals higher sulfur utilization of 83%.

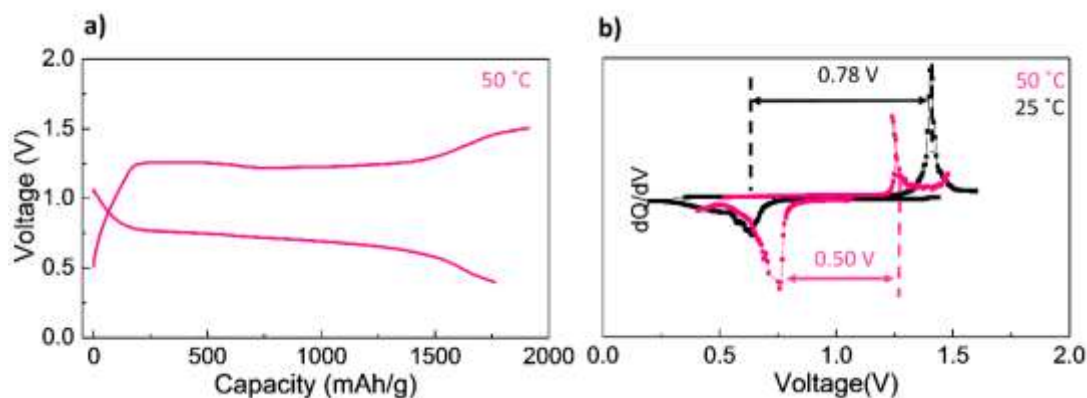


Figure 6-17. a) charge/discharge curve at 50 °C(50 mA/g) and b) dQ/dV curve of Al/S cell at different temperatures;

### Conclusion

In conclusion, we demonstrated the first rechargeable Al/S battery with an ionic liquid electrolyte, by addressing the hurdle for oxidizing  $\text{AlS}_x$  with a microporous carbon/sulfur cathode that can fortify the electron access of sulfur species, enlarge interfacial reaction area and reduce  $\text{Al}^{3+}$  diffusion length. Experimental results indicate that sulfur undergoes solid state conversion reaction in the electrolyte. The readiness to oxidize  $\text{AlS}_x$  and low sulfur loss into

the electrolyte renders a substantially improved reversibility: a capacity of 1000 mAh/g<sub>s</sub> for over 20 cycles, corresponding to an obtainable energy density of 650 Wh/kg. Moreover, The Al/S system shows dendrite free deposition/stripping at Al anode. The large voltage hysteresis is a result of the sluggish solid state reaction and Al<sup>3+</sup> diffusion, which can be effectively reduced by elevating temperature. The scientific insights obtained in this work sheds lights on electrochemical sulfur reaction in tri-valent cation environment and will facilitate progress on the way to realize a rechargeable Al/S battery.



## Chapter 7 Summary and Future Work

### Hybrid Mg/Li Battery

In this dissertation, I demonstrated a concept hybrid Mg/Li battery which couples a Li<sup>+</sup> intercalation cathode with Mg metal anode in a mixed Mg<sup>2+</sup>/Li<sup>+</sup> electrolyte. This hybrid battery is able to bypass the sluggish Mg intercalation kinetics at cathode while maintaining the high capacity feature of Mg anode. The concept battery shows an energy density of ~200 Wh/kg, which is still not competitive with state-of-the-art Li ion battery. However, if the cathode used here (TiS<sub>2</sub>) is replaced by high voltage cathode such as LiCoO<sub>2</sub>, the hybrid battery is able to provide an energy density comparable to Li ion battery. This improvement is based on the development of electrolyte compatible with high voltage Li intercalation cathode, for example, NMC, NCA, Li-rich material etc.

Future work can explore the feasibility of pairing these high voltage cathode with Mg metal. The interfacial stability and the reaction reversibility needs to be examined carefully. The amount of electrolyte, which is necessary to ensure high capacity operation, also needs deliberate consideration.

### Mg/I<sub>2</sub> battery

In this dissertation, I demonstrated a concept Mg/I<sub>2</sub> battery, which utilizes the dissolution of I<sub>2</sub> and polyiodide to achieve fast reaction kinetics. Our preliminary study justifies the chemical reversibility and high rate capability of this redox chemistry. However, the cycling stability of this redox chemistry, which is crucial for rechargeable battery, is subject to deliberate

consideration, since the dissolution of active material causes the loss of capacity. The synergetic effect of cathode structure optimization and electrolyte improvement is proved to be an effective method in our study. The high power performance of the liquid-solid two phase reaction also provides an alternative design strategy for addressing the cathode kinetics limitation for Mg batteries.

Future work can focus on either improving the stability of the system via further cathode optimization and electrolyte improvement, or developing semi-flow battery based on the soluble iodine redox couple.

### *Al/S battery*

In this dissertation, I made the first rechargeable Al/S battery via improving the oxidation kinetics of aluminum sulfide by confining the sulfur particle into nanosized carbon pores. The sulfur reduction in the ionic liquid occurs in a solid state route, which causes large voltage hysteresis. This is an intrinsic problem for multivalent battery system, since the solid state diffusion of the multivalent ion, which is an important step in the electrochemical reaction, is limiting the overall kinetics and posing large energy penalty for the system.

Nevertheless, Al/S battery is still promising especially for low cost applications. Future work can focus on finding proper electrolyte to dissolve aluminum sulfide so that the reaction kinetics can be remarkably improved.

## Mg/S battery

In this dissertation, I investigated the thermodynamics and kinetics of the Mg/S chemistry for the first time. This is especially important for the fundamental understanding of the reduction/oxidation route of sulfur cathode in Mg chemistry. The electrolyte used in previous studies renders severe dissolution of Mg polysulfide, therefore causing huge difficulty for obtaining the equilibrium state of sulfur cathode at different Mg concentration. In our study, I used MgTFSI<sub>2</sub>-DME electrolyte in three-electrode configuration and successfully addressed this issue.

The reaction kinetics of sulfur in Mg chemistry is highly dependent on the reaction product. For first electron transfer the reaction is very fast, which renders sulfur a very good cathode which possesses both high capacity and fast reaction kinetics. However, the reaction reversibility needs to be further improved for practical application. On the other hand, the reaction kinetics need to be maintained at high sulfur loading. Future work can focus on these two directions.



## Bibliography

- [1] D. Larcher, J.-M. Tarascon, *Nat. Chem.* **2014**, 7, 19–29.
- [2] J.-M. Tarascon, *Nat. Chem.* **2010**, 2, 510.
- [3] B. Scrosati, J. Garche, *J. Power Sources* **2010**, 195, 2419–2430.
- [4] B. L. Ellis, K. T. Lee, L. F. Nazar, *Chem. Mater.* **2010**, 22, 691–714.
- [5] J. B. Goodenough, Y. Kim, *Chem. Mater.* **2010**, 22, 587–603.
- [6] W. Xu, J. Wang, F. Ding, X. Chen, E. Nasybulin, Y. Zhang, J.-G. Zhang, *Energy Environ. Sci.* **2014**, 7, 513–537.
- [7] P. Bai, J. Li, F. R. Brushett, M. Z. Bazant, *Energy Environ. Sci.* **2016**, 13–17.
- [8] D. Aurbach, E. Zinigrad, Y. Cohen, H. Teller, *Solid State Ionics* **2002**, 148, 405–416.
- [9] W. Li, H. Yao, K. Yan, G. Zheng, Z. Liang, Y.-M. Chiang, Y. Cui, *Nat. Commun.* **2015**, 6, 7436.
- [10] X. Ji, K. T. Lee, L. F. Nazar, *Nat. Mater.* **2009**, 8, 500–506.
- [11] J. Lu, Y. Jung Lee, X. Luo, K. Chun Lau, M. Asadi, H.-H. Wang, S. Brombosz, J. Wen, D. Zhai, Z. Chen, et al., *Nature* **2016**, 529, 1–7.
- [12] C. P. G. Tao Liu<sup>1</sup>, Michal Leskes<sup>1,†</sup>, Wanjing Yu<sup>1, 2,‡</sup>, Amy J. Moore<sup>1</sup>, Lina Zhou<sup>1</sup>, Paul M. Bayley<sup>1</sup>, Gunwoo Kim<sup>1, 2</sup>, *Science (80-. )*. **2015**, 170–175.
- [13] Y. Chen, S. a Freunberger, Z. Peng, O. Fontaine, P. G. Bruce, *Nat. Chem.* **2013**, 5, 489–94.
- [14] S. Urbonaite, T. Poux, P. Novák, *Adv. Energy Mater.* **2015**, n/a–n/a.
- [15] G. Girishkumar, B. McCloskey, A. C. Luntz, S. Swanson, W. Wilcke, *J. Phys. Chem. Lett.* **2010**, 1, 2193–2203.
- [16] D. Aurbach, B. D. McCloskey, L. F. Nazar, P. G. Bruce, *Nat. Energy* **2016**, 1, 16128.

- [17] J. Muldoon, C. B. Bucur, T. Gregory, *Chem. Rev.* **2014**, *114*, 11683–11720.
- [18] H. D. Yoo, I. Shterenberg, Y. Gofer, G. Gershinsky, N. Pour, D. Aurbach, *Energy Environ. Sci.* **2013**, *6*, 2265–2279.
- [19] M. Liu, Z. Rong, R. Malik, P. Canepa, A. Jain, G. Ceder, K. A. Persson, *Energy Environ. Sci.* **2015**, *8*, 964–974.
- [20] T. D. T. Gregory, R. R. J. Hoffman, R. C. R. Winterton, *J. Electrochem. Soc.* **1990**, *137*, 2–7.
- [21] D. Aurbach, Z. Lu, a Schechter, Y. Gofer, H. Gizbar, R. Turgeman, Y. Cohen, M. Moshkovich, E. Levi, *Nature* **2000**, *407*, 724–727.
- [22] E. Levi, M. D. Levi, O. Chasid, D. Aurbach, *J. Electroceramics* **2009**, *22*, 13–19.
- [23] Z. Lu, a. Schechter, M. Moshkovich, D. Aurbach, *J. Electroanal. Chem.* **1999**, *466*, 203–217.
- [24] T. D. Gregory, *J. Electrochem. Soc.* **1990**, *137*, 775.
- [25] R. Mohtadi, F. Mizuno, *Beilstein J. Nanotechnol.* **2014**, *5*, 1291–311.
- [26] D. Aurbach, H. Gizbar, A. Schechter, O. Chusid, H. E. Gottlieb, Y. Gofer, I. Goldberg, *J. Electrochem. Soc.* **2002**, *149*, A115.
- [27] O. Mizrahi, N. Amir, E. Pollak, O. Chusid, V. Marks, H. Gottlieb, L. Larush, E. Zinigrad, D. Aurbach, *J. Electrochem. Soc.* **2008**, *155*, A103.
- [28] E. G. Nelson, S. I. Brody, J. W. Kampf, B. M. Bartlett, **2014**, 18194–18198.
- [29] R. E. Doe, R. Han, J. Hwang, A. J. Gmitter, I. Shterenberg, H. D. Yoo, N. Pour, D. Aurbach, *Chem. Commun. (Camb)*. **2014**, *50*, 243–5.
- [30] R. Mohtadi, M. Matsui, T. S. Arthur, S. J. Hwang, *Angew. Chemie - Int. Ed.* **2012**, *51*, 9780–9783.
- [31] T. J. Carter, R. Mohtadi, T. S. Arthur, F. Mizuno, R. Zhang, S. Shirai, J. W. Kampf,

- Angew. Chemie Int. Ed.* **2014**, *53*, 3173–3177.
- [32] O. Tutusaus, R. Mohtadi, T. S. Arthur, F. Mizuno, E. G. Nelson, Y. V. Sevryugina, *Angew. Chemie Int. Ed.* **2015**, *54*, 7900–7904.
- [33] S. Y. Ha, Y. W. Lee, S. W. Woo, B. Koo, J. S. Kim, J. Cho, K. T. Lee, N. S. Choi, *ACS Appl. Mater. Interfaces* **2014**, *6*, 4063–4073.
- [34] N. Sa, H. Wang, D. L. Proffit, A. L. Lipson, B. Key, M. Liu, Z. Feng, T. T. Fister, Y. Ren, C.-J. Sun, et al., *J. Power Sources* **2016**, *323*, 44–50.
- [35] I. Shterenberg, M. Salama, H. D. Yoo, Y. Gofer, J.-B. Park, Y.-K. Sun, D. Aurbach, *J. Electrochem. Soc.* **2015**, *162*, A7118–A7128.
- [36] P. Novak, R. Imhof, O. Haas, **1999**, *45*.
- [37] N. Amir, Y. Vestfrid, O. Chusid, Y. Gofer, D. Aurbach, *J. Power Sources* **2007**, *174*, 1234–1240.
- [38] S. Rasul, S. Suzuki, S. Yamaguchi, M. Miyayama, *Solid State Ionics* **2012**, *225*, 542–546.
- [39] R. Zhang, X. Yu, K. W. Nam, C. Ling, T. S. Arthur, W. Song, A. M. Knapp, S. N. Ehrlich, X. Q. Yang, M. Matsui, *Electrochem. commun.* **2012**, *23*, 110–113.
- [40] R. Zhang, F. Mizuno, C. Ling, *Chem. Commun.* **2015**, *51*, 1108–1111.
- [41] Y. Gu, Y. Katsura, T. Yoshino, H. Takagi, K. Taniguchi, *Sci. Rep.* **2015**, *5*, 12486.
- [42] K. Taniguchi, Y. Gu, Y. Katsura, T. Yoshino, H. Takagi, *Appl. Phys. express* **2016**, *011801*, 1–5.
- [43] Z. Rong, R. Malik, P. Canepa, G. Sai Gautam, M. Liu, A. Jain, K. Persson, G. Ceder, *Chem. Mater.* **2015**, *27*, 6016–6021.
- [44] M. Liu, A. Jain, Z. Rong, X. Qu, P. Canepa, R. Malik, G. Ceder, K. A. Persson, D. Aurbach, Z. Lu, et al., *Energy Environ. Sci.* **2016**, *9*, 3201–3209.

- [45] X. Sun, P. Bonnicks, V. Duffort, M. Liu, Z. Rong, K. A. Persson, G. Ceder, L. F. Nazar, *Energy Environ. Sci.* **2016**, *9*, 2273–2277.
- [46] J. T. Inconvati, L. F. Wan, B. Key, D. Zhou, C. Liao, L. Fuoco, M. Holland, H. Wang, D. Prendergast, K. R. Poepelmeier, et al., *Chem. Mater.* **2016**, *28*, 17–20.
- [47] W. Kaveevivitchai, A. J. Jacobson, *Chem. Mater.* **2016**, *28*, 4593–4601.
- [48] A. L. Lipson, S. Han, S. Kim, B. Pan, N. Sa, C. Liao, T. T. Fister, A. K. Burrell, J. T. Vaughey, B. J. Ingram, *J. Power Sources* **2016**, *325*, 646–652.
- [49] D. M. Kim, Y. Kim, D. Arumugam, S. W. Woo, Y. N. Jo, M. S. Park, Y. J. Kim, N. S. Choi, K. T. Lee, *ACS Appl. Mater. Interfaces* **2016**, *8*, 8554–8560.
- [50] C. Ling, R. Zhang, F. Mizuno, *ACS Appl. Mater. & Interfaces* **2016**, *8*, 4508–4515.
- [51] V. Duffort, X. Sun, L. F. Nazar, *Chem. Commun.* **2016**, *52*, 12458–12461.
- [52] Y. Tashiro, K. Taniguchi, H. Miyasaka, *Electrochim. Acta* **2016**, *210*, 655–661.
- [53] R. Zhang, C. Ling, F. Mizuno, *Chem. Commun.* **2014**, 2–5.
- [54] B. Pan, D. Zhou, J. Huang, L. Zhang, A. K. Burrell, J. T. Vaughey, Z. Zhang, C. Liao, **2016**, *163*, 580–583.
- [55] B. Pan, J. Huang, Z. Feng, L. Zeng, M. He, L. Zhang, J. T. Vaughey, M. J. Bedzyk, P. Fenter, Z. Zhang, et al., *Adv. Energy Mater.* **2016**, *6*, 2–4.
- [56] X. Sun, P. Bonnicks, L. F. Nazar, *ACS Energy Lett.* **2016**, DOI 10.1021/acseenergylett.6b00145.
- [57] H. S. Kim, T. S. Arthur, G. D. Allred, J. Zajicek, J. G. Newman, A. E. Rodnyansky, A. G. Oliver, W. C. Boggess, J. Muldoon, *Nat. Commun.* **2011**, *2*, 427.
- [58] G. Vardar, E. G. Nelson, J. G. Smith, J. Naruse, H. Hiramatsu, B. M. Bartlett, A. E. S. Sleightholme, D. J. Siegel, C. W. Monroe, *Chem. Mater.* **2015**,

acs.chemmater.5b03608.

- [59] T. Shiga, Y. Hase, Y. Yagi, N. Takahashi, K. Takechi, *J. Phys. Chem. Lett* **2014**, *5*, 1648–1652.
- [60] R. T. Carlin, W. Crawford, M. Bersch, *J. Electrochem. Soc.* **1992**, *139*, 2720–2727.
- [61] S. Takahashi, L. a. Curtiss, D. Gosztola, N. Koura, M.-L. Saboungi, *Inorg. Chem.* **1995**, *34*, 2990–2993.
- [62] T. Jiang, M. J. Chollier Brym, G. Dubé, a. Lasia, G. M. Brisard, *Surf. Coatings Technol.* **2006**, *201*, 1–9.
- [63] L. Legrand, *J. Electrochem. Soc.* **1994**, *141*, 378.
- [64] L. Legrand, A. Tranchant, R. Messina, *Electrochim. Acta* **1994**, *39*, 1427–1431.
- [65] A. KITADA, K. NAKAMURA, K. FUKAMI, K. MURASE, *Electrochemistry* **2014**, *82*, 946–948.
- [66] M.-C. Lin, M. Gong, B. Lu, Y. Wu, D.-Y. Wang, M. Guan, M. Angell, C. Chen, J. Yang, B.-J. Hwang, et al., *Nature* **2015**, DOI 10.1038/nature14340.
- [67] M. Chiku, H. Takeda, S. Matsumura, E. Higuchi, H. Inoue, *ACS Appl. Mater. Interfaces* **2015**, 151022062337009.
- [68] G. Cohn, L. Ma, L. a. Archer, *J. Power Sources* **2015**, *283*, 416–422.
- [69] J. Muldoon, C. B. Bucur, A. G. Oliver, T. Sugimoto, M. Matsui, H. S. Kim, G. D. Allred, J. Zajicek, Y. Kotani, *Energy Environ. Sci.* **2012**, *5*, 5941.
- [70] Y. Gofer, O. Chusid, H. Gizbar, Y. Viestfrid, H. E. Gottlieb, V. Marks, D. Aurbach, *Electrochem. Solid-State Lett.* **2006**, *9*, A257.
- [71] T. Gao, F. Han, Y. Zhu, L. Suo, C. Luo, K. Xu, C. Wang, *Adv. Energy Mater.* **2014**, *5*, 1401507.
- [72] H. D. Yoo, Y. Liang, Y. Li, Y. Yao, *ACS Appl. Mater. Interfaces* **2015**,

150323142029005.

- [73] S. Yagi, T. Ichitsubo, Y. Shirai, S. Yanai, T. Doi, K. Murase, E. Matsubara, *J. Mater. Chem. A* **2014**, *2*, 1144.
- [74] Y. Cheng, Y. Shao, J.-G. Zhang, V. L. Sprenkle, J. Liu, G. Li, *Chem. Commun. (Camb)*. **2014**, *50*, 9644–9646.
- [75] K. W. Nam, S. Kim, S. Lee, M. Salama, I. Shterenberg, Y. Gofer, J.-S. Kim, E. Yang, C. S. Park, J.-S. Kim, et al., *Nano Lett.* **2015**, 150518113929005.
- [76] X. Sun, V. Duffort, B. L. Mehdi, N. D. Browning, L. F. Nazar, *Chem. Mater.* **2015**, acs.chemmater.5b03983.
- [77] G. Sai Gautam, P. Canepa, W. D. Richards, R. Malik, G. Ceder, *Nano Lett.* **2016**, acs.nanolett.5b05273.
- [78] I. Shterenberg, M. Salama, Y. Gofer, E. Levi, D. Aurbach, *MRS Bull.* **2014**, *39*, 453–460.
- [79] S. S. Zhang, *J. Power Sources* **2013**, *231*, 153–162.
- [80] R. Elazari, G. Salitra, A. Garsuch, A. Panchenko, D. Aurbach, *Adv. Mater.* **2011**, *23*, 5641–5644.
- [81] T. Gao, M. Noked, A. J. Pearse, E. Gillette, X. Fan, Y. Zhu, C. Luo, L. Suo, M. a Schroeder, K. Xu, et al., *J. Am. Chem. Soc.* **2015**, 150911151245004.
- [82] Z. Zhao-Karger, X. Zhao, D. Wang, T. Diemant, R. J. Behm, M. Fichtner, *Adv. Energy Mater.* **2015**, *5*, 1401155.
- [83] <http://webbook.nist.gov/chemistry/form-ser.html> **n.d.**
- [84] Z. Zhao-Karger, X. Zhao, O. Fuhr, M. Fichtner, *RSC Adv.* **2013**, *3*, 16330.
- [85] L. Suo, Y.-S. Hu, H. Li, M. Armand, L. Chen, *Nat. Commun.* **2013**, *4*, 1481.
- [86] T. Zhang, K. Liao, P. He, H. Zhou, *Energy Environ. Sci.* **2015**, *9*, 1024–1030.

- [87] Q. Zhang, Y. Liu, Y. Duan, N. Fu, Q. Liu, Y. Fang, Q. Sun, Y. Lin, *RSC Adv.* **2014**, *4*, 15091.
- [88] C. C. Clark, A. Marton, R. Srinivasan, A. A. Narducci Sarjeant, G. J. Meyer, *Inorg. Chem.* **2006**, *45*, 4728–4734.
- [89] P. M. A. Sherwood, *J. Chem. Soc.* **1976**, 1805–1820.
- [90] A. Hanom Ahmad, F. S. Abdul Ghani, *AIP Conf. Proc.* **2009**, *1136*, 31–35.
- [91] X. Liang, C. Hart, Q. Pang, A. Garsuch, T. Weiss, L. F. Nazar, *Nat. Commun.* **2015**, *6*, 5682.
- [92] X. Ji, L. F. Nazar, *J. Mater. Chem.* **2010**, *20*, 9821.
- [93] X. Tao, J. Wang, C. Liu, H. Wang, H. Yao, G. Zheng, Z. W. Seh, Q. Cai, W. Li, G. Zhou, et al., *Nat. Commun.* **2016**, *7*, 11203.
- [94] Q. Pang, D. Kundu, M. Cuisinier, L. F. Nazar, *Nat Commun* **2014**, *5*, 4759.
- [95] Y. S. Su, A. Manthiram, *Nat Commun* **2012**, *3*, 1166.
- [96] Y. Xu, Y. Wen, Y. Zhu, K. Gaskell, K. A. Cychosz, B. Eichhorn, K. Xu, C. Wang, *Adv. Funct. Mater.* **2015**, *25*, 4312–4320.
- [97] Z. Zhang, Z. Cui, L. Qiao, J. Guan, H. Xu, X. Wang, P. Hu, H. Du, S. Li, X. Zhou, et al., *Adv. Energy Mater.* **2017**, *201602055*, 1602055.
- [98] X. Yu, A. Manthiram, *ACS Energy Lett.* **2016**, *28*, 896–905.
- [99] V. B P, Z. Zhao-Karger, T. Diemant, V. S. K. Chakravadhanula, N. I. Schwarzburger, M. A. Cambaz, R. J. Behm, C. Kuebel, M. Fichtner, *Nanoscale* **2015**, DOI 10.1039/C5NR04383B.
- [100] W. Li, S. Cheng, J. Wang, Y. Qiu, Z. Zheng, H. Lin, S. Nanda, Q. Ma, Y. Xu, F. Ye, et al., *Angew. Chemie Int. Ed.* **2016**, 1–6.
- [101] Z. Zhao-Karger, X.-M. Lin, C. Bonatto Minella, D. Wang, T. Diemant, R. J. Behm,

- M. Fichtner, *J. Power Sources* **2016**, 323, 213–219.
- [102] A. K. Rajagopal, J. Callaway, *Phys. Rev. B* **1973**, 7, 1912–1919.
- [103] G. Kresse, J. Hafner, *Phys. Rev. B* **1994**, 49, 14251–14269.
- [104] W. Kohn, L. J. Sham, *Phys. Rev.* **1965**, 140, DOI 10.1103/PhysRev.140.A1133.
- [105] Z. Zhu, I. H. Chu, Z. Deng, S. P. Ong, *Chem. Mater.* **2015**, 27, 8318–8325.
- [106] S. P. Ong, Y. Mo, W. D. Richards, L. Miara, H. S. Lee, G. Ceder, *Energy Environ. Sci.* **2012**, 12, 148–156.
- [107] K. Momma, F. Izumi, *J. Appl. Crystallogr.* **2011**, 44, 1272–1276.
- [108] R. D. Rauh, F. S. Shuker, J. M. Marston, S. B. Brummer, *J. Inorg. Nucl. Chem.* **1977**, 39, 1761–1766.
- [109] R. D. Rauh, K. M. Abraham, G. F. Pearson, J. K. Surprenant, S. B. Brummer, E. I. C. Corporation, *J. Electrochem. Soc.* **1979**.
- [110] M. Cuisinier, P.-E. Cabelguen, B. D. Adams, A. Garsuch, M. Balasubramanian, L. F. Nazar, *Energy Environ. Sci.* **2014**, 7, 2697.
- [111] E. G. Nelson, S. I. Brody, J. W. Kampf, B. M. Bartlett, *J. Mater. Chem. A* **2014**, 2, 18194–18198.
- [112] C. Barchasz, F. Molton, C. Duboc, *Anal. Chem.* **2012**, 84, 3973–3980.
- [113] J.-T. Yeon, J.-Y. Jang, J.-G. Han, J. Cho, K. T. Lee, N.-S. Choi, *J. Electrochem. Soc.* **2012**, 159, A1308–A1314.
- [114] H. Park, H. S. Koh, D. J. Siegel, *J. Phys. Chem. C* **2015**, 119, 4675–4683.
- [115] S. Waluś, C. Barchasz, R. Bouchet, J.-C. Leprêtre, J.-F. Colin, J.-F. Martin, E. Elkaim, C. Baetz, F. Alloin, *Adv. Energy Mater.* **2015**, n/a–n/a.
- [116] H.-L. Wu, L. a Huff, A. a Gewirth, *ACS Appl. Mater. Interfaces* **2015**, 7, 1709–19.
- [117] M. Hagen, P. Schiffels, M. Hammer, S. Dorfler, J. Tubke, M. J. Hoffmann, H.

- Althues, S. Kaskel, *J. Electrochem. Soc.* **2013**, *160*, A1205–A1214.
- [118] S. Zhang, K. Ueno, K. Dokko, M. Watanabe, *Adv. Energy Mater.* **2015**, 1500117.
- [119] A. Swiderska-Mocek, E. Rudnicka, *J. Power Sources* **2015**, *273*, 162–167.
- [120] N. A. Cañas, S. Wolf, N. Wagner, K. A. Friedrich, *J. Power Sources* **2013**, *226*, 313–319.
- [121] J. Nelson, S. Misra, Y. Yang, A. Jackson, Y. Liu, H. Wang, H. Dai, J. C. Andrews, Y. Cui, M. F. Toney, *J. Am. Chem. Soc.* **2012**, *134*, 6337–6343.
- [122] T. Gao, X. Li, X. Wang, J. Hu, F. Han, X. Fan, L. Suo, A. J. Pearse, S. B. Lee, G. W. Rubloff, et al., *Angew. Chemie Int. Ed.* **2016**, 1–5.
- [123] M. Helen, M. A. Reddy, T. Diemant, U. Golla-Schindler, R. J. Behm, U. Kaiser, M. Fichtner, *Sci. Rep.* **2015**, *5*, 12146.
- [124] H. Lindström, S. Södergren, A. Solbrand, H. Rensmo, J. Hjelm, A. Hagfeldt, S.-E. Lindquist, *J. Phys. Chem. B* **1997**, *101*, 7717–7722.
- [125] M. Cuisinier, P. E. Cabelguen, S. Evers, G. He, M. Kolbeck, A. Garsuch, T. Bolin, M. Balasubramanian, L. F. Nazar, *J. Phys. Chem. Lett.* **2013**, *4*, 3227–3232.
- [126] T. Liu, Y. Shao, G. Li, M. Gu, J. Hu, S. Xu, Z. Nie, X. Chen, C. Wang, J. Liu, *J. Mater. Chem. A* **2014**, *2*, 3430.
- [127] L. Bai, B. E. Conway, *J. Electrochem. Soc.* **1990**, *137*, 3737–3747.
- [128] H. Wang, S. Gu, Y. Bai, S. Chen, N. Zhu, C. Wu, F. Wu, *J. Mater. Chem. A* **2015**, DOI 10.1039/C5TA06187C.
- [129] P. R. Gifford, J. B. Palmisano, *J. Electrochem. Soc.* **1988**, *135*, 650–654.
- [130] J. V. Rani, V. Kanakaiah, T. Dadmal, M. S. Rao, S. Bhavanarushi, *J. Electrochem. Soc.* **2013**, *160*, A1781–A1784.
- [131] T. Tsuda, I. Kokubo, M. Kawabata, M. Yamagata, M. Ishikawa, S. Kusumoto, a.

- Imanishi, S. Kuwabata, *J. Electrochem. Soc.* **2014**, *161*, A908–A914.
- [132] W. Wang, B. Jiang, W. Xiong, H. Sun, Z. Lin, L. Hu, J. Tu, J. Hou, H. Zhu, S. Jiao, *Sci. Rep.* **2013**, *3*, 3383.
- [133] N. Jayaprakash, S. K. Das, L. a. Archer, *Chem. Commun.* **2011**, *47*, 12610.
- [134] T. Gao, M. Noked, A. J. Pearse, E. Gillette, X. Fan, Y. Zhu, C. Luo, L. Suo, M. A. Schroeder, K. Xu, et al., *J. Am. Chem. Soc.* **2015**, *137*, 12388–12393.
- [135] S. Xin, Y.-X. Yin, Y.-G. Guo, L.-J. Wan, *Adv. Mater.* **2014**, *26*, 1261–1265.
- [136] S. Wenzel, H. Metelmann, C. Raiß, A. K. Dürr, J. Janek, P. Adelhelm, *J. Power Sources* **2013**, *243*, 758–765.
- [137] A. C. Kozen, C.-F. Lin, A. J. Pearse, M. A. Schroeder, X. Han, L. Hu, S.-B. Lee, G. W. Rubloff, M. Noked, *ACS Nano* **2015**, *9*, 5884–5892.
- [138] L. X. Yuan, J. K. Feng, X. P. Ai, Y. L. Cao, S. L. Chen, H. X. Yang, *Electrochem. commun.* **2006**, *8*, 610–614.
- [139] M. Nagao, A. Hayashi, M. Tatsumisago, *Electrochim. Acta* **2011**, *56*, 6055–6059.
- [140] G. Zhou, E. Paek, G. S. Hwang, A. Manthiram, *Nat. Commun.* **2015**, *6*, 7760.
- [141] K. Laajalehto, I. Kartio, P. Nowak, *Appl. Surf. Sci.* **1994**, *81*, 11–15.
- [142] S. Xin, L. Gu, N. Zhao, Y. Yin, L. Zhou, Y. Guo, L. Wan, *J. Am. Chem. Soc.* **2012**, *134*, 18510–18513.
- [143] S. Zheng, P. Han, Z. Han, H. Zhang, Z. Tang, J. Yang, *Sci. Rep.* **2014**, *4*, 4842.

## Peer Reviewed Publications

1. Y. Zhu<sup>†</sup>, **T. Gao**<sup>†</sup>, X. Fan, F. Han, C. Wang, Electrochemical Techniques for Intercalation Compounds in Rechargeable Batteries, *Account of Chemical Research*, Accepted, 2017
2. H. Tian<sup>†</sup>, **T. Gao**<sup>†</sup>, X. Li, X. Wang, C. Luo, X. Fan, C. Yang, L. Suo, Z. Ma, W. Han, and C. Wang, High Power Rechargeable Magnesium/iodine Battery Chemistry, *Nature Communications*, Accepted, 2016
3. **T. Gao**, X. Li, X. Wang, F. Han, X. Fan, L. Suo, A. J. Pearse, S. B. Lee, G. W. Rubloff, M. Noked and C. Wang, Rechargeable Al/S Battery with Ionic Liquid Electrolyte, *Angew.*

*Chem. Int. Ed.* 55(2016), 9898-9901

4. **T. Gao**<sup>†</sup>, M. Noked<sup>†</sup>, A. J. Pearse, E. Gillette, X. Fan, Y. Zhu, C. Luo, L. Suo, M. A. Schroeder, K. Xu, S. B. Lee, G. W. Rubloff, C. Wang, Enhancing the Reversibility of Mg/S Battery Chemistry through Li<sup>+</sup> Mediation, *Journal of American Chemical Society*, 37(2015)12388. Highlighted by C&EN
5. **T. Gao**, F. Han, Y. Zhu, L. Suo, C. Luo, K. Xu and C. Wang, Hybrid Mg<sup>2+</sup>/Li<sup>+</sup> Battery with Long Cycle Life and High Rate Capability, *Advanced Energy Materials*, DOI: 10.1002/aenm.201401507. Highlited by Materials View.
6. X. Wang, **T. Gao**, F. Han, Z. Zhang, J. Li and C. Wang, Stabilizing high sulfur loading Li-S batteries by chemisorption of polysulfide on three-dimensional current collector, *Nano Energy*, In press
7. X. Wang, **T. Gao**, X. Fan, F. Han, Y. Wu, Z. Zhang, J. Li and C. Wang, Tailoring surface acidity of metal oxide for better polysulfide entrapment in Li-S batteries, *Advanced Functional Materials*, DOI: 10.1002/adfm.201602264
8. F. Han, **T. Gao**, Y. Zhu, K. J. Gaskell, C. Wang, "A Battery Made from a Single Material", *Advanced Materials*, 27(2015)3473
9. L. Suo, O. Borodin, **T. Gao**, M. Olguin, J. Ho, X. Fan, C. Luo, C. Wang, K. Xu, "Water-in-Salt" Electrolyte Enables High Voltage Aqueous Li-ion Chemistries" *Science*, 350(2015)938. Perspective from Prof. Bruce Dunn.
10. F. Han, J. Yue, X. Fan, **T. Gao**, C. Luo, Z.i Ma, L. Suo, C. Wang, Batteries Enabled by Mixed-Conductive Li<sub>2</sub>S Nanocomposites, *Nano Letters*, 16(2016), 4521-4527
11. J. Mao, C. Luo, **T. Gao** and C. Wang, "Scalable synthesis of Na<sub>3</sub>V<sub>2</sub>(PO<sub>4</sub>)<sub>3</sub>/C porous hollow spheres for Na-ion batteries cathode" *Journal of Materials Chemistry A*, 2015, 3, 10378

12. X. Fan, Y. Zhu; C. Luo; **T. Gao**; L. Suo; S.-C. Liou, K. Xu, C. Wang, "In situ Lithiated FeF<sub>3</sub>/C Nanocomposite as High Energy Conversion-Reaction Cathode for Lithium-ion Batteries" **J. Power Sources**, 307 (2016) 435-442
13. X. Fan, Y. Zhu, C. Luo, L. Suo, Y. Lin, **T. Gao**, K. Xu, and C. Wang, "Pomegranate-Structured Conversion-Reaction Cathode with a Built-in Li Source for High-Energy Li-Ion Batteries", *ACS Nano*, 2016, 110, 5567–5577
14. L. Suo, O. Borodin, W. Sun, X. Fan, C. Yang, F. Wang, **T. Gao**, Z. Ma, M. Schroeder, A. v. Cresce, S. M. Russell, M. Armand, A. Angell, K. Xu, and C. Wang, "Advanced High Voltage Aqueous Li-ion Battery Enabled by “Water-in-Bisalt” Electrolyte," *Angew. Chem. Int. Ed.* (VIP). 2016,55,7136–7141
15. C. Luo, Y. Zhu, O. Borodin, **T. Gao**, X. Fan, Y. Xu, K. Xu, C. Wang, "Activation of Oxygen-Stabilized Sulfur for Li and Na Batteries," **Advanced Functional Materials**), DOI: 10.1002/adfm.201503918
16. Y. Zhu, X. Fan; L. Suo, L. Chao, T. Gao, C. Wang, "Electrospun FeS<sub>2</sub>@Carbon Fiber Electrode as a High Energy Density Cathode for Rechargeable Lithium Batteries" **ACS Nano**, 10 (1), pp 1529–1538
17. Y. Zhu, Y. Wen, X. Fan, **T. Gao**, F. Han, C. Luo, S. Liou, C. Wang, "Red Phosphorus-Single-Walled Carbon Nanotube Composite as a Superior Anode for Sodium Ion Batteries." *ACS Nano*, 9(2015)3254.
18. Y. Zhu, L. Suo, **T. Gao**, X. Fan, F. Han, and C. Wang, Ether-based electrolyte enabled Na/FeS<sub>2</sub> rechargeable batteries, *Electrochemistry Communications*, 54 (2015) 18–22
19. J. Wang, C. Luo, **T. Gao**, A. Langrock, A. C. Mignerey, C. Wang, "An Advanced MoS<sub>2</sub>/Carbon Anode for High Performance Sodium-Ion Batteries" *Small*, 11(2015) 472. DOI: 10.1002/sml.201401521. highlighted in cover

20. C. Luo, Y. Zhu, **T. Gao**, Y. Xu, Y. Liu, J. Wang, C. Wang, "Graphene Oxide Wrapped Croconic Acid Disodium Salt for Sodium Ion Battery Electrodes" *Journal of Power Sources*, 250(2014)372.
21. X. Fan, J. Mao, Y. Zhu, C. Luo, L. Suo, **T. Gao**, F. Han, S. C. Liou and C. Wang, "Superior Stable Self-healing SnP3 Anode for Sodium-ion Batteries" *Advanced Energy Materials*, 10.1002/aenm.201500174
22. L. Suo, Y. Zhu, F. Han, **T. Gao**, C. Luo, X. Fan, Y. Hu, and C. Wang, "Carbon Cage Encapsulating Nano-cluster Li2S by Ionic Liquid Polymerization and Pyrolysis for High Performance Li-S Batteries," *Nano Energy*, 13(2015)467
23. J. Wang; C. Luo, J. Mao, Y. Zhu, X. Fan, **T. Gao**, A. Mignerey, C. Wang, "Solid-State Fabrication of SnS2/C Nanospheres for High Performance Na-Ion Battery Anode," *ACS Applied Materials & Interfaces*, 2015, 7 (21), pp 11476–11481

† refers equal contribution

## Conference Presentations

1. Material Research Society Spring Meeting, Phoenix, AZ, 2017
2. 18th IMLB, Rechargeable Al/S Battery with Ionic Liquid Electrolyte, Chicago, IL, USA  
(Jun. 2016)
3. 228th Electrochemical Society Meeting, High Capacity Rechargeable Magnesium Battery  
Enabled By Dual-Ion Chemistry Phoenix, AZ (2015)

